Radiation-induced processes within DNA in the gas phase

Min Liu

Normandie Université

UNIVERSITÉ CAEN NORMANDIE

THÈSE

Pour obtenir le diplôme de doctorat

Spécialité **PHYSIQUE**

Préparée au sein de l'**Université de Caen Normandie**

Radiation-induced processes within DNA in the gas phase

Présentée et soutenue par

MIN LIU

Thèse soutenue le 18/12/2023

devant le jury composé de :

M. SAMUEL EDEN	Maître de conférences HDR - The Open University	Rapporteur du jury
M. LUKE MAC ALEESE	Chercheur HDR - UNIVERSITE LYON 1 CLAUDE BERNARD	Rapporteur du jury
M. AMINE CASSIMI	Directeur de recherche au CEA - Université de Caen Normandie	Membre du jury
M. FRANCOIS CHEVALIER	Directeur de recherche au CEA - Université de Caen Normandie	Membre du jury
MME SANDRINE LACOMBE	Professeur des universités - Université Paris Saclay	Président du jury
M. JEAN-CHRISTOPHE POULLY	Maître de conférences - Université de Caen Normandie	Directeur de thèse Co-encadrant

Thèse dirigée par **JEAN-CHRISTOPHE POULLY** (Centre de recherche sur les ions, les matériaux et la photonique (Caen))

ED 591 PSIME

CIMAP

THÈSE

Pour obtenir le diplôme de doctorat

Spécialité PHYSIQUE

Préparée au sein de l'Université de Caen Normandie

Radiation-induced processes within DNA in the gas phase

Présentée et soutenue par

Min LIU

Directeur de thèse：Jean-Christophe POULLY

Centre de recherche sur les ions, les matériaux et la photonique (Caen)

I want to warn you again.
After wearing the Gold Ring, you'll no longer be a normal human.
You can't touch human desires anymore.
If you do so, the Gold Ring will get smaller and smaller.
It's unbearably painful.

Okay.

A CHINESE ODYSSEY PART TWO: CINDERELLA

Jeffrey Lau

Table of contents

1 Introduction

According to the World Health Organization (WHO), ionizing radiation is a type of energy released by atoms that travels in the form of electromagnetic waves (gamma or X-rays *etc*.) or particles (neutrons, beta or alpha *etc*.).[1] On Earth, people are exposed to ionizing radiation every day, from both natural sources and man-made sources. Natural sources include radiation from space, the earth, building materials and radioactive elements that are naturally in our body. Man-made sources are mainly medical diagnostic exams. Normally the amount of ionizing radiation is small and negligible. However, in certain cases, there is a risk for us to receive excess radiation. For example, if your house locates in a radium-rich region and has a leaky foundation, you may be exposed to excess radiation from radon. Accidents with radioactive materials can also bring surplus radiation to those who are in site. Therefore, radiation research is crucial to evaluate the potential risks and provide scientific advice for radiation related actions. Furthermore, radiation research can contribute to the development of basic biological research, such as DNA damage and repair, and more practical tools, such as radiation therapy.

Of all the living cell lesions caused by ionizing radiation, those affecting DNA are the most common and important.[2] Hence, we will focus on radiation-induced processes within DNA strands in this thesis. We will start by introducing radiotherapy, which is the application of radiation-induced denaturation of DNA strands. Then we will briefly introduce the basic information about DNA, including its definition, history and structure. We will then describe tandem mass spectrometry, a commonly used technique for characterizing DNA in the gas phase. Finally, there will be a presentation of related work that has been reported in this area.

1.1 Radiation therapy

1.1.1 Biological effect of radiation

Radiation was first discovered by Henri Becquerel in 1896 while studying the emissions from uranium.[3] Two years later, Pierre and Marie Curie made a historic announcement of the discovery of two previously unknown elements: polonium and radium.[4,5] These two elements exhibited significantly higher levels of radioactivity compared to uranium. The Curies introduced the term “radioactivity”. In 1903, Becquerel and the Curies shared the Nobel Prize in Physics because of these discoveries.[6,7] Since then, much more work about radiation had been done by many physicists, including Rutherford, Debierne, Elster, etc. An important work

among them was the discovery of artificial radioactivity and the identification of new radioelements produced in the laboratory by Irène and Frédéric Joliot in 1934.[8]

After radiation was first discovered, there was a time when radioactive elements were widely used in everyday life because people thought they were good for health. With a deeper understanding of radiation thanks to research, people have learned that, like most things in the world, radiation has two sides. On the one hand, as Frédéric Joliot successfully predicted in his official Nobel Lecture[9], radiation can be used for cancer treatment and illness diagnosis. On the other hand, radiation can also be harmful to human health.

As far as its human health risks are concerned, we need to specify what kind of radiation we are talking about. Based on the energy level, radiation can be divided into two different terms: ionizing and non-ionizing radiation. Non-ionizing radiation, such as radiowaves, microwaves, ultraviolet (lower energy part), visible, and infrared radiation, is a type of radiation with lower energy compared to ionizing radiation. In contrast to ionizing radiation, non-ionizing radiation does not remove electrons from atoms or molecules in substances such as air, water, and living tissue, and its energy is even not sufficient for excitation of electrons in most cases. Ionizing radiation, as its name suggests, is a type of energy that extracts electrons from atoms and molecules found in materials like air, water, and living tissue. Typical ionizing radiation consists of atomic or subatomic particles (*e.g.* alpha particles, beta particles, and neutrons) and electromagnetic waves (*e.g.* gamma rays, X-rays, and the higher energy ultraviolet part of the electromagnetic spectrum).

For non-ionizing radiation, there is evidence that it can cause free-radical damage to humans, animals, plants and microorganisms, because it can disrupt oxidative repair mechanisms, leading to oxidative stress, harm to cellular components, including DNA, and disruptions to cellular processes that contribute to the development of cancer.[10] However, since non-ionizing radiation lacks the requisite energy to detach electrons to ionize atoms or molecules, it is generally accepted that it cannot cause cancer. Most of the literature refers to ionizing radiation as the radiation that causes health hazards.[11–15] In this thesis, we focus on the physical and chemical molecular processes induced by ionizing radiation.

For ionizing radiation, it possesses sufficient energy to generate highly reactive and short-lived molecules known as free radicals by ejecting an electron from the molecules in the biological tissues. Since water is the most abundant molecule within cells, the majority of free radicals originate from the radiolysis of water. Moreover, because of their unstable property,

free radicals can easily react with nearby molecules, resulting in the transfer of chemical damage. Under physiological conditions, these free-radical reactions typically take place within a millisecond. These reactions cause chemical damage to the components of the cell, including proteins, enzymes, membrane components, and more. While these molecules are present in large quantities within each cell, harm to a few of them likely has minimal impact on the cell's overall viability since they can be rapidly regenerated. However, there is one cellular component, found within the cell nucleus, which stands out as nearly unique in its vulnerability: DNA.

DNA is usually a double-helix molecule composed of a repeating sequence of bases in the biological environment, which is explained in detail in the next section. The repeating sequence of bases contains the genetic information needed to encode proteins related to the functions of cells. Therefore, specific functions of the cells may be lost if radiation-induced damage causes the loss or modification of the DNA bases, which contains genetic information. Some of these functions may be essential for cell survival, and their loss could lead to cell death. It makes DNA the most vulnerable component of a cell when it is irradiated. Fortunately, over the course of evolution, life on Earth has developed a sophisticated repair system. This repair system can monitor DNA integrity, recognize and repair DNA damage induced by many processes, including radiation. However, this repair system can only deal with low-dose radiation, because high-dose radiation caused DNA damage is beyond the capability of the repair system. Even at low doses, it can increase the unsuccessful repair of radiation-induced damage and thus increase the risk of subsequent radiation-induced carcinogenesis.[16,17]

In fact, biological damage to living tissue cannot be assessed simply by the absorbed dose, as it is influenced by many factors. Different types of ionizing radiation have different biological effectiveness in causing damage to living tissue and different tissues and organisms in the human body have varying sensitivities to radiation. Thus, the dose equivalent H (unit: Sv, short for Sievert) is used to predict the biological damage to living tissue as a result of radiation exposure.

In addition, because it takes time to repair DNA damage, the health risk is lower when the radiation dose is delivered over a long period of time (instead of being delivered all at once). For example, a single dose of 1 Sv can cause symptoms of acute radiation sickness (ARS), which is a sickness that occurs when someone is exposed to high levels of radiation, enough to harm their blood, digestive system, heart, blood vessels, or central nervous system.[18] Meanwhile, if the same dose is given to the whole population in one year, 5.5% of them will

either pass away due to cancer or, if they survive, experience a reduced quality of life.[19] Therefore, the dose rate, measured in microsieverts per hour (μSv/hour) or millisieverts per year (mSv/year), is a crucial parameter to consider in terms of biological damage.

Normally, the annual equivalent dose received by the average population is significantly lower and comes mainly from natural sources. For example, the average dose to U.S. population from all sources is 6.2 mSv/year while the natural contribution (including radon & thoron, cosmic radiation and terrestrial radiation) is 2.82 mSv/year.[20] For comparison, the dose for a significant increase in cancer risk is above 100 mSv.[21] The dose limit recommended by the International Commission on Radiological Protection (ICRP) is 20 mSv/year for exposed workers performing occupational activities and 1 mSv/year for the general public.[19]

1.1.2 Application of radiation

On the other hand, the biological damage to normal living tissue also applies to the cancer cells. This has led to the development of radiation therapy (also called radiotherapy) since the discovery of X-rays by Röntgen in 1895 and the following discoveries related to radioactivity. As we know, cancer is a major worldwide health issue. It causes around 7.6 million deaths every year[22] and the estimated cancer mortality rate for every country across the globe in every year over the next century is approximately 0.24%.[23] Radiation therapy (X-rays, to be more precise) was first used to treat an advanced ulcerated breast cancer in 1896, less than 60 days after the discovery of X-rays.[24,25] The side-effects of radiation were also soon recognized by people,[26] which encouraged the optimization of radiation therapy and promoted the radiation protection. Nowadays, radiation therapy has become a more accurate, more efficient and less harmful anticancer therapy, thanks to the discoveries in radiation physics, chemistry and biology over the last century.[25]

As summarized by Thariat *et al.*,[27] there are three advantages of radiation therapy to treat cancer:

1) Clinical effective: radiation therapy has been shown to be effective in curing most of cancers, when combined with surgery and medical treatments. Around half of the cancer patients are treated with radiotherapy.

2) Treatment conservative: radiation therapy aims to sculpt the optimal dose of radiation on the tumor volume while sparing normal tissues. This approach helps in preserving the function and integrity of organs affected by cancer, which greatly improve the life quality of the cancer patients.

3) Cost-efficient: radiation therapy, when compared to other treatment options, can be a cost-effective approach in the management of cancer. It offers a balance between effectiveness and cost, making it a valuable option for patients.

In the clinical application of radiation therapy, there are several beams used: kilovoltage X-ray beams, high-energy photon beams (megavoltage beams), electron beams and hadron beams (including proton and other heavy charged-particle beams).[11] Figure 1.1 shows the dose profile of some representative beams in water. The 2.5 MeV photon beam exhibits a sharp dose increase upon entry, followed by a consistent decrease. The hadron beams (150 MeV protons and 250 MeV C-12) both show a relatively constant dose deposition along the track and end with a sharp dose peak. This peak is known as the Bragg peak.[28] After the Bragg peak, the dose rapidly diminishes to nearly zero. The low energy electron beams (5 MeV and 15 MeV) display a relatively flat dose distribution until reaching the maximum dose, after which there is a sharp decline in dose. The high energy electron beam (150 MeV) has a similar flat dose deposition before reaching the maximum dose but has a slow decline in dose thereafter.

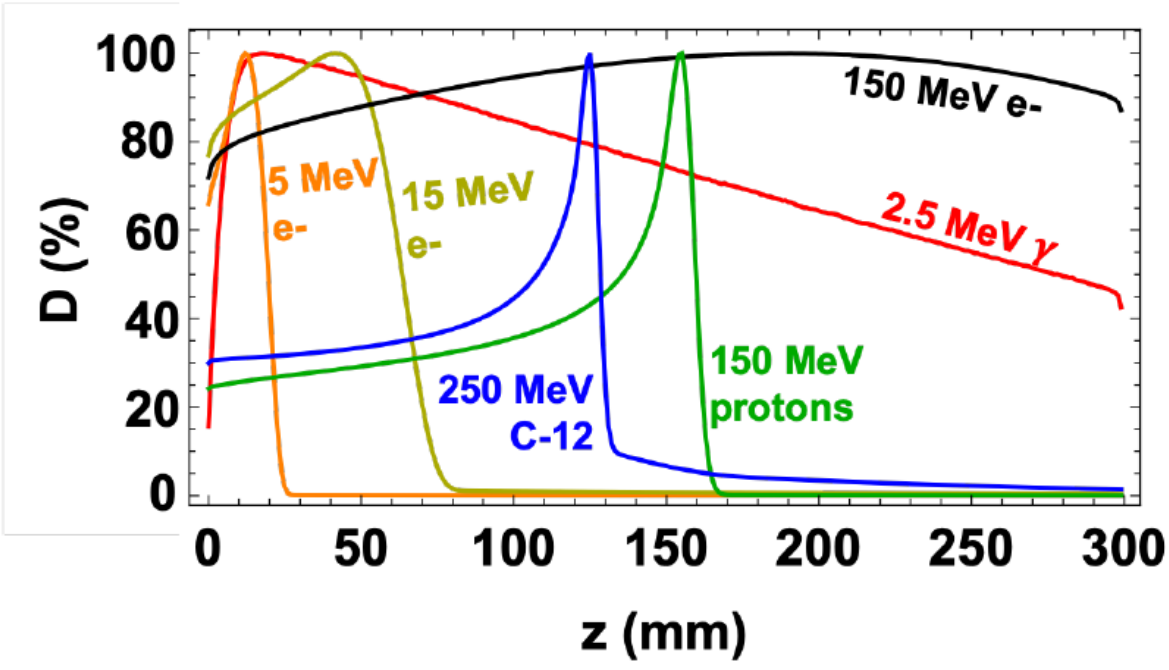

Figure 1.1: Integrated percentage depth-dose profiles of σ = 5 mm wide pencil beams of 2.5 MeV photons, 5, 15 and 150 MeV electrons, 150 MeV protons and 250 MeV/u Carbon-12 ions in water normalized to dose maximum simulated using the TOPAS MC code. Reprinted from Agnese Lagzda, VHEE Radiotherapy Studies at CLARA and CLEAR facilities, doctoral thesis, The University of Manchester, 2019.[29]

In this thesis, we mainly focus on two types of ionizing particles, photon and ion beams, which correspond to the two types of radiation therapy. In the following, a more detailed overview of these two types of radiation therapy will be given.

The photon radiation therapy uses kilovoltage X-ray beams or megavoltage beams (high-energy photon beams). Kilovoltage x-rays were the earliest form of external beam therapy to be employed in medical treatment.[11] Their disadvantage are that they do not have enough penetrative qualities. Therefore, multiple overlapping beams are often used to reach a high dose. They can be further divided into two types, superficial X-rays (10-150 kV) and deep X-rays (150-400 kV). The former is used for very thin skin lesions and the latter is used for thicker lesions. On the other hand, high-energy photon beams are the most commonly employed beams in radiation therapy due to their superior penetration capabilities in comparison to kilovoltage beams.[11] At the early stage of photon radiation therapy, high-energy photons are produced by cobalt-60 radioactive sources. Linear electron accelerators are now the most widely used radioactive sources for photon radiation therapy because they can produce beams with enhanced penetration, provide flexibility in selecting beam energy, generate a narrower penumbra at the edge of the beam, and deliver an increased dose rate. One significant benefit of high-energy photon beams is the skin-sparing effect thanks to their very low entrance dose (shown in Figure 1.1). This effect becomes more pronounced with increasing energy levels, when the field size is small (less than 10 cm^2).[11]

The hadron radiation therapy, as shown in Figure 1.1, is able to release most of its energy at the end of the ion range and show great biological effects there, due to the sharp high-dose Bragg peak. This is because when the ions are slowed down to velocities similar to those of valence electrons within the molecules in the medium, the interaction between the ions and the medium becomes stronger and then the energy transfer increases, causing the ions to stop very quickly. Thus, it makes the dose-localization possible in clinical application. However, this Bragg peak is so sharp (usually several millimetres wide) that it cannot cover most deep-seated tumors, which are about several centimetres wide. To solve this problem, a uniform dose field created by Spread Out Bragg Peak (SOBP) is used for clinical applications. Figure 1.2 shows the formation of SOBP by superposing beams of various energies.

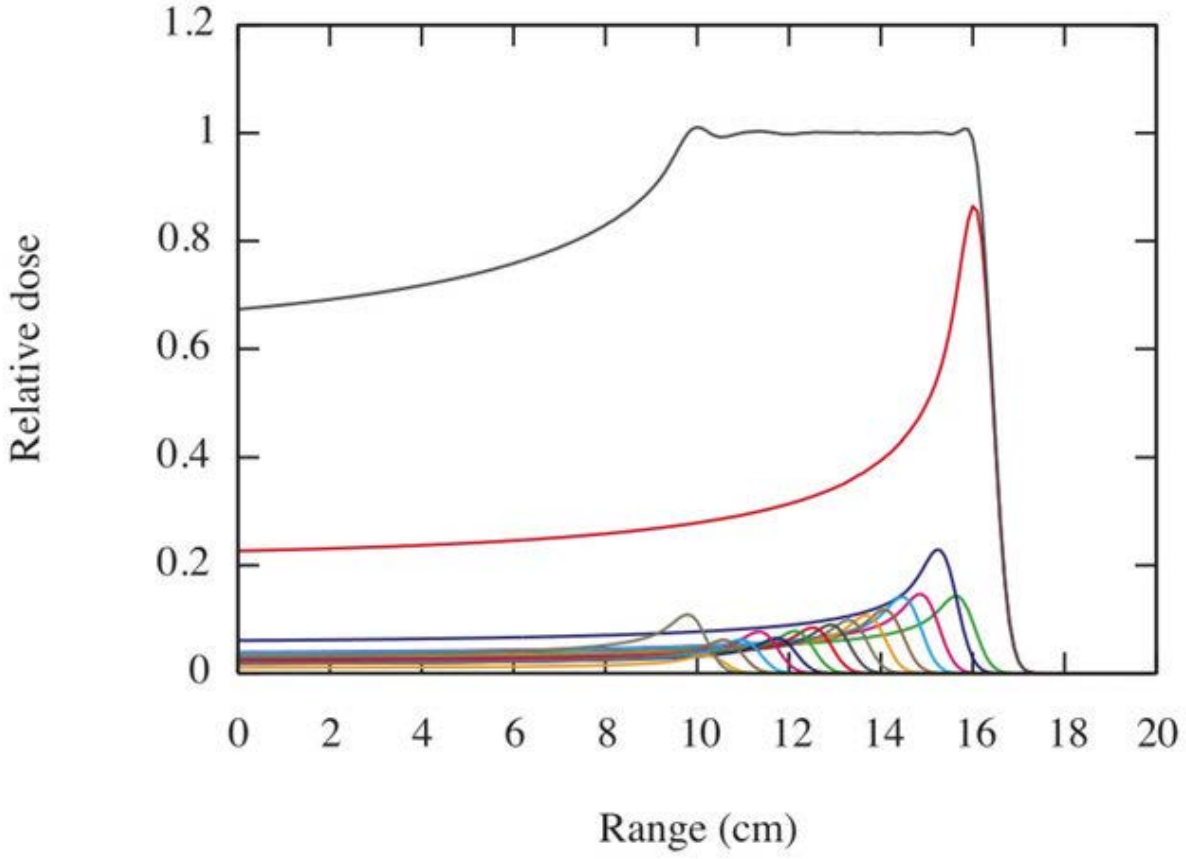

Figure 1.2: The formation of SOBP by superposing beams of various energies. Reprinted from T. Yokoi et al., Beam injection issues of FFAG for particle therapy, in Proceedings of EPAC, 2008, p. 3401 .[30]

1.2 DNA

DNA was first observed in the late 1800s by the Swiss biochemist Frederich Miescher, who call it "nuclein".[31] In modern biology, DNA stands for deoxyribonucleic acid, which is now widely known as the genetic material of all known living organisms and many viruses on earth. However, since Mendel's discovery of the fundamental laws of heredity in 1865,[32] there has been a longstanding belief that protein, rather than DNA, is the genetic material. Until 1944, Avery, McCarty and Macleod had found that DNA is the "transforming factor" in bacteria.[33] Although their work was initially not widely accepted by the mainstream scientific community, it stimulated further research into DNA. Later, in 1951, Chargaff *et al.* proved that the ratio of adenine (A) to thymine (T) and of guanine (G) to cytosine (C) is 1 in the DNA of salmon sperm.[34] This finding implied that certain structural principles might apply to DNA. This finding, together with the X-ray diffraction data from Wilkins and Franklin, helped Watson and Crick to reveal the famous double helix structure of DNA in 1953.[35–37]

In the double helix structure of DNA, as shown in Figure 1.3, there are two strands joined together, wrapped around the same axis in an antiparallel helical structure to form a twisted ladder. Each strand is a chain of nucleotides, which are the building blocks of DNA. These building blocks are made up of a phosphate group, a sugar molecule (deoxyribose) and a nucleobase. There are four nitrogenous bases in DNA, two purines (adenine and guanine) and two pyrimidines (cytosine and thymine). The bases are located on the inside of the helix, while the phosphate groups are located on the outside. Two nucleobases are paired by hydrogen bonds to form a base plane, one nucleobase from one strand and another nucleobase from the other strand. The base plane is perpendicular to the central axis.[36] The base pairing rules are: firstly, the purine adenine (A) always forms a hydrogen bond with the pyrimidine thymine (T) on the other strand; secondly, the pyrimidine cytosine (C) always forms a hydrogen bond with the purine guanine (G) on the other strand. Because of these rules, the two strands are complementary to each other. This complementary pattern facilitates the process of DNA duplication. During duplication, the two DNA strands unwind first by breaking the hydrogen bonds. A new complementary strand is then synthesized according to the sequence of an old strand. The synthesis works for both old strands, resulting in two identical new double-stranded DNA molecules.

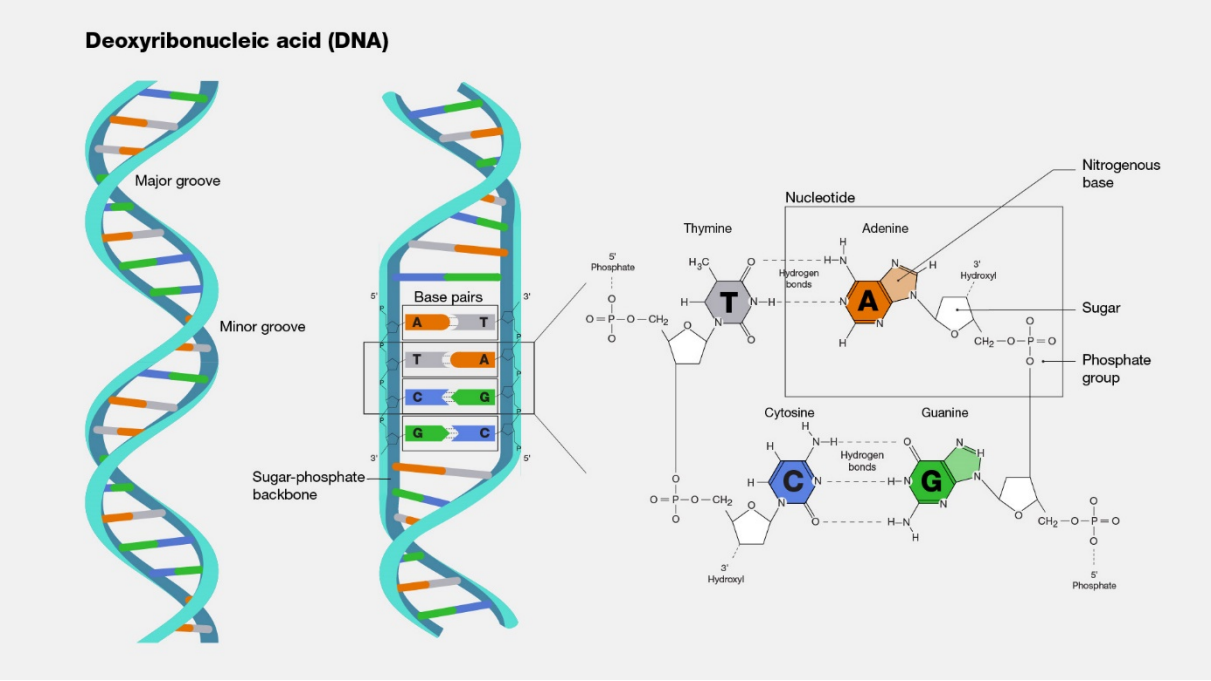

Figure 1.3: The double helix structure of DNA (left) and base pairing rules (right). Courtesy: National Human Genome Research Institute[38]

1.3 Tandem mass spectrometry for characterization of DNA

Mass spectrometry (MS) is an analytical technique that allows measuring the mass-to-charge (*m/z*) ratio of atomic or molecular ions in a vacuum chamber, thanks to DC or AC electric fields. In this section, we will show how mass spectrometry can give valuable information on some properties of biomolecules such as DNA. To be studied in a mass spectrometer, biomolecules have to be brought in the gas phase by a source: in early investigations, mostly ovens were used to heat a powder or liquid of the molecule of interest. However, biologically-relevant molecules such as DNA chemically react and decompose upon heating before being vaporized. With the development of soft ionization sources like electrospray ionization (ESI) or matrix-assisted laser desorption/ionization (MALDI), it became possible to bring polar, thermally fragile compounds into the gas phase. These sources create molecular ions that can be manipulated by electric or magnetic fields, notably to be guided, but also selected or accumulated (see Chapter 2 for examples). Selecting the molecular ion of interest (precursor) vs. *m/z* is useful when the source creates several charge states of the same molecular ion and/or different molecular ions, which is very often the case of ESI. This selection is performed by a first step of mass spectrometry. If further mass spectrometry steps are applied, the apparatus is called a tandem mass spectrometer, or MS/MS (two examples of tandem mass spectrometers are shown in the setup section). Tandem mass spectrometry is based on activating the precursor ion and analyzing the *m/z* ratio of its product ions, mostly formed by fragmentation by cleavage of noncovalent and/or covalent bonds. As a result, the ion activation method is very important in the analysis because it directly decides what products we can get.

The most common ion activation techniques used in tandem mass spectrometry are collision-induced dissociation (CID), Surface-induced dissociation (SID), Electron-capture dissociation (ECD), Infrared multiphoton dissociation (IRMPD) and Blackbody infrared radiative dissociation (BIRD).[39] Specifically, in CID, a selected ion is activated by collisions with a neutral gas in the collision cell, which increases the internal energy of the selected ion. CID can be performed at high (100–1000 eV) or low (1-100 eV) collision energies using different types of instruments. SID involves the collisional activation of precursor ions upon impact with a solid surface. ECD involves the capture of low-energy electrons by cations carrying multiple charges, leading to a reduction in the charge state of the ions followed by subsequent fragmentation. IRMPD is a photodissociation activation method that vibrationally excites the ions by the successive absorption of multiple photons from an infrared laser. BIRD involves the dissociation of ions by the absorption of blackbody photons emitted from the walls of a

heated ion cyclotron resonance (ICR) cell. In this thesis, we have used CID activation in Chapter 3.

Thanks to the improvement of related techniques in the past years, tandem mass spectrometry is considered a powerful tool for DNA studies due to its advantages of sensitivity, accuracy and versatility when applied to oligonucleotide characterization.[40] It can provide detailed information about the nucleotide sequences, the identification of structural modifications, the development of higher-order structures, and the interactions between nucleic acids and other cellular components or chemotherapeutic agents.[40] Moreover, if combined with ion mobility spectrometry (IMS), it can also provide an extra information about the collisional cross section (CCS) of the ions, which relates to their shape and size. It is also the main tool in the investigations of this thesis, in order to identify the ionic products of DNA after irradiation by X-ray photons (*cf.* Chapter 4) or carbon ion beams (see Chapter 5).

In order to name the fragments created after irradiation of DNA in the tandem mass spectrometer, we use the commonly applied nomenclature for the oligonucleotide fragments proposed by McLuckey, Van Berkel, and Glish,[41] which is shown in Figure 1.4. This nomenclature is based on the cleavage of the phosphodiester bonds. The four possible fragments which contain the 5'-OH group are named by the letters a, b, c, and d while the four possible fragments which contain the 3'-OH group are named by the letters w, x, y, and z. The numerical subscripts represent the number of the building blocks from the corresponding terminal group in the fragment ions. The bases (B_n) are also numbered according to their positions with respect to the 5'-OH group of the DNA chain. The numerical subscript of bases stands for the number of the bases from the 5' terminal group in the fragment ions. If two or more bonds break, the corresponding fragment ions are called internal fragments. Specifically, we use "i" (short for internal) plus the abbreviation of the base (A, T, C, G) to refer to the internal fragments in this thesis.

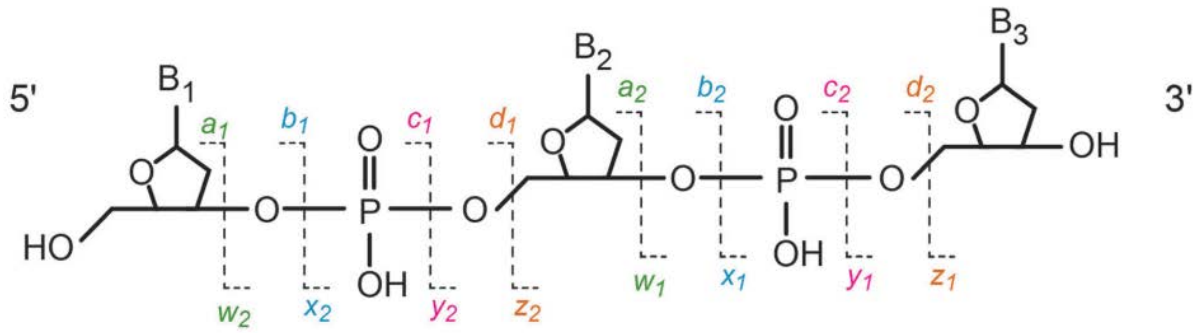

Figure 1.4: Nomenclature for oligonucleotide fragments. Reprinted from Stefan Schürch, Mass Spectrometry Reviews 35, 483–523 (2016), with the permission of John Wiley and Sons.

1.4 Previous studies of DNA in the gas phase

According to the interaction mechanism, the interaction between DNA and radiation can be divided into two types: direct interaction and indirect interaction. The direct interaction happens when the DNA in the cells is directly hit by the ionizing radiation. The indirect interaction is mentioned in Section 1.1.1, it occurs when the DNA in the cells reacts with the reactive species (*e.g.* hydroxyl radicals, solvated electrons, and hydrogen atoms) caused by the interaction between ionizing radiation and other species, mainly cellular water. It has been believed that radiation-induced damage of DNA comprises approximately one-third "direct" damage and two-thirds "indirect" damage.[42] However, this assumption has been doubted by the ultrafast electron transfer experiments on DNA, which suggest that about two-thirds of the DNA damage after irradiation is induced by direct interaction and one-third is induced by indirect interaction.[43,44]

In any case, since the direct interaction is an important part of the interaction between the DNA and the radiation, it is of great importance to study the processes happening after direct interaction, such as the transfer of charge, atoms and energy within the DNA molecules. Nevertheless, this is not easy to achieve in condensed phase experiments. On the other hand, gas phase experiments have several advantages for studying the direct interaction, as summarized by Chevalier *et al.*:[45]

- Due the removal of solvent, the gas phase investigations can bring the information about the intrinsically properties of DNA.
- Thanks to quantum chemical methods, the experimental data in the gas phase can be compared with the results of theoretical calculations.
- Gas-phase analytical methods such as mass spectrometric tools make it possible to define the initial state of DNA such as size, stoichiometry, temperature, charge, and tautomeric states. In addition, we can determine the final state of DNA by detecting the mass-to-charge (*m/z*) ratio of ionic products generated following the interaction between DNA and ionizing radiation.
- Gas-phase techniques such as ion mobility spectrometry can provide information about the geometric structure of DNA, allowing a particular conformer to be selected or a specific ion product with a particular conformer to be traced.

- Owing to the techniques such as electrospray (or nanospray) ionization or matrix-assisted laser desorption ionization, a large molecule like DNA can be transferred intact to the gas phase.

Except for the summary of advantages for studying the direct interaction, the authors of the same review also wrote a summary of the previous work about the direct interaction between DNA building blocks and radiation in the gas phase.[45] In the following, I will adapt this summary.

Since the gas-phase techniques such as mass spectrometry often involve ionization of the target molecules, the study of DNA began with one of its building blocks, nucleobases. This is because they are more stable (compared to oligonucleotides or longer DNA sequences) when thermally heated. In fact, before the invention of electrospray ionization and matrix-assisted laser desorption ionization, it was very hard to bring the large DNA molecules into the gas phase without damaging them. In 1975, Hush *et al.* did a pioneering work to measure the ionization energy of several nucleobases by means of photoelectron spectroscopy.[46] One year later, Sukhodub and his colleague studied the thermodynamics of binding of methylated nucleobase pairs in the gas phase using mass spectrometry.[47] In addition to single nucleobases, some work has been devoted to the study of non-covalent clusters of nucleobases, such as their dimers. For example, Nir *et al.* generated isolated guanine-cytosine (G-C) and guanine- guanine (G-G) base pairs through hydrogen bonding.[48] Moreover, they identified the proton transfer in the G-C pair, which is a crucial step in the pathways leading to radiation-induced DNA damage. Similar proton transfer was also found in the cytosine-cytosine (C-C) dimers and uracil-uracil (U-U) dimers, after ionization by VUV single photon absorption.[49,50] More recently, Hartweg *et al.* observed proton transfer in the adenine-thymine (A-T) noncovalent complex.[51] They measured a very low upper limit (317 meV) of the barrier of the proton transfer in the ionized A-T pair. Zappa *et al.* created larger nucleobase clusters by embedding thymine and 1-methylthymine in helium clusters and ionized them by electron impact.[52] They found that protonation was the predominant process after electron impact ionization.

With so many studies on DNA nucleobases, researchers want to know how the sugar moiety affects the radiation-induced damage on DNA. Since the 1960s, extensive research has been dedicated to neutral nucleosides in the gas phase. In 1962, Biemann and McCloskey reported that nucleobase radical cations and protonated nucleobases were produced in the electron ionization source of a time-of-flight mass spectrometer, and that hydrogen was rearranged from

the sugar group to the nucleobase.[53] After that, identical nucleobase cations have been detected with different ionization methods, such as proton impact,[54] oxygen ion collision,[55] and VUV photoabsorption[55–57]. This indicates that the formation of the nucleobase cations does not need special ionizing particles. For example, after VUV photoabsorption, the thymine radical cation generated from the ionized thymidine was observed.[55] However, only much smaller singly-charged fragment ions (with *m/z* no more than 55) are detected after X-ray (330 eV) photoionization, when the carbon 1s electrons are ionized.[58] In these studies involving the formation of the nucleobase radical cations, thermal reactivity effects should also be taken into account, because the nucleosides were heated by the oven. Even with the application of the gentler laser thermal desorption technique, it is noteworthy that nucleoside decomposition can still be observed.[59]

As the monomeric units of DNA, nucleotides have also been studied after exposure to ionizing radiation, although less is known. Shin and Bernstein have generated four different neutral nucleotides (adenosine-, cytidine-, guanosine-, and uridine-5'-monophosphate) in the gas phase, and ionized them with a VUV (10.49 eV) laser.[60] They have demonstrated that the primary site of fragmentation for these species is the bond between the carbohydrate and nucleobase moieties. In addition, they have used density functional theory (DFT) calculations to explain the experimental results. Ball *et al.* have ionized adenosine monophosphate, diphosphate and triphosphate (AMP, ADP and ATP) by electron impact at 26.5 eV.[61] They showed that the ionic products differed when the nucleotide cation contained different numbers of sodium. Among the ionic products, they observed the protonated nucleobase as a major product, which is also detected from protonated AMP after absorption of a single ultraviolet (UV) photon (4-12.5 eV).[62] Notably, in the latter work, they also investigated the influence of a single water molecule, and demonstrated that it has the ability to exert an influence on the structure and physicochemical attributes of the AMP cation.

Compared to the building blocks and units of DNA, less work has also been done on the oligonucleotides, which are short DNA or RNA molecules. In 1991, the Grotemeyer group did a pioneering work on the ionization of oligonucleotides.[63] In this work, they desorbed neutral protected dinucleotides with an IR laser and then ionized them by resonantly enhanced multiphoton ionization. Because the protective group against thermal decomposition is aromatic, it also has UV absorption, just like nucleobases in the oligonucleotides, making it impossible to determine the initial position of the positive charge (either in the protective group or in the nucleobases). Even so, their findings indicated that preceding the fragmentation of the

backbone and/or cleavage of the glycosidic bond, all product cations undergo hydrogen transfer. However, the influence of the protective group in the process was not clear. In 2013, the electrospray ionization source was used to bring the oligonucleotide into the gas phase, where the protective group is no longer needed. They irradiated protonated dGCAT oligonucleotides by VUV, X-ray photons as well as carbon ions.[64] Upon all these ionizations, the dominant products are always nucleobase cations, including protonated and non-protonated nucleobase ions for guanine, adenine, and thymine. However, cytosine has only protonated, not non-protonated, nucleobase ions. These results all include the hydrogen transfer within the oligonucleotides after ionization. More recently, Schlathölte's group observed intramolecular hydrogen transfer after site-selective ionization by soft X-ray photoabsorption in the isolated tri-oligonucleotide d(^{F}UAG), where ^{F}U stands for fluorouracil.[65] They summarized that hydrogen transfer can occur regardless of where the initial ionization site locates. The same group also studied the influence of size on the VUV photoabsorption of deprotonated oligonucleotides and proved that the valence hole favors migration towards guanine-rich regions.[66] In addition, they identified at least three electrons were detached from a doubly deprotonated gas-phase oligonucleotide following the Auger decay after X-ray photoabsorption.[67]

Despite all the research that has been done on gas-phase irradiation of DNA, there are still many questions that we would like to ask in this area. For example, what are the differences and similarities between ion- and photon-induced ionization of DNA? What is the relationship between the fragmentation pattern and the initial photoabsorption site on DNA? How do the hydrogen bonds between the two strands of the double helix DNA affect the fragmentation after irradiation?

In this thesis, the experimental results related to these questions will be shown in the following chapters. In particular, we will investigate the different fragmentation patterns of the same oligonucleotide upon photoabsorption and ion collision.

1.5 Thesis outline

The structure of this thesis is delineated as follows:

- Chapter 2 describes the experimental setups used in our experiments. A home-built tandem mass spectrometer named Paultje and a commercial mass spectrometer equipped with an ion mobility module will be introduced. In addition, synchrotron user facilities and heavy ion accelerators will be described.

- Chapter 3 identifies the presence of the dimer of the oligonucleotide in the gas phase under our experimental environment. In addition, other information such as the charge state, the conformation of the dimer will be acquired.

- Chapter 4 focuses on the photon-induced fragmentation of the oligonucleotide dCGCGGGCCCGCG. The initial photoabsorption site will be fixed at the backbone of the oligonucleotide, and the fragmentation pattern will be investigated. The charge, energy and hydrogen transfer after photoabsorption will be discussed.

- Chapter 5 studies the carbon ion-induced fragmentation of the oligonucleotide dCGCGGGCCCGCG. Both its monomer and dimer will be studied. Some of the results in this chapter will be compared with the ones in Chapter 4.

- The appendix presents the UV-VUV photofragmentation spectrum of the complex between neutral vancomycin and the singly deprotonated $Ac_2{}^{L}K^{D}A^{D}A$ peptide. We will show that the photofragmentation of the peptide is can be ignored, so that the recorded spectrum can be considered as the UV-VUV photofragmentation spectrum of isolated neutral vancomycin.

Chapter 4 is adapted from the corresponding publication in Chemistry - A European Journal. The appendix is a copy of the corresponding paper in The Journal of Physical Chemistry A. The latter is here reprinted with permission from *J. Phys. Chem. A* 2022, 126, 48, 9042–9050, Copyright 2022 American Chemical Society.

2 Experimental section

2.1 Paultje setup

The mass spectra in Chapters 4 and 5 were obtained using a home-made tandem mass spectrometer called Paultje. Its name comes from the Nobel Prize winner Wolfgang Paul, who invented the radiofrequency (RF) ion trap (Paul-trap)[68]. Paultje means "little Paul" in Dutch. The setup can be used to investigate the irradiation of gas-phase biomolecules by interfacing itself with external ionizing radiation sources, such as synchrotron or ion beamlines. In this thesis, the setup has been interfaced with an X-ray photon beamline located at the 3rd generation synchrotron facility PETRA III (DESY, Hamburg, Germany) and a beamline of MeV highly charged ions located at the GANIL facility (Caen, France).

In this chapter, all different parts of Paultje are described in detail. The main structure of the setup is shown in Figure 2.1.

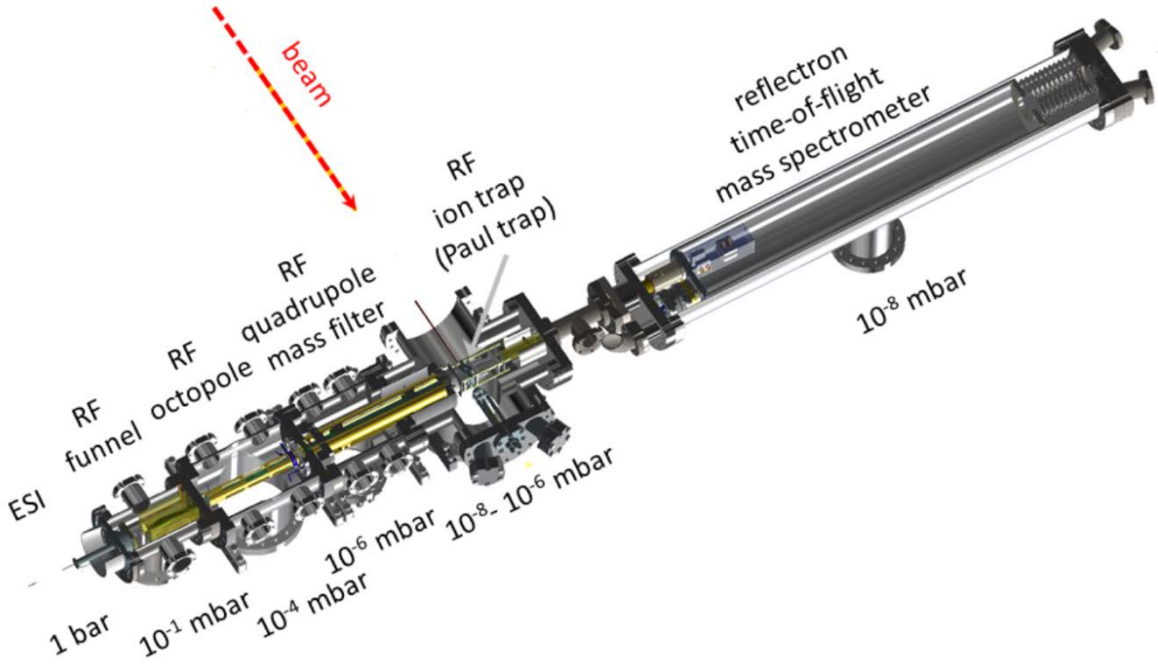

Figure 2.1: Scheme of the home-built tandem mass spectrometer (top view). The beam (photon or ion) enters from the side of the Paul trap. The working pressures of each part are shown. Reprinted from Xin Wang, Photon induced charge and structural dynamics in gas-phase DNA, doctoral thesis, University of Groningen, 2022.[69]

First of all, the molecular ions of interest are produced by an electrospray ionization (ESI) source that works at atmospheric pressure. The ions in the gas phase then go through a metal capillary and are focused into an RF ion funnel. Afterward, they are guided by an RF octopole before reaching a quadrupole RF mass filter, which can select the ions according to their mass-to-charge ratio (*m/z*). Then, the selected ions enter into a Paul trap and are accumulated there

for a controlled time. To achieve better trapping efficiency of the ions, a helium buffer gas at room temperature is used to "cool down" the ions by reducing their kinetic and internal energies. Once enough ions have been trapped, external beams, such as MeV ions or energetic photons, pass through the Paul trap and irradiate the trapped ions for a controlled time. It is important to note that in a Paul trap, cations and anions can be trapped simultaneously. After irradiation, all cations or all anions in the trap are extracted at time zero into a reflectron time-of-flight (Re-TOF) mass spectrometer and are detected by a microchannel plate (MCP) detector. The signal (voltage) from the MCP is sent to a digitizer to record the intensity of the signal as a function of detection time. Since the detection time of a given ion depends on its *m/z* ratio, mass spectra can be extracted from these data.

The functions of each component of the setup shown in Figure 2.1 are described in detail in the following.

2.1.1 Electrospray ionization

Electrospray ionization is a soft ionization method developed by J. B. Fenn, who shared a Nobel Prize in chemistry with Koichi Tanaka and Kurt Wuthrich by the contribution of this invention.[70] This method allows ions in solution to be gently transferred to the gas phase, making it a powerful tool for generating intact biomolecular ions without destroying them. For these biomolecules, the corresponding ions produced by the electrospray ionization often have multiple charge states, and are most of the time either deprotonated, or protonated.

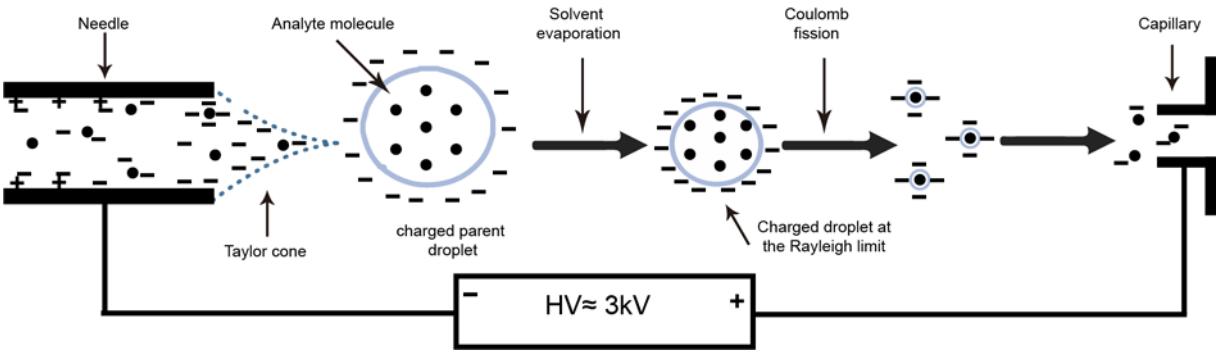

Figure 2.2: Scheme of the electrospray ionization method in negative mode to produce deprotonated molecules. Adapted from S. Banerjee et al., International Journal of Analytical Chemistry, 282574, (2012).

As shown in Figure 2.2, in the negative ion mode, a biomolecule sample solution (about 50 µM) with ammonium hydroxide (to deprotonate the biomolecule) is injected into a metal needle using a syringe pump. In front of the needle tip, there is a metal capillary which is the entrance to the vacuum chambers. The distance between the needle and the capillary is a few millimeters. Between the needle and the capillary, a strong voltage (usually 3 kV) is applied. Because of the

electrical field, charges accumulate at the tip, and a negatively charged drop forms at the end of the needle. The drop turns into a Taylor cone in the electrical field. When the voltage reaches a threshold, the charged parent droplets are ejected from the Taylor cone. The solvent evaporates from the droplet, increasing the Coulomb repulsion. When the surface tension of the droplet cannot compensate for the Coulomb repulsion and the Rayleigh limit is reached, Coulomb fission occurs and many smaller droplets are formed from the parent droplet. Solvent evaporation and Coulomb fission can be repeated until the analyte molecules lose all the solvent and enter the gas phase before entering the capillary. However, the ion signal is usually enhanced by heating the capillary to *e.g.* 100°C to help desolvation.

2.1.2 RF Ion funnel

The RF ion funnel helps to guide and focus the molecular ion beam. It is worth mentioning that this ion beam can contain many different molecular species: several charge states of the molecule of interest, but also fragments or/and ions from the solvent.

When the ions are going out of the heated capillary that transfers them from the atmospheric environment to the first vacuum chamber (where the pressure is around 0.1 mbar), they undergo Coulombic repulsion, together with collisions with gas molecules, which hinders ion transport here. Therefore, an ion funnel is installed after the capillary to compress the phase space of the ions and improve ion transfer to the next vacuum chamber. The funnel electrodes create a RF pseudo-potential that confines the ions radially inside the ion funnel and an axial DC electric field that guides the ions towards the exit of the funnel.

The ion funnel here was purchased from GAA Custom Engineering, LLC (Benton City, Washington, United States) and its design follows the one of Gordon Anderson's group.[71–73] As shown in Figure 2.3, it has two opposite printed circuit board (PCB) plates, which are the electric DC and RF coupling boards, respectively. It consists of 100 stacked square funnel plates with metal ring electrodes of progressively smaller inner diameter, which are soldered to the two PCB plates. The first 99 electrodes are connected together by resistors soldered between each adjacent electrode to create a DC voltage gradient between the first and 99th electrode. The "funnel in" voltage is applied to the first electrode and the "funnel out" voltage is applied to the 99th electrode. The last one is independently connected without a resistive load to apply a different voltage ("funnel exit" voltage) and to push the ions out. The RF voltages with equal amplitude but with 180° phase difference are applied between adjacent electrodes. A modular

RF/DC power system called Modular Intelligent Power Supply (MIPS, from GAA Custom Engineering) is used to drive the funnel. The RF field is generated by a high-Q-head.

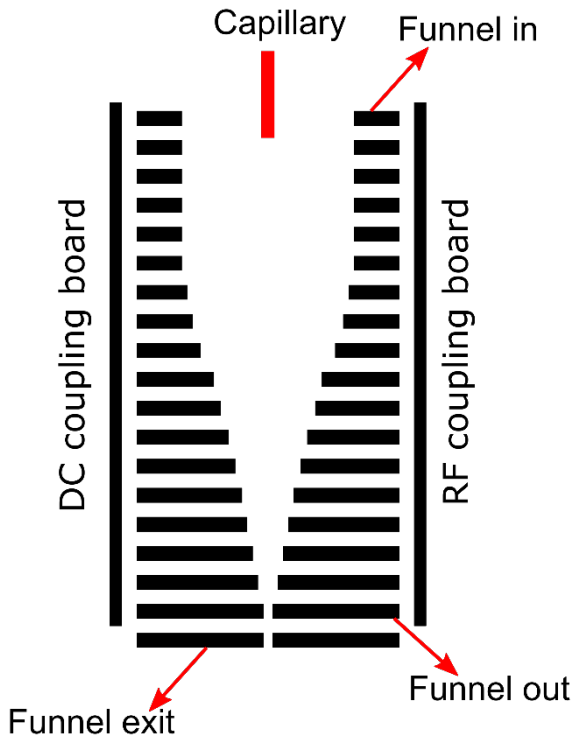

Figure 2.3: Sketch of the ion funnel with capillary. Adapted from Wen Li, Ionization-induced fragmentation dynamics of Guanine-rich oligonucleotides and G-quadruplexes, doctoral thesis, University of Groningen, 2022.

2.1.3 RF octopole

After passing through the exit of the funnel, the ions are transferred to the RF octopole chamber. The RF octopole consists of 8 electrodes, which are stainless steel rods, as shown in Figure 2.4. Two electrically insulated support rings hold the rods in place. The rings are covered by stainless steel diaphragms with one axial opening and 8 openings for the 8 electrodes. Normally, the octopole is used as an RF ion guide with neighboring electrodes with 180° phase difference and biased at a controlled voltage. In this setup, the octopole is also used as a trap for the ions. The bias voltages of the octopole diaphragms can be controlled to accumulate the ions between the two support rings from hundreds of milliseconds to several seconds. By pre-trapping the ions in the octopole, ion bunches can be created for subsequent better trapping in the Paul trap.

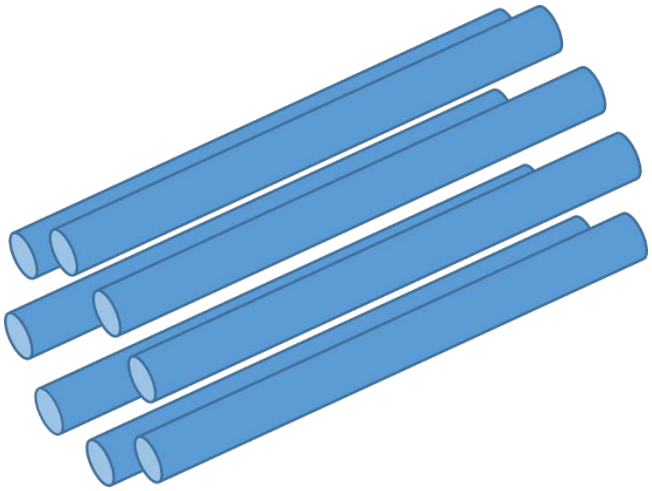

Figure 2.4: Sketch of the RF octopole.

2.1.4 RF quadrupole mass filter

As we know, ESI sources do not only produce the target ions but also other ions, such as solvent ions, unknown ions due to impurities in the solution. On the other hand, some fragment ions from the target ions can also be produced because of the multiple collisions with the residual gas molecules. Therefore, it is necessary to select the target ions of a given charge state before accumulation in the Paul trap. A quadrupole mass filter is used to select the ions with a controlled mass-to-charge (*m/z*) ratio. The quadrupole mass filter consists of 4 cylindrical stainless-steel rods, as shown in Figure 2.5. The RF peak-to-peak voltage and the DC voltage are supplied by a commercial quadrupole power supply (150QC, Extrel). The power supply is based on a self-oscillating circuit. It adjusts the output frequency over a wide range of capacitive loads.

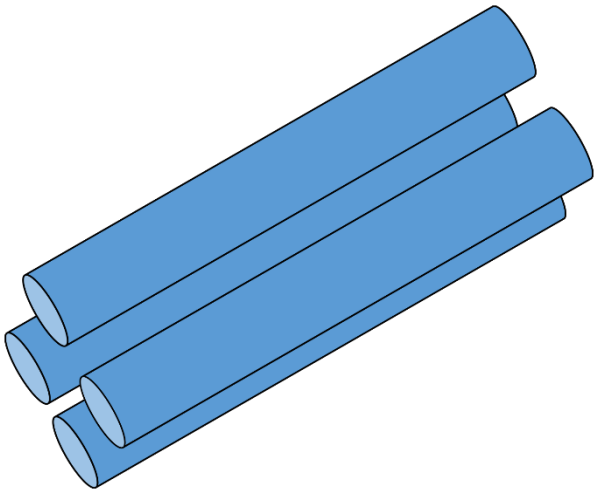

Figure 2.5：Sketch of the RF quadrupole mass filter.

The quadrupole mass filter can be used in two modes. In the RF ion guide mode, it operates in a similar way to the RF octopole described just before, and thus all ions in a wide range of *m/z* go through. In the mass-selective mode, two sets of opposing quadrupole rods in the quadrupole mass filter can be biased with different DC voltages, while maintaining the same RF amplitude and frequency. According to Mathieu's equations, for one set of DC voltages, only ions with one specific mass-to-charge ratio has a stable trajectory, the others will be unstable. This allows the present quadrupole selecting only one *m/z* up to 2000.

2.1.5 RF ion trap

Since the ion flux produced by the ESI source is relatively low, it becomes necessary to increase the ion density before irradiation. By doing so, we are able to increase the signal-to-noise ratio for our irradiation experiments. This is why the quadrupole mass filter is followed by a 3D ion trap, also known as a Paul trap. It allows to accumulate the ions into a dense cloud.

As shown in Figure 2.6, the RF ion trap has 3 hyperbolic electrodes. One is a ring where the RF field is applied (V_{dc} = 0; frequency = 1 MHz; V_{ac} from 0 to 2000 V). Two caps called injection and extraction electrodes are placed on each side of the central ring. The caps are connected to ground potential. Positively- and negatively-charged ions in a range of *m/z* are trapped: both the minimum and maximum *m/z* values increase with Vac, therefore when the precursor ion has a high *m/z*, small and/or highly-charged fragments cannot be trapped. For Vac = 2000 V, with the present Jordan Paul trap and power supply, the minimum value is around 150.

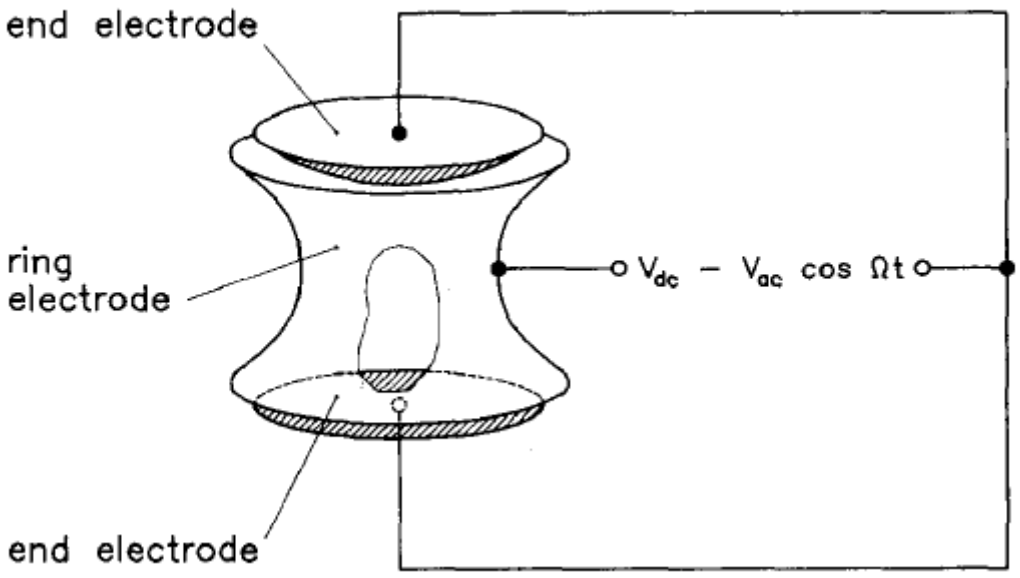

Figure 2.6: Sketch of the RF ion trap. Reprinted from H. Winter et al., American Journal of Physics 59, 807–813 (1991), with the permission of AIP Publishing.

The holes in the center of the end caps are aligned with the central axis from the ESI source to the TOF mass spectrometer, to inject and extract the ions, and there are also holes in the central ring that are perpendicular to the axis from the ESI source to the TOF mass spectrometer. These latter holes let the photon beam or ion beam go through the trap.

The base pressure of the ion trap chamber is usually around 1×10^{-8} mbar. A pulsed solenoid valve delivers 50-100 ms pulses of helium buffer gas into the trap through a hole in the ring electrode. The helium gas pulses are synchronized with the ion bunches from the upstream components. It increases the trapping efficiency by reducing the excess kinetic energy of the ions through collisional cooling. It also decreases the ion cloud size in the Paul trap to improve the final extraction to the TOF mass spectrometer. After the injection of the ions, the ESI beam is blocked by a repulsing voltage to prevent the ions from entering the trap. The accumulated ions are then exposed to the photon beam or ion beam for a well-defined time controlled by a pulse generator. To avoid multiple interactions of the projectile beam with the same target molecular ion, the irradiation time is set to consume only a maximum of 10% of precursor ions. Typical exposure time is about several hundreds of milliseconds. To cool down the irradiated energetic products, a second helium buffer gas pulse is injected after exposure. The RF voltage is then switched off and high voltages are applied to the end caps for the extraction of the cations or anions contained in the trap.

2.1.6 Reflectron TOF mass spectrometer

The reflectron TOF mass spectrometer is used to identify the *m/z* ratio of each ionic species contained in the trap after irradiation. After extraction from the Paul trap, the ions are re-accelerated and focused using a set of electrodes to which we can apply different voltages (see figure 7). The ions then enter the free-flight zone where there is no field. At the end of the chamber, they are reflected by the reflectron mirror and go back until they are finally detected at the time t_{stop} on a microchannel plate (MCP) detector. If we define the rising edge of the extraction pulse from the Paul trap as t_{start}, the time-of-flight of the ions is then $\Delta t = t_{stop} - t_{start}$. The intensity of the MCP signal as a function of Δt is called the time-of-flight spectrum.

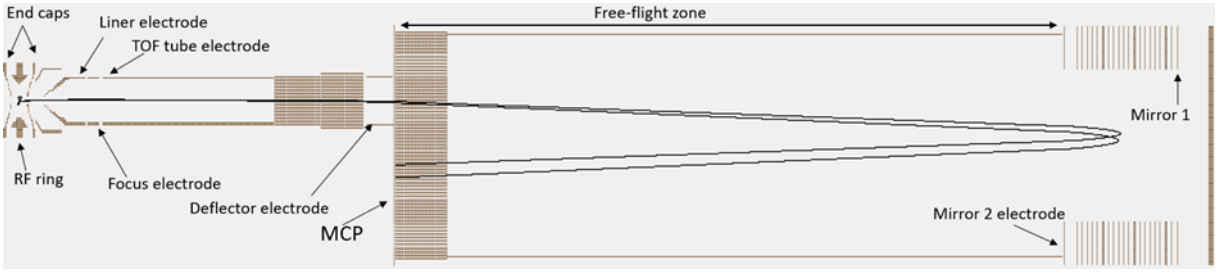

Figure 2.7: SIMION representation of the Re-TOF mass spectrometer. In black, the trajectory of two ions with different initial positions and velocity vector orientation when they exit the Paul trap.

The time-of-flight of an ion depends on its *m/z* ratio. Therefore, one can get a mass spectrum from a time-of-flight spectrum. In fact, when an ion initially at rest is accelerated by a uniform electric field of amplitude E, Newton's second law gives:

$$ma = qE$$

where m is the mass of the ion, a is its acceleration along the electric field axis and $q = ze$ is the charge of the ion.

Therefore, the position of the ion after a time Δt is given by

$$x(\Delta t) = \frac{zeE}{2m}\,\Delta t^2$$

Thus, the measurement of the time-of-flight Δt of an ion at a given position x makes it possible to obtain its mass-to-charge ratio by

$$\frac{m}{z} \propto \Delta t^2$$

Based on the relation shown above, one can transform the time-of-flight spectrum into a mass spectrum after a calibration.

By adding an electrostatic ion mirror at the end of the drift tube, it is possible to increase the flight distance and improve mass resolution by reducing the spread of flight times due to the different kinetic energies or starting positions of the ions.[74] As shown in Figure 2.7, the principle is to make the ions bounced in backward direction by imposing a force opposite to their velocity vector thanks to a constant and homogeneous electric field, created by electric potentials applied to parallel electrodes. Thus, for the ions with the same mass-to-charge ratio, the faster ones will penetrate deeper into the reflectron and spend more time in it than the slower ones. In this way, the initial dispersion in kinetic energy of the ions is compensated. As a result, time focusing of ions with the same mass-to-charge ratio on the detector is achieved and resolution is improved compared to a linear TOF mass spectrometer without the ion mirror. The resolution of the linear

TOF spectrometer before adding the reflectron is about $m/\Delta m$ = 300 at a mass of 555.[75] After adding the reflectron, the resolution has been improved to about $m/\Delta m$ = 2800.[76]

The ions are finally detected by a chevron-type double microchannel plate (MCP) detector. Each MCP has a regular array of very small tubes (microchannels) from a side of the plate to the other. The diameter of the microchannels is 12 micrometers in the MCP of Paultje. Each channel serves as a continuous-dynode electron multiplier. The MCP can detect ions and electrons, and if of sufficient energy, neutrons and photons. The front/back sides of the detector are biased at -5/-3 kV for detecting positive ions, and +3/+5 kV for negative ions.

2.1.7 Time sequence of the Paultje operation

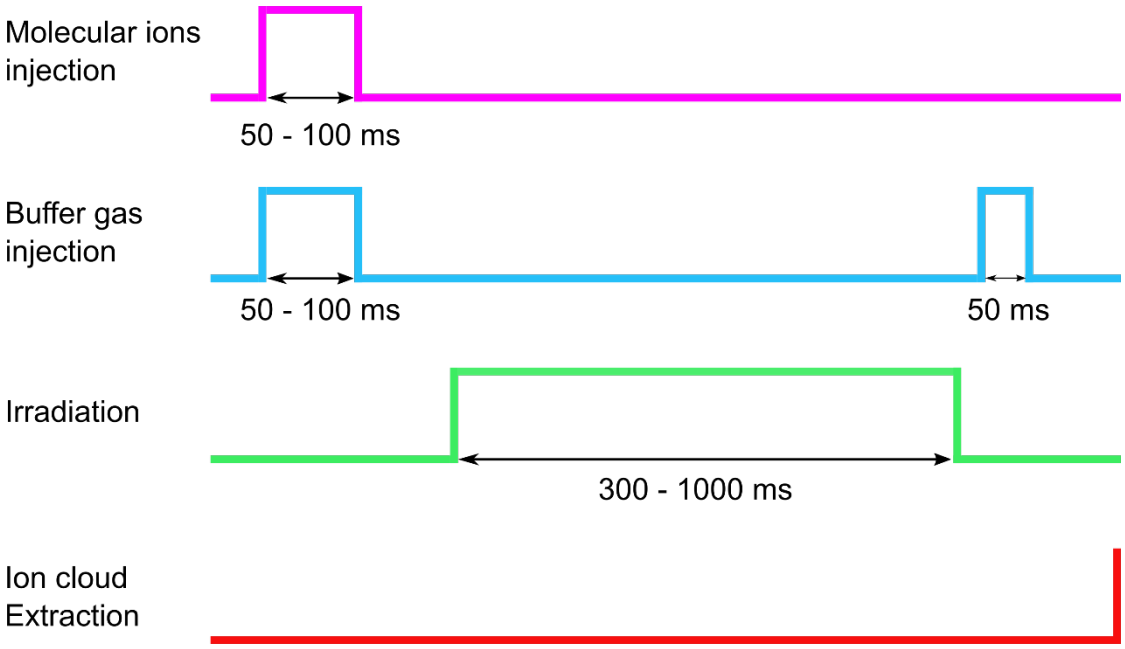

Figure 2.8: Time sequence of the Paultje operation.

A time sequence of a complete cycle is shown in Figure 2.8. First, the molecular ions are injected into the Paul trap tens of milliseconds after the previous extraction. It usually lasts for 50 – 100 ms. The buffer gas is also sent during the same time and the same duration to cool down the molecular ions before irradiation. To avoid the collision between the buffer gas and the molecular ions during irradiation, we need to wait for 50 – 100 ms to reduce the buffer gas pressure before sending the photon or ion beam to the trap. The irradiation time depends on a number of factors and is usually between 300 to 1000 ms but can be increased to several seconds (see Chapter 4). Soon after irradiation (tens of ms), the second buffer gas is injected to the trap

to cool down the molecular ions again for 50 ms. At the end of the cycle, the ions are extracted from the trap and sent to the TOF mass spectrometer.

2.2 Synchrotron user facilities

Synchrotron radiation facilities are those that use magnetic fields to force the electrons or other charged particles moving at relativistic speeds to follow curved trajectories, in which case, the electrons or other charged particles emit electromagnetic radiation in the direction of their motion.[77] This radiation is called synchrotron radiation. To date, there are more than 50 synchrotron radiation sources and free-electron laser facilities in the world, including BESSY II (Berlin, Germany), PETRA III (Hamburg, Germany), SOLEIL (Paris, France), ESRF (Grenoble, France), NSRL (Hefei, China), and SSRF (Shanghai, China). The number of these facilities is still increasing and an updating list of all the synchrotron radiation sources can be found on the website of light sources.[78]

The Paultje setup was interfaced with the XUV beamline P04[79] at the PETRA III synchrotron light source facility (Hamburg, Germany) to perform the experiments described in Chapter 4. PETRA III has a 2.3-kilometer-long storage ring. This ring was initially used as an electron-positron collider for particle physics experiments. It also served as a pre-accelerator for a larger HERA ring. Now this ring is one of the world's brightest X-ray radiation sources based on storage ring. To meet the great needs of researchers, PETRA III has built 25 beamlines with almost 60 measuring stations.

Our experiments target on gas-phase molecules of very low density. Therefore, very high photon flux is required to get measurable signals. The beamline of P04 at the PETRA III provides photon fluxes up to 5×10^{12} photons per second. It also has a quite wide energy range, from 250 eV to 3000 eV, which covers the energy range we need in our experiments (288-300 eV in carbon K-edge and 2143-2178 eV in phosphorus K-edge with energy resolution 0.5 eV and 8 eV, respectively).

The photon energy resolution is controlled by the size of the exit slits after the last mirror (details in Section 4.2.1). The photon energy is controlled via the P04 beamline panel where we can set the energy value directly. The photon beam diameter is of the order of 100 μm where the Paultje setup was installed (at the focus it is 12 μm but we go out of the focus to get a better overlap between photons and precursor ions). To further optimize the overlap between photons and precursor ions, we first use a white light to do a rough alignment, by making the white light to pass through a hole in the RF ring electrode of the Paul trap. Then we do a fine alignment by

measuring the signal of the precursor ions, which means that we move the photon beam using the mirrors of the beamline until we get the maximum signal of the precursor ions after interaction with the photon beam.

2.3 Heavy ion accelerator

Heavy ion accelerators can accelerate the particles and turn them into pure and intense beams of a desired energy.[80] The resulting heavy ion beams can then be used for many scientific purposes, from the synthesis of "artificial" elements to nuclear physics, biology and medicine.[80]

The Paultje setup was connected to the IRRSUD beamline at the GANIL facility to perform the experiments described in Chapter 5. GANIL is a heavy ion research center in Caen, France and IRRSUD is one of its beamlines. The IRRSUD beamline can provide ions from carbon to uranium. These ions are produced in an electron cyclotron resonance (ECR) source and then accelerated by one of the injector cyclotrons (C01 or C02). The kinetic energy of the ions is on the order of 1 MeV/amu, and the typical current intensity is a few microamperes at the exit of the beamline. We need such high intensities for our irradiation experiments because our target is diluted and we lose much intensity (about two orders of magnitude) when the beam passes through the Paul trap.

A $^{13}C^{3+}$ ion beam at 0.8 MeV/amu was used in our experiments in Chapter 5. A Faraday cup was used to detect the intensity of the carbon ion beam that goes through the Paul trap. A tube (shown in Figure 2.9) with a 2 mm diameter hole (Hole A) was placed in front of the hole in the trap ring electrode, to avoid the production of secondary charged particles following ion-impact on the ring electrode. The other hole B is to control the diameter of the carbon ion beam. The intensity of the $^{13}C^{3+}$ ion beam was 10 µA before entering the Paul trap and became 20 ~ 60 nA after going through the Paul trap and being detected by the Faraday cup. By means of an electrostatic deflector (located after the ion source and before acceleration by the cyclotron), we were able to pulse the carbon ion beam, and control the irradiation time. The irradiation time was between 600 ms to 1200 ms. The optimization of the overlap between carbon ions and precursor ions is the same as the overlap between photon beam and precursor ions (described in Section 2.2).

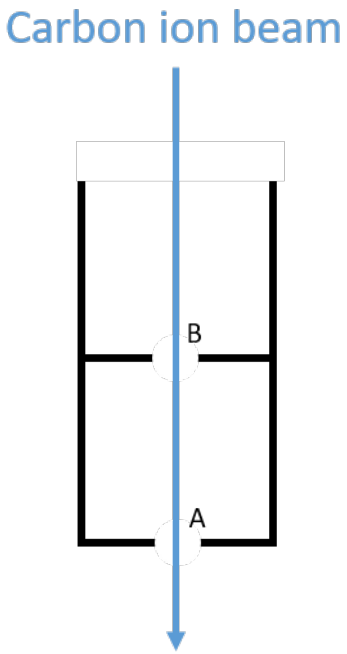

Figure 2.9: The tube in front of the hole in the trap ring electrode.

2.4 TIMS-TOF Pro mass spectrometer

The mass spectra and ion mobility spectra in Chapter 3 were obtained using a commercial setup named TIMS-TOF Pro (Bruker Daltonics), provided by the Proteogen Platform at University of Caen Normandy. The setup allows for the study of gas-phase ionic biomolecules, by getting the mass spectrometry (MS) spectra and tandem mass spectrometry (MS/MS) spectra of isolated precursor ions. At the same time, thanks to an additional ion mobility analyzer, it can determine the collisional cross sections of these ions, which is directly related to their geometric structure.

In this section, the main features of the setup used for production, accumulation, trapping, collision, as well as mass-to-charge ratio and ion mobility analysis of molecular ions are discussed. It should be noted that since it is a commercial setup, its specifications are not published in detail. The description here is mainly based on some publications from Matthias Mann's group[81–83], it may differ a bit from the one we use, but the main structure and principle are the same.

As shown in Figure 2.10, the TIMS-TOF Pro mass spectrometer consists of six parts: an ion interface (source), a dual trapped ion mobility spectrometry (TIMS) analyzer, an ion transfer multipole, a quadrupole, a collision cell and a Time-of-Flight (TOF) analyzer.

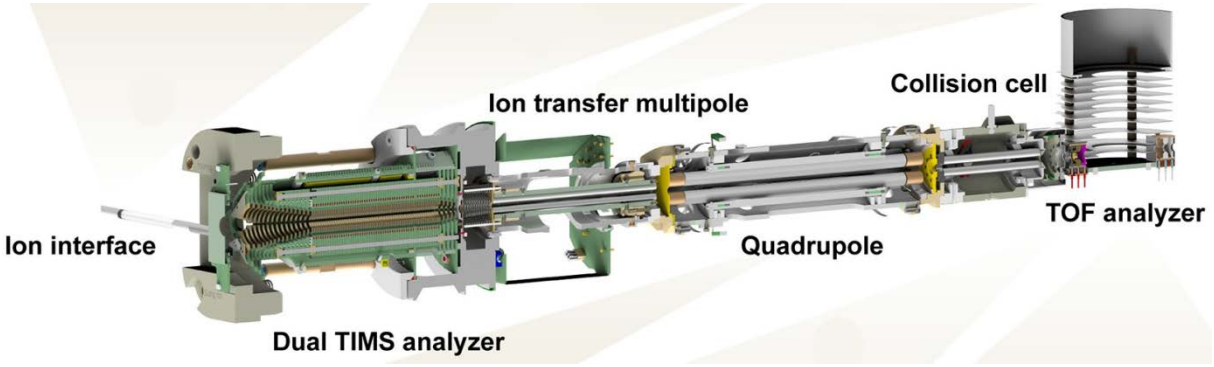

Figure 2.10: Scheme of TIMS-TOF Pro Mass spectrometer. Reprinted from Meier et al., 2018, Molecular & Cellular Proteomics 17, 2534–2545 (Open access).

First of all, ions dissolved in solution are injected into a modified nano ESI source (CaptiveSpray, Bruker Daltonics) through a syringe. Then a spray voltage with a capillary temperature of 180°C is typically employed for ionizing. Heated nitrogen gas is used as the dry gas to effectively eliminate the solvent of the sample. After ionizing in the ion interface region, the desolvated ions enter in the vacuum system through the capillary and are deflected by 90º (see Figure 2.11). Next, as shown in Figure 2.11, they enter in the dual TIMS analyzer. The TIMS analyzer consists of a set of electrodes and is divided into three parts: the entrance funnel, the TIMS tunnel (96 mm funnel) and the exit funnel. In the TIMS analyzer, they are focused in an electrodynamic funnel, and trapped in the first part of the TIMS tunnel. The TIMS tunnel consists of stacked printed circuit boards (PCBs) with an inner diameter of 8 mm and a total length of 96 mm[82]. The length of the tunnel is more than twice of the first-generation prototype, which is 46 mm. The doubled length of the tunnel makes it possible to include a new “ion accumulation trap” upstream of the analysis region. In particular, the PCB electrodes can form a stacked multipole in the direction of ion transmission. Typically, a RF potential of 350 V_{pp} is applied to the electrodes to confine the trapped ions radially. The whole TIMS tunnel can be electrically separated into two regions (dual TIMS), the storage region and the analysis region. The first region is utilized as an ion accumulation trap which mainly stores all ions entering the setup. Meanwhile, the second region is used to handle the trapped ion mobility analysis.

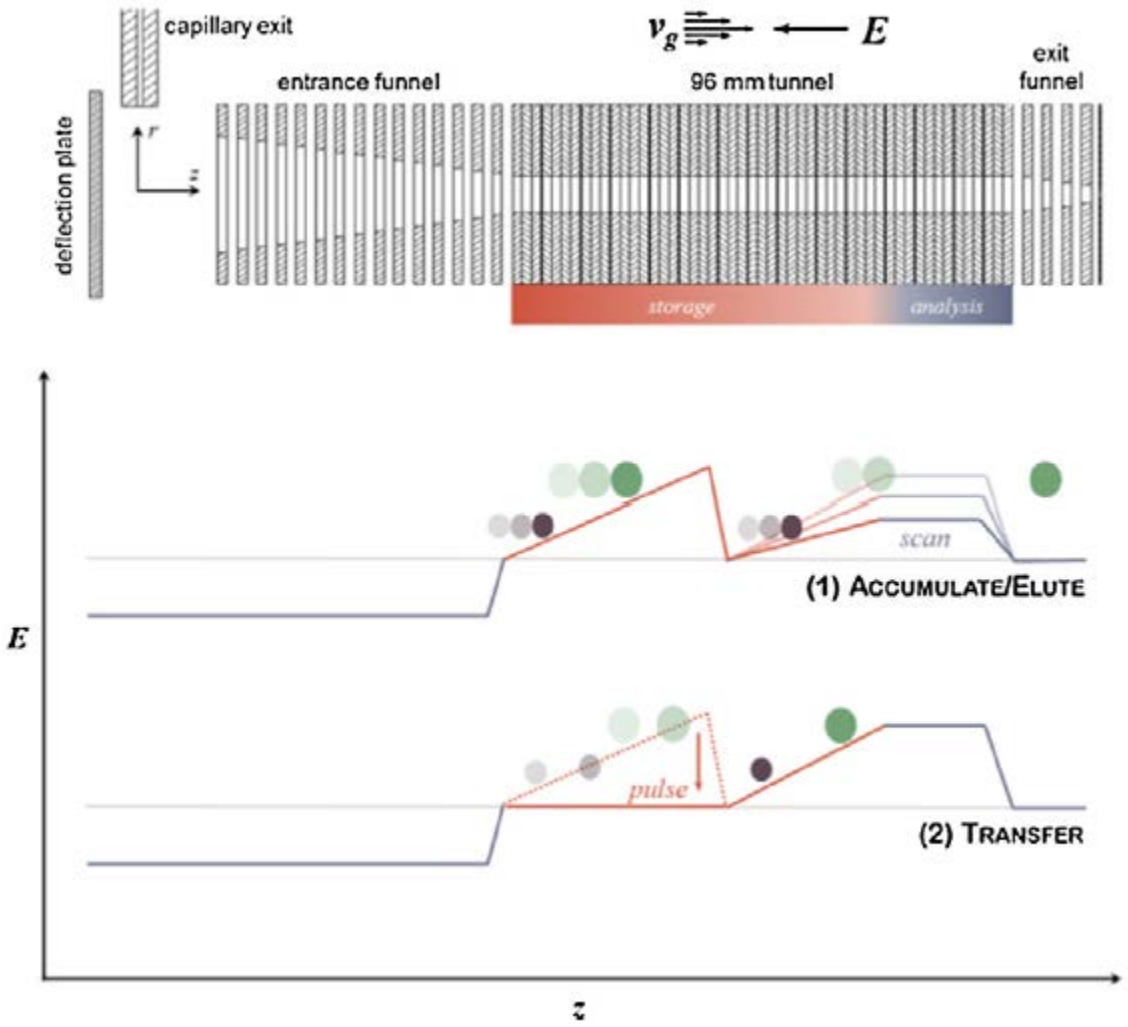

Figure 2.11: Detailed schematic of the Dual TIMS analyzer (top) and its general operation mode (bottom). Reprinted from J.A. Silveira et al., International Journal of Mass Spectrometry 413 (2017) 168–175 Copyright (2017), with permission from Elsevier.

In both the storage and the analysis region of the TIMS tunnel, the RF field (potential: 350 V_{pp}) is superimposed from entrance to exit of each region with an increasing DC voltage gradient creating an electrical field (E) in the longitudinal axis. On the other hand, nitrogen gas (the drift-gas, abbreviated as "g") from the ESI source mixed with ambient air is introduced into the tunnel through the capillary and flows through the tunnel in the opposite direction compared to the electric field (for positive ions, *cf.* Figure 2.11). In this way, ions in the tunnel are simultaneously dragged by the incoming gas flow and repulsed by the electrical field.

Under these two counteracting forces, ions in the storage region finally end up staying at a position along the longitudinal axis where these two forces are equal, while being radially confined by the RF field. Since the drag force is proportional to the collisional cross section Ω,[83,84] ions with different collisional cross sections (all other parameters being constant) are trapped at different positions along the longitudinal axis. More specifically, ions with larger

collisional cross sections are trapped closer to the exit of the tunnel while ions with smaller collisional cross sections are trapped closer to the entrance of the tunnel. In addition, because the counteracting force from the electrical field is proportional to the charge state *Q*, ions with lower charge states (all other parameters being constant) are closer to the exit of the tunnel, and *vice versa*. These two factors are included in the Mason-Schamp equation[85–88], where ion mobility K_0 can be calculated (Equation (1)). In brief, ions with high ion mobility stay closer to the entrance of the tunnel and the other way around (see Figure 2.12).

$$K_0 = \frac{3Q}{16N}\sqrt{\frac{2\pi}{\mu k_B T}}\frac{1}{\Omega} \qquad (1)$$

Here, *N* is the drift-gas number density, μ is the reduced mass of the ion and drift gas, k_B is the Boltzmann constant, *T* is the drift-gas temperature, and K_0 is the reduced ion mobility.

After a certain accumulation time, by applying a proper DC gradient to the electrodes of the storage region, the electric field drops to 0 (see Figure 2.11), so that all accumulated ions are transferred to the analysis region due the drift-gas flow. After this transfer, the voltages are set back to their original values, in order to create a linearly increasing electric field that allows the storage region to be filled again. Meanwhile, the transferred ions are eluted in the analysis region, by means of a progressive decrease of the maximum electric field value at the end of the analysis region ("scan" in Figure 2.11). Ions with small ion mobility are thus extracted first. It makes the accumulation and analysis to happen at the same time. By making the accumulation and analysis time equal in both TIMS parts, the accumulating and analyzing process are run in parallel instead of in series. In this way, if the time for ion transfer is negligible, the system can run in a 100% duty cycle. The time for ion transfer between the two parts of TIMS tunnel is 2 ms. Thus, it does not influence the total ion utilization for typical ramp and accumulation times (approximately 25 ~ 200 ms). Eluted ions then enter into the exit funnel and are focused there. After, they pass through the ion transfer multipole chamber and then enter in the quadrupole. Precursor ions can be selected by the quadrupole mass filter for the optional following fragmentation in the collision cell (see Figure 2.12). In the collision cell, nitrogen gas is used for fragmentation which is necessary for MS/MS spectra. This fragmentation is usually called collision-induced dissociation (CID). To achieve the CID, the selected ions are given a controlled kinetic energy (called "collision energy") by the electrical field at the entrance of the collision cell and then collide with neutral nitrogen molecules. During the collision, part of the kinetic energy is transformed into internal energy. Thereby, the internal energy can break the

bonds in the ions and cause fragmentation. Smaller fragment ions are produced and can be analyzed later.

However, if the setup is run in MS mode, the ions are not selected by the quadrupole mass filter and no gas is injected in the collision cell.

After the collision cell, the ions (both in MS mode and MS/MS mode) enter in the orthogonal TOF analyzer, where they are accelerated and then go through a field-free drift region. To compensate the differences in the initial kinetic energy of the ions and increase the mass resolution, a reflectron is used here. The ions are finally detected by a microchannel plate (MCP) detector coupled to a digitizer.

In the MS/MS analytical part, it worth noting that the setup can perform analysis in a Parallel accumulation-serial fragmentation (PASEF) mode. Traditionally, MS/MS experiments only select one precursor out of the ions eluted from the TIMS tunnel while other ions with different *m/z* are wasted (Figure 2.12, upper panel). However, in this PASEF mode, since the release of ions from the TIMS device is controllable and the cross sections of ions are approximately correlated with precursor mass[89], MS/MS experiments in this setup are able to use several precursors in one scan, with mass selection of each precursor by the quadrupole. In particular, the quadrupole is positioned at the *m/z* of a precursor eluted from TIMS tunnel, and then is fast enough to move to the next *m/z* as soon as it has been eluted (Figure 2.12, lower panel). Thus, the total intensity of all precursors that have been trapped together is used in one TIMS scan. Therefore, this PASEF mode can greatly increase the speed and sensitivity of MS/MS by the number of precursors that are targeted by the quadrupole, because more precursors can be detected in one TIMS scan to increase the speed and the same precursors can be targeted in different TIMS scans to increase the sensitivity.

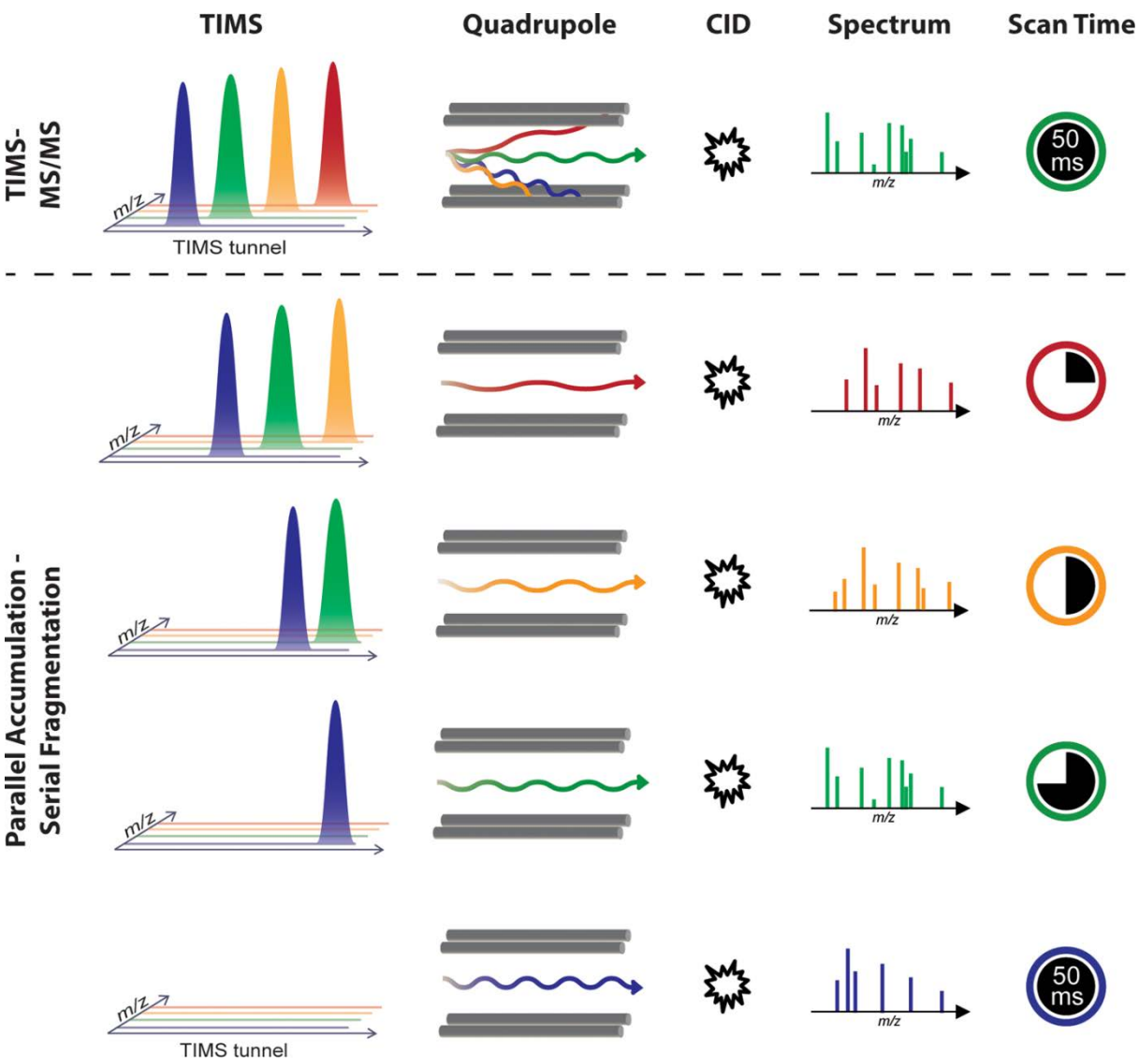

Figure 2.12: Illustration of the PASEF mode in comparison with the traditional TIMS-MS/MS operation mode. Reprinted from Meier et al., J. Proteome Res. 2015, 14, 5378−5387 (Open access).

3 Study of double strand DNA using ion mobility-tandem mass spectrometry

3.1 Introduction

Before we start to present and discuss the results of experiments where isolated dCGCGGGCCCGCG DNA strands are irradiated in an ion trap with the Paultje set-up (see section 2.1), an important step is to bring them into the gas phase and accumulate the target ions in the ion trap. However, one of our target molecules is a double strand DNA. Even though we used a soft ionization technique, it is possible that non-covalent systems like double strand DNA does not stay intact into the gas phase, and separates into single strands after dissociation of all H bonds. Moreover, even if we detect, in the MS obtained with the Paultje set-up, a peak with *m/z* corresponding to the double strand, we have no information on its geometrical structure. In order to know more about the structure and stability of the dCGCGGGCCCGCG double strand anions, we have used a commercial ion mobility-mass spectrometer, which is described in detail in Section 2.4, to validate the feasibility of bringing our DNA target into the gas phase. This setup can not only confirm the feasibility of accumulating the double strand DNA in the ion trap, but also provide the collision cross section (CCS) information, thanks to its ion mobility part.

The sequence of the DNA oligonucleotide we have chosen here is dCGCGGGCCCGCG. Because the DNA oligonucleotide dCGCGGGCCCGCG is complementary to itself, it can self-assemble into a DNA duplex in the solution. On the other hand, because this sequence contains only Guanine and Cytosine, this means the corresponding DNA duplex has only G-C pairs. Because there are 3 hydrogen bonds in G-C pairs, they are considered to be more stable than A-T pairs, which have a hydrogen bond number of 2. What's more, there have already been some studies of this sequence in the gas phase,[90–96] where we can get some useful information about it. All these advantages make the DNA oligonucleotide dCGCGGGCCCGCG an ideal sample for our experiments.

3.2 Experimental details

3.2.1 Ion mobility-tandem mass spectrometry

To study the deprotonated double strand dCGCGGGCCCGCG DNA in the gas phase, we used the TIMS-TOF pro ion mobility-tandem mass spectrometer (TIMS-TOF pro, Bruker Daltonics, described in Subsection 2.4).

The apparatus was calibrated every week to ensure that the mass precision was better than 1 ppm. The spray voltage was -1000 V and the capillary temperature was 150 ^{o}C. The dry gas (nitrogen) flow rate was 8.0 L/min. The flow rate of the syringe was 300 µL/h. Mass spectra were acquired in the negative mode in the 100 – 2500 *m/z* mass range. The mass spectrometer was operated in PASEF mode. A number of PASEF MS/MS scans were performed for the 5- charge state, with collision energy between 10 and 50 eV.

Because mass and ion mobility spectrometry analyses of this oligonucleotide were performed simultaneously on this commercial apparatus which couples trapped ion mobility spectrometry and time-of-flight mass spectrometry, the information about the mass over charge ratio (*m/z*) and the ion mobility of the sample ions can be acquired at the same time. Specifically, we mainly focus on three kinds of data. The first is the raw mass spectrum, which shows the abundance and *m/z* of all the ions produced by the ESI source for a given DNA sample solution. The second is the tandem CID mass spectrum of a given selected ion, which gives information on its lowest-energy fragmentation channels. The third is the mobilogram of a given selected ion. The mobilogram is a spectrum which presents the intensity of the selected ion with an *m/z* as a function of the reciprocal of ion mobility. Specifically, since all ions have to go through the dual TIMS tunnel, the arrival time of each ion is detected by the ion mobility analyzer. The mass spectra of ions with the same arrival time are measured simultaneously. The data analysis system then reconstructs the ion mobility spectra by recording the different ion mobilities of the ion with the same *m/z*. Thus, we are able to obtain the ion mobility spectrum of one ion by selecting one peak from the mass spectrum, and *vice versa*. The ion mobility spectrum is named as "mobilogram" in the software system. All these spectra can be acquired from the commercial software DataAnalysisViewer Version 5.2. from Bruker Daltonics.

The DNA sample was prepared by dissolving a powder of the dCGCGGGCCCGCG oligonucleotide of up to 85% purity (Reverse-Phase HPLC purified, Eurogentec, Seraing, Belgium) without further purification in a mixed solvent of 50% methanol (Laboratory reagent, ≥ 99.6%), 50% deionized water and 3% 3.9 M ammonium acetate (produced by mixing 5.0 M

ammonium hydroxide and 100% acetic acid (analytical reagent) together, pH = 7.0). The final concentration of the dCGCGGGCCCGCG oligonucleotide was 10 μM.

3.2.2 Circular dichroism spectroscopy

To obtain information on the geometrical structure of the DNA oligonucleotide dCGCGGGCCCGCG in our ESI solutions, we performed circular dichroism (CD) spectroscopy. The concentration of this DNA solution was 50 μM with 2% 5 M ammonium acetate added. The solvent for the DNA solution was a mixture of 50% methanol and 50% deionized water. A quartz cuvette with a path length of 1 mm was used to hold the DNA solution sample. We used the Chirascan™ Circular Dichroism Spectrometer (Applied Photophysics Ltd, UK) at Wuhan University to record the circular dichroism spectrum. The scanning range was from 220 nm to 320 nm. The scanning speed was 60 nm/min, and the response time was 0.5 s.

The corresponding CD spectrum is shown in Figure 3.1, there is a CD maximum near 270 nm, a CD minimum near 250 nm, and a cross-over point (from negative to positive intensity) near 260 nm. It is a typical duplex DNA feature in a CD spectrum.[97–99] For example, G. Reid Bishop and Jonathan B. Chaires have obtained a CD spectrum of *E. coli* DNA.[97] The *E. coli* DNA is a duplex DNA and has a very similar CD spectrum with a minimum near 250 nm and a maximum near 280 nm, and a cross-over point at 260 nm (shown in Figure 3.2). Donald M. Gray *et al.* also have recorded a similar CD spectrum of another duplex DNA, T7 phage DNA.[99] Thus, it is clear that the ESI solution most probably contains dimers of dCGCGGGCCCGCG oligonucleotide with a double helix structure. But we cannot estimate the percentages of the double helix DNA and the single strand DNA in the solution.

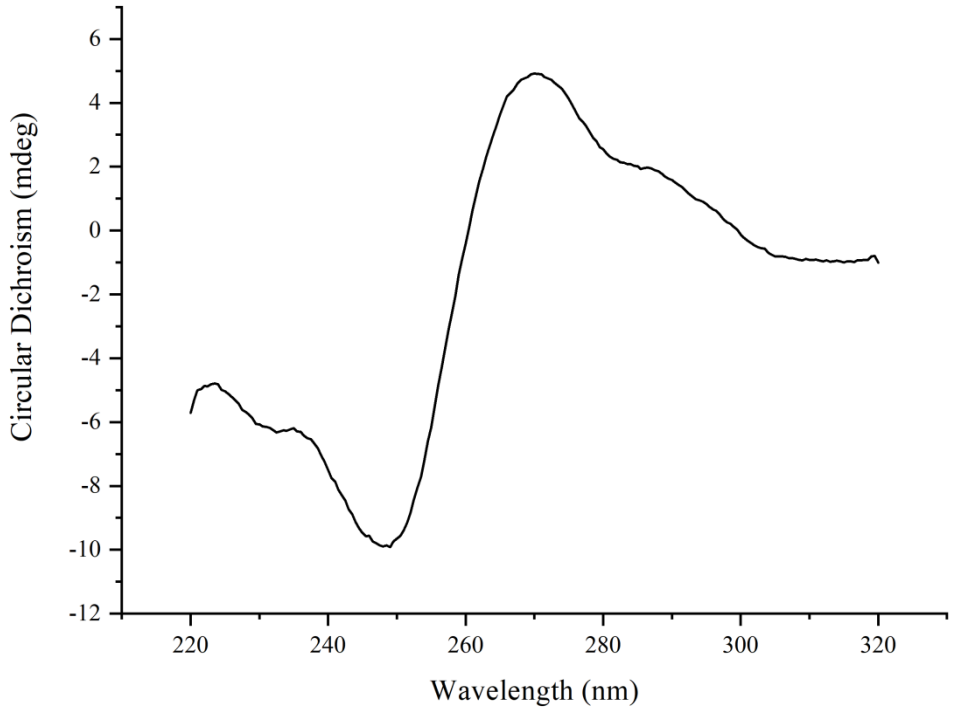

Figure 3.1: Circular dichroism (CD) spectrum of a solution of the dCGCGGGCCCGCG oligonucleotide (see the experimental section for details).

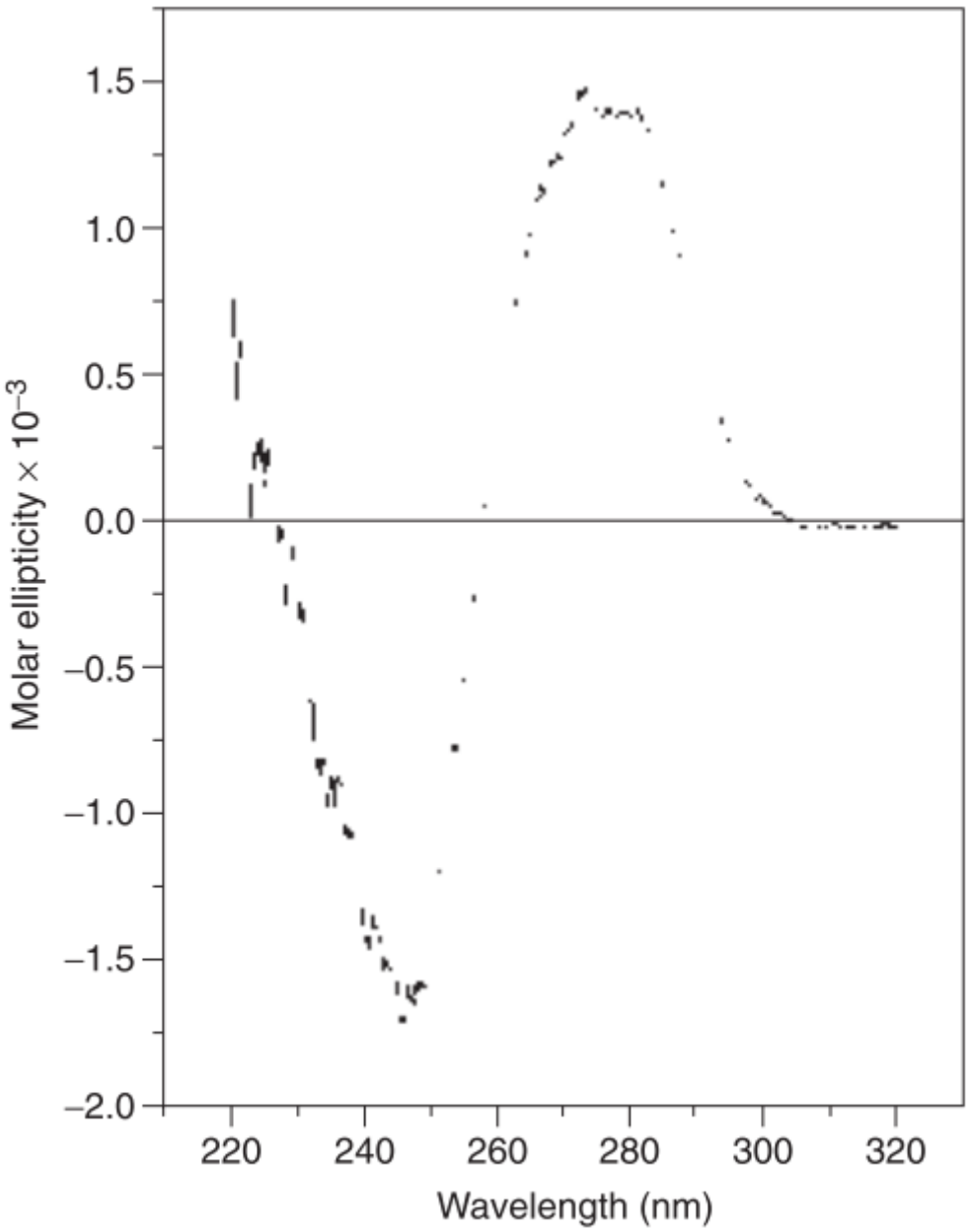

Figure 3.2: Circular dichroism spectrum of E. coli DNA in 1 mM Na_2EDTA, 185 mM NaCl, and 6 mM Na_2HPO_4/2 mM NaH_2PO_4, pH 7.0. Reprinted from Bishop et al., Curr. Protoc. Nucleic Acid Chem. 2002, 7.11.1-7.11.8, with the permission of John Wiley and Sons.

3.3 Results and discussion

3.3.1 Tandem mass spectrometry and collision-induced dissociation of dCGCGGGCCCGCG oligonucleotide negative ions

Following the experimental procedure described in section 3.2.1, we recorded the full mass spectrum of the negative ions created by the source from the dCGCGGGCCCGCG oligonucleotide solution: it is shown in Figure 3.3. It contains many peaks of different ions with different charge states over a wide *m/z* range because the setup is run in MS mode, and the ions

are not selected by the quadrupole mass filter. Some of the most intense can be assigned to anions of the dCGCGGGCCCGCG oligonucleotide. One is quadruply deprotonated dCGCGGGCCCGCG, written $[dCGCGGGCCCGCG\text{-}4H]^{4-}$, around 911 *m/z*, another is $[dCGCGGGCCCGCG\text{-}3H]^{3-}$ around 1215 *m/z*. The third one is the five-fold deprotonated dimer of dCGCGGGCCCGCG, namely $[d(CGCGGGCCCGCG)_2\text{-}5H]^{5-}$, around 1458 *m/z*. The quadruply deprotonated dimer of dCGCGGGCCCGCG, namely $[d(CGCGGGCCCGCG)_2\text{-}4H]^{4-}$, around 1822 *m/z* was also found in this full mass spectrum, though its intensity is very low. The isotopic patterns of these four ions are shown in Figure 3.3: the *m/z* gap between the peaks is consistent with their respective charge state.

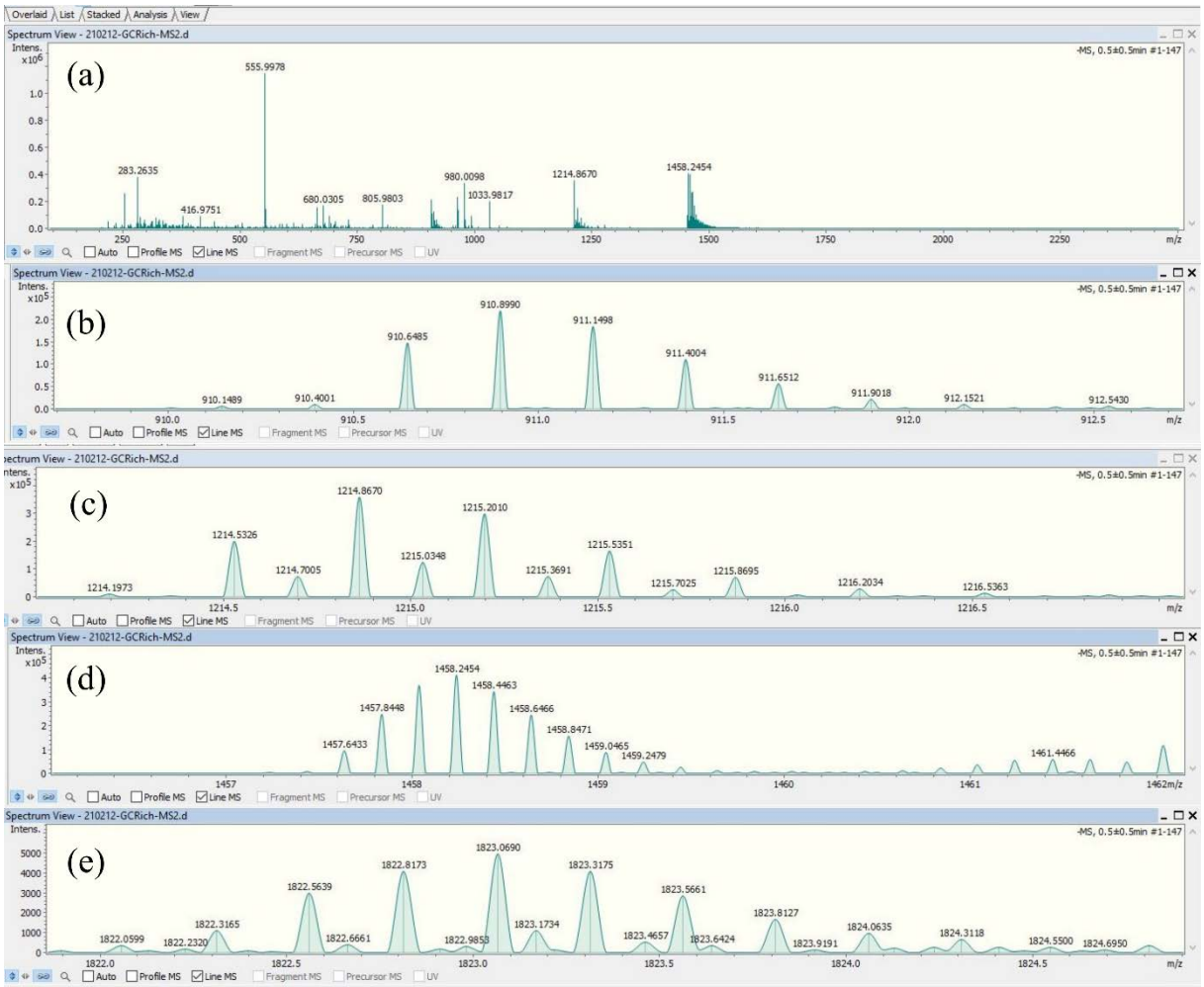

Figure 3.3: (a) Full mass spectrum of dCGCGGGCCCGCG oligonucleotide negative ions produced by ESI (see the text for details). (b-e): zoom into the regions corresponding to peaks attributed to the following anions of the dCGCGGGCCCGCG oligonucleotide with calculated monoisotopic m/z: $[dCGCGGGCCCGCG\text{-}4H]^{4-}$: m/z 910.6504 ; $[dCGCGGGCCCGCG\text{-}3H]^{3-}$: m/z 1214.5365 ; $[d(CGCGGGCCCGCG)_2\text{-}5H]^{5-}$: m/z 1457.6454; $[d(CGCGGGCCCGCG)_2\text{-}4H]^{4-}$: m/z 1822.3087.

It is worth noting that we also observed a bit of deprotonated dimer of dCGCGGGCCCGCG with 6 negative charges, namely $[d(CGCGGGCCCGCG)_2\text{-}6H]^{6-}$ in Figure 3.3(c). Since the mass spectrometer distinguishes different ions by mass over charge ratio, we can deduce that

in the MS the peaks assigned to $[d(CGCGGGCCCGCG)_2\text{-}6H]^{6-}$ will be in the same region as $[dCGCGGGCCCGCG\text{-}3H]^{3-}$, because they have the same mass over charge ratio (double mass with double charges). However, it is still possible to distinguish these two ions by mass spectrometry with enough resolution, because of the high relative abundance of carbon in DNA (*e.g.* around 29% of the atoms are carbon for the dCGCGGGCCCGCG molecule) and the existence of ^{13}C isotopes (natural abundance of 1.1% per carbon atom[100]). Thus, the isotope patterns of these two systems are quite different, as shown in the simulations of Figure 3.4 (top). Nevertheless, one can distinguish these two ions by their isotopic patterns. A molecule with 3 charges will have its peaks separated by 0.33 *m/z*, whereas a molecule with 6 charges will have its peaks separated by 0.17 *m/z*. In bottom of Figure 3.4, we can see that the peaks of $[d(CGCGGGCCCGCG)_2\text{-}6H]^{6-}$ are of lower intensity compared to those of $[dCGCGGGCCCGCG\text{-}3H]^{3-}$. Thus, from the comparison between the simulated and experimental isotopic patterns, the relative abundance were calculated for the monomer $[dCGCGGGCCCGCG\text{-}3H]^{3-}$ (~ 60%) and dimer $[d(CGCGGGCCCGCG)_2\text{-}6H]^{6-}$ (~ 40%).

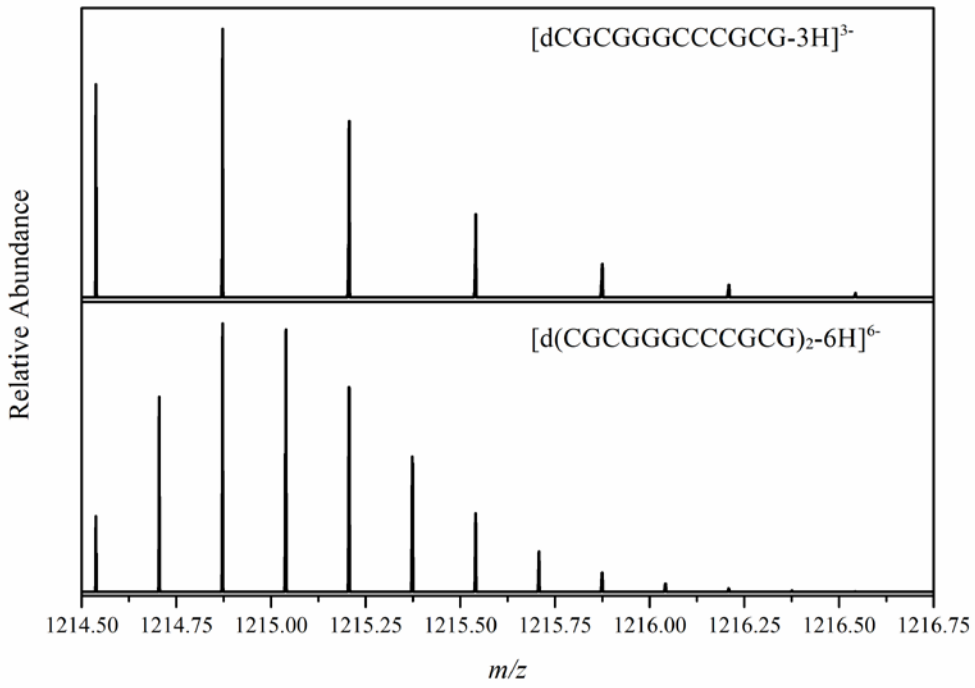

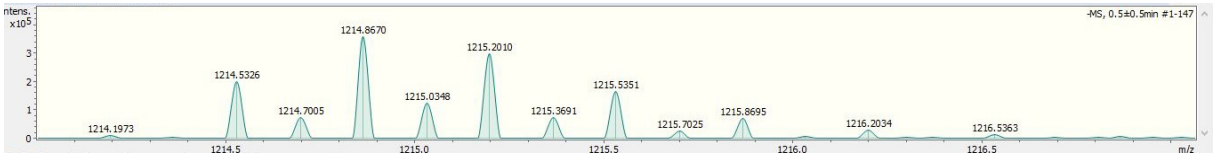

Figure 3.4: Comparison of the mass spectra in the region of the isotopic pattern of [dCGCGGGCCCGCG-3H]$^{3-}$ and [d(CGCGGGCCCGCG)$_2$-6H]$^{6-}$, simulated by Thermo Xcalibur software, resolution: 1ppm (top) and taken from the experimental data (bottom).

A similar mixture is also observed for [d(CGCGGGCCCGCG)$_2$-4H]$^{4-}$. The small peaks between the main peaks may be multimers such as [d(CGCGGGCCCGCG)$_3$-6H]$^{6-}$ (*cf.* Figure 3.3(e)). However, as the intensity of these peaks is extremely low, there is no need to consider it.

In addition, it can be seen that the zoomed mass spectra of all the ions follow the Gaussian distribution, whereas the corresponding unzoomed peaks in Figure 3.3 (a) do not. This is because the peaks in Figure 3.3 (a) contain not only the peaks assigned to the pure DNA ions as in Figure 3.3 (b-e), but also the peaks assigned to the DNA salt adducts (not zoomed).

From the results above, we can conclude that both single strand dCGCGGGCCCGCG (monomer) and double strand dCGCGGGCCCGCG (dimer) are present in the gas phase. However, we want to study the collision induced dissociation pattern of the dimer in order to obtain more information on this ion: for instance, we expect the lowest-energy channel to be the formation of two monomers due to cleavage of the H bonds. The first step is to choose the charge state of the dimer ion to be isolated. As some of the peaks assigned to [(dCGCGGGCCCGCG)$_2$-6H]$^{6-}$ fall at the same *m/z* as those attributed to [dCGCGGGCCCGCG-3H]$^{3-}$, in the following we will focus on the 1457.34 *m/z ion*, unambiguously assigned to [d(CGCGGGCCCGCG)$_2$-5H]$^{5-}$. Therefore, we operated the TIMS-TOF pro mass spectrometer in MS/MS mode to study the CID of this ion. We selected this ion with the quadrupole and transferred it to the collision cell. In the latter, the ion was impacted by nitrogen with collision energy from 10 eV/z to 50 eV/z. The resulting tandem mass spectrum at 10 eV/z collision energy is shown in Figure 3.5 (top left). As we can see, this spectrum is very “clean”, which means we can see mainly one peak around 1458 *m/z* due to the precursor. When the collision energy increases, more and more other peaks appear while the intensity of the precursor peak decreases. With collision energy increasing to 30 eV/z, (*cf.* Figure 4.4 (Top right)), we can clearly observe peaks assigned to the single strand dCGCGGGCCCGCG with 2 and 3 negative charges around 1822 *m/z* and 1215 *m/z*, respectively. It indicates that the precursor [d(CGCGGGCCCGCG)$_2$-5H]$^{5-}$ dimer was separated into two monomers due to the increase of vibrational energy brought by multiple collisions with the gas, even though it doesn't appear as the main fragmentation channel. The intensity of the monomer peak is relatively low compared to some lower *m/z* fragments. In addition, we can see many other peaks, for example assigned to the fragments a$_2$-G at 386 *m/z* and w$_2$ at 635 *m/z* that are probably due to

fragmentation of monomers after dissociation of the dimer. Surprisingly, we also observe base loss directly from the intact dimer, leading to the following ions: $[d(CGCGGGCCCGCG)_2\text{-}5H\text{-}G]^{5-}$ (guanine loss) at 1427 *m/z* and $[d(CGCGGGCCCGCG)_2\text{-}5H\text{-}C]^{5-}$ (cytosine loss) at 1435 *m/z*. Usually in CID of noncovalent complexes H bonds are cleaved preferentially: here the glycosidic bond between a base and the backbone is cleaved while at least some of the H bonds of the dimer remain intact. The same observation was made for deprotonated DNA G-quadruplexes after electron detachment due to VUV photoabsorption, but in this case it was assigned to very low barriers associated with reactions involving radicals.[66] Moreover, the intensity of peaks assigned to guanine loss is twice that of cytosine, which might also seem surprising, given that guanines and cytosine have the same abundance in dCGCGGGCCCGCG. We can also observe that the relative intensity of the precursor peak has decreased from 10 to 30 eV/z collision energy. If we plot the relative intensity of the precursor and the sum of the intensities of all the fragments (all the isotopes are taken into account) as a function of collision energy, we can see that the relative abundance of the precursor smoothly decreases while that of the fragments increases (shown in Figure 3.5 Bottom). What's more, the two curves allow us to extract the collision energy for 50% dissociation of the precursor (28 eV/z here under our experimental condition: see Figure 4.4 Bottom, where the two curves cross), which could be used in future studies to compare the stability of different DNA duplexes of similar size and charge.

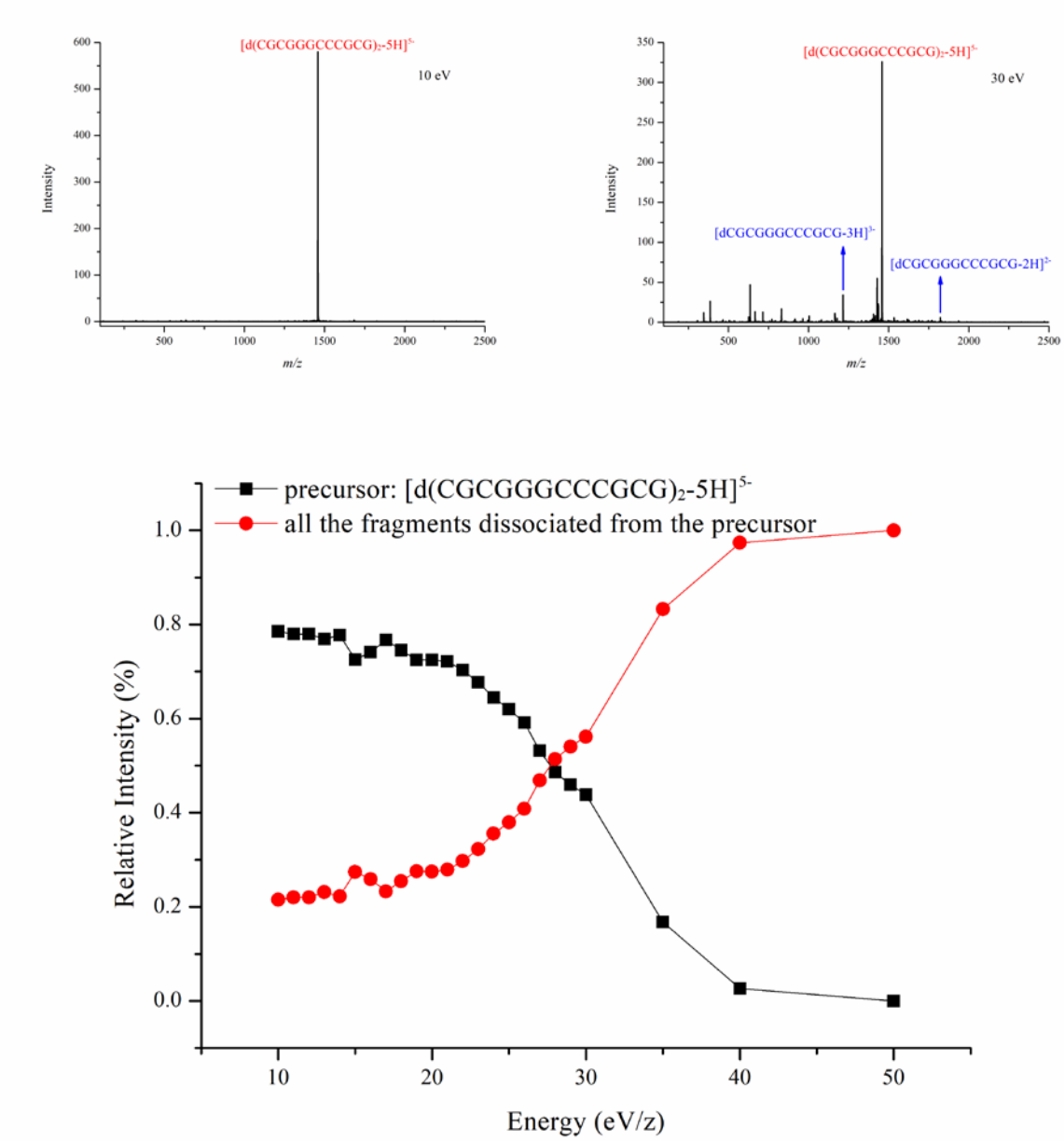

Figure 3.5: Top: Tandem mass spectra of the [(dCGCGGGCCCGCG)$_2$-5H]$^{5-}$ dimer after isolation in the QMS and collision-induced dissociation at collision voltages of 10 eV/z and 30 eV/z. Bottom: Relative intensity of the [(dCGCGGGCCCGCG)$_2$-5H]$^{5-}$ dimer precursor and all the fragments dissociated from the precursor as a function of collision voltage.

3.3.2 Ion mobility spectrometry of dCGCGGGCCCGCG oligonucleotide negative ions

In the last subsection, we have identified the d(CGCGGGCCCGCG)$_2$ oligonucleotide dimer in the gas phase by mass spectrometry and studied its dissociation pattern by tandem mass spectrometry. However, we cannot know the conformation of this dimer by mass spectrometry alone. According to a previous study using ion mobility coupled to mass spectrometry of several oligonucleotides with a similar number of base pairs (bp), the DNA duplexes are considerably more compact in the gas phase compared to the canonical solution structures.[101] Hence, we tried to identify the structure of the d(CGCGGGCCCGCG)$_2$ oligonucleotide dimer with ion mobility

spectrometry. The mobilogram of the dCGCGGGCCCGCG dimer with 5 negative charges by selecting the highest isotope peak at 1458.2454 (see Figure 3.3 d) is shown in Figure 3.6. As we can see here, there is only one main peak in the mobilogram, which indicates that there is only one main structure of this dimer. The average reciprocal of mobility ($1/K_0$) is around 0.9 V·s/cm^2. The value of the mobility of a given ion depends on the parameters of the ion mobility spectrometer, so we cannot compare this value with other reported ones.

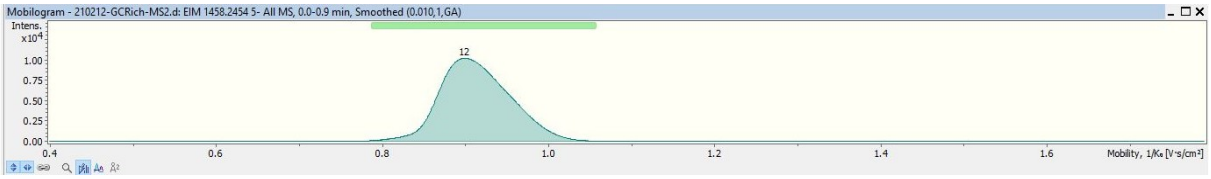

Figure 3.6: Mobilogram of the [d(CGCGGGCCCGCG)$_2$ -5H]$^{5-}$ ion.

Since the mobility of a given ion depends on the parameters of the ion mobility spectrometer, we need to transform the mobility to collision cross section Ω that is independent from these parameters, in order to plot the intensity of a given ion as a function of Ω. It will allow getting more information about the conformation of the oligonucleotide dimer ions by comparing our values with the already reported ones. According to previous studies, the collision cross section (Ω) of an ion depends on its mobility through the Mason-Schamp equation[85–88]

$$\Omega = \frac{3Q}{16N}\sqrt{\frac{2\pi}{\mu k_B T}}\frac{1}{K_0} \qquad (2)$$

Where Q is the ion charge, N is the drift-gas number density, μ is the reduced mass of the ion and drift gas, k_B is the Boltzmann constant, T is the drift-gas temperature, and K_0 is the reduced mobility. Because the ion mobility mass spectrometer provides the mobilogram by plotting the intensity of the ion as a function of the reciprocal of mobility ($1/K_0$), we can convert the reciprocal of mobility ($1/K_0$) to the collision cross section (Ω) with this equation. Since $\frac{3}{16N}\sqrt{\frac{2\pi}{\mu k_B T}}$ in Equation (2) is a constant in a given working condition, we can set a correlation coefficient C_0 as in Equation (3)

$$C_0 = \frac{Q}{\Omega K_0} \qquad (3)$$

Meanwhile, we can now calculate the value of C_0 by choosing a series of values of the collision cross section (Ω) and the reduced mobility (K_0) of some sample ions with known charges. The commercial software DataAnalysisViewer Version 5.2. from Bruker Daltonics

designed for the setup can calculate the collision cross section and the reduced mobility of the sample ions automatically based on the mobilogram, which are shown in Table 1.

Table 1: Calculation of the correlation coefficient C_0.

ion	Ω (Å^2)	1/ K_0 (V·s/cm^2)	Q	C_0 (V·s/ Å^2·cm^2)
1	923.1	0.913	5	0.00495
2	1097.0	0.904	6	0.00494
3	1148.8	0.948	6	0.00495
4	1231.1	1.017	6	0.00496
5	933.0	0.923	5	0.00495
6	864.1	1.071	4	0.00496
7	650.1	0.800	4	0.00492
8	590.4	0.971	3	0.00493

By averaging the values of C_0 given in Table 1, we obtain a value of 0.00494. Then according to Equation (3), we have

$$\Omega = \frac{Q}{0.00494 K_0} \qquad (4)$$

With Equation (4), we can convert the reciprocal of mobility ($1/K_0$) to the collision cross section (Ω). The results are shown in Figure 3.7 for the $[(dCGCGGGCCCGCG)_2\text{-}5H]^{5-}$ dimer.

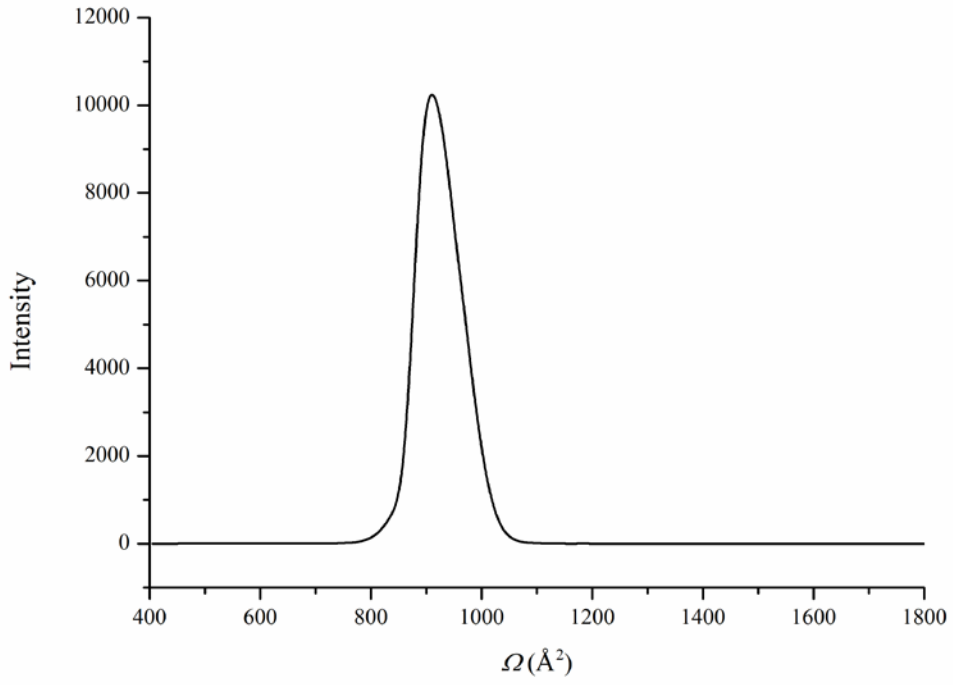

Figure 3.7: Experimental collision cross section of the most abundant isotope of the [d(CGCGGGCCCGCG)$_2$-5H]$^{5-}$ ion appearing in the mass spectrum of Figure 3.3 d.

From Figure 3.7, we can obtain the collision cross section (CCS) of the dimer of dCGCGGGCCCGCG oligonucleotide with 5 negative charges is 911 Å^2, because the a-axis value is 911 when the intensity reaches its maximum value. As reported by Porrini *et al.*,[101] the calculated cross section of the canonical B-helix of d(CGCGGGCCCGCG)$_2$ on helium is 908 Å^2. Since the cross section is obtained with nitrogen in our case, we cannot compare it with the one in helium directly. The Bush database shows that CCS values for anions and cations on helium are similar, but they are about 20% higher on nitrogen than on helium for cations of proteins.[102] It would give around 1080 Å^2 for the canonical B-helix when obtained with nitrogen gas, but we do not observe any signal at this CCS. It indicates that the conformation of the dimer of dCGCGGGCCCGCG oligonucleotide is more compact in our experiment than that of the canonical B-helix in the gas phase and is closer to the zipped helix structure of d(CGCGGGCCCGCG)$_2$, whose calculated cross section on helium is 711 ± 9 Å^2 (around 850 Å^2 on nitrogen if we consider the 20% difference between on nitrogen and on helium).[101] Porrini explained this by new phosphate − phosphate hydrogen bonds formed across both grooves in the very late stages of electrospray and the subsequent major rearrangements of the backbone as the DNA double helix is transferred from solution to the gas phase.[101] Porrini has also provided the structure figures of the B-helix and the zipped helix DNA (whose sequence is similar with ours) in the supporting information of the same article (shown in Figure 3.8).[101]

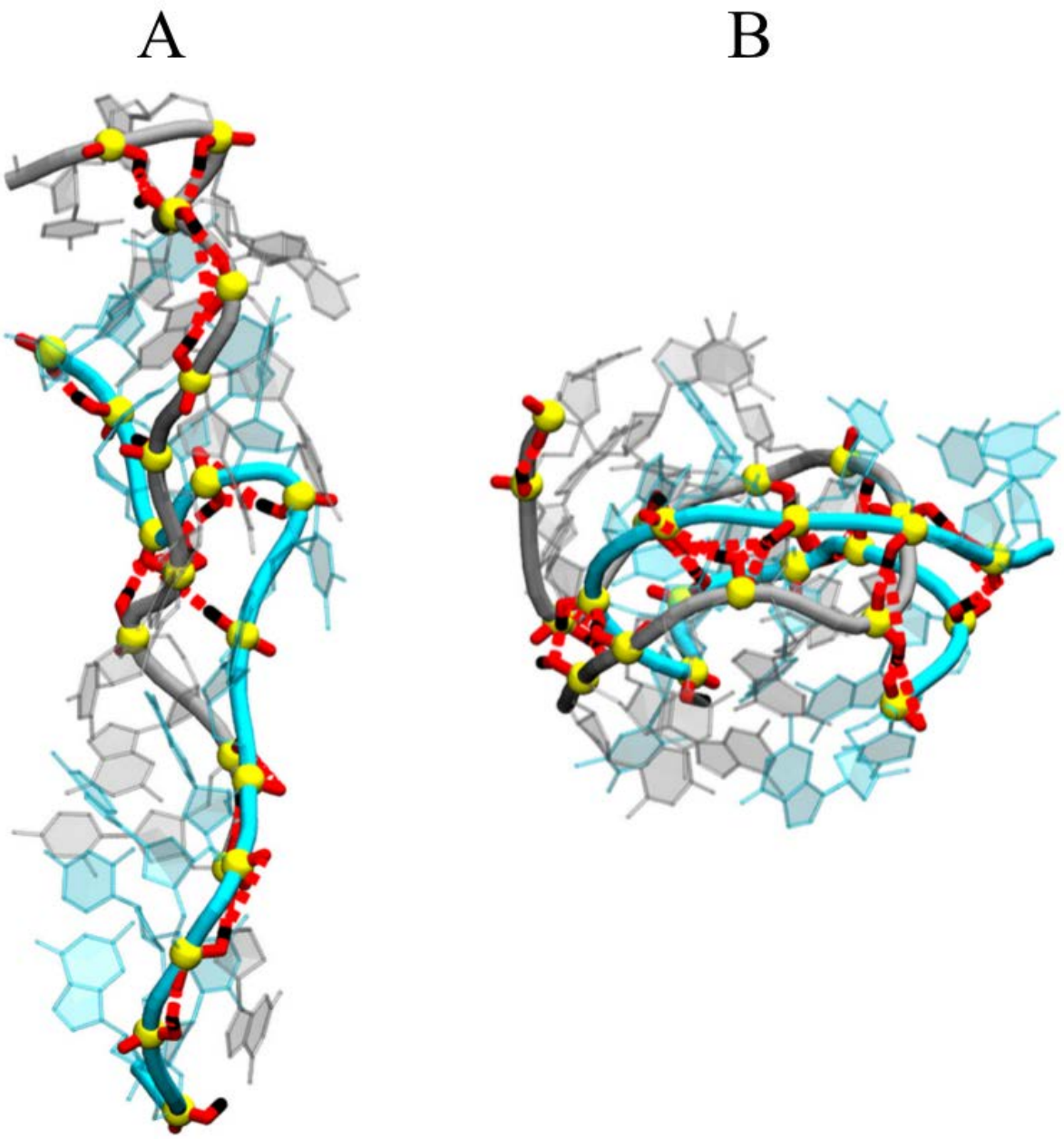

Figure 3.8: Final molecular structures from the gas phase (unbiased) molecular dynamic (MD) of B-DNA (A) and the zipped B-DNA (B). Both molecules have 5 negative charges. The dashed red lines indicate the H-bonds. The DNA sequences are $(dCGCGAATTCGCG)_2$ for both. Reprinted from Porrini et al., ACS Cent. Sci. 2017, 3 (5), 454–461 (Open access).

Since the full width at half maximum (FWHM) of the peak in the spectrum in Figure 3.7 is 96 $Å^2$, the resolution of this measurement is $\frac{\Omega}{\Delta\Omega} \approx 10$. However, the ideal resolution of this ion mobility spectrometer should reach 200, according to the information given by the engineer of the Bruker Daltonics Company. We have two explanations for the low resolution observed. One is that only one family of conformers exists, sharing the same global secondary structure, but the parameters (mainly the ramp time to determine the rate at which the electrical field in the

second part of the TIMS tunnel is reduced) of the apparatus are not optimized for ultimate resolution. Another explanation may be that there are different slightly different sub-structures existing, and the resolution is not sufficient to distinguish the peaks corresponding to these different structures. In any case, we can claim that the structure of $[d(CGCGGGCCCGCG)_2\text{-}5H]^{5-}$ is most probably a zipped helix, indicating that the dimer pre-exists in solution, and was not formed in the gas phase, like for collagen peptide assemblies[103].

Apart from the $[d(CGCGGGCCCGCG)_2\text{-}5H]^{5-}$ oligonucleotide dimer, we have also obtained the mobilograms of some other ions in Figure 3.3 by selecting their corresponding highest isotope peak in the MS. Here, the experimental collision cross sections of $[d(CGCGGGCCCGCG)_2\text{-}5H]^{5-}$, $[d(CGCGGGCCCGCG)_2\text{-}4H]^{4-}$ and $[dCGCGGGCCCGCG\text{-}4H]^{4-}$ are obtained from the corresponding mobilograms, as shown in Figure 3.9.

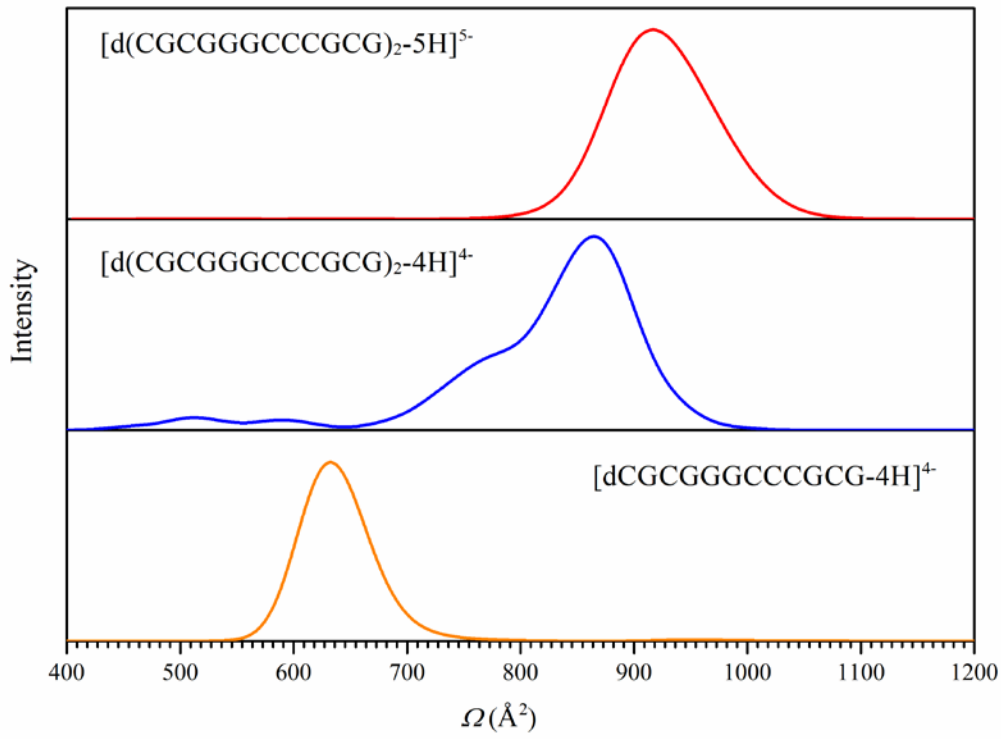

Figure 3.9: Experimental collision cross sections of $[d(CGCGGGCCCGCG)_2\text{-}5H]^{5-}$, $[d(CGCGGGCCCGCG)_2\text{-}4H]^{4-}$ and $[dCGCGGGCCCGCG\text{-}4H]^{4-}$.

Each of these three curves has a highest peak, which indicates that the corresponding ions all have at least one structure. Nevertheless, the curve of $[d(CGCGGGCCCGCG)_2\text{-}4H]^{4-}$ also has some smaller intensity peaks at lower cross-sections. These smaller peaks might be assigned to other structures for $[d(CGCGGGCCCGCG)_2\text{-}4H]^{4-}$, or to larger oligomers of higher charge state having the same *m/z*. In any case, these additional peaks are not very intensive, which is

consistent with the mass spectrum in Figure 3.3 (e). Furthermore, from the peak positions, we can see that the $[d(CGCGGGCCCGCG)_2\text{-}5H]^{5-}$ has the largest CCS and the $[dCGCGGGCCCGCG\text{-}4H]^{4-}$ has the smallest CCS. Obviously, the CCS of two dimers are similar and larger than the one of the monomer. More interestingly, the CCS of dimer increases with the charge state. It may be due to unfolding of the DNA structure. According to the article of Garabedian *et al.*[104], when they record the mass spectra and mobility profiles in nitrogen for i-motif DNA as a function of the solution pH (4.0 - 9.0) in both positive and negative ESI modes, they find that the increase of CCS with the charge state is an expected trend and does not necessarily reflect major conformational changes for low charge states (*e.g.*, +3 to +5 and -3 to -5). It may simply reflect less "compact" conformations due to the charge state and the internal base pairing stacking within the i-motif DNA. The increase of the CCS values of the dimers with the increase of the charge state can also be attributed to the stronger interaction between the charge of the molecular ion and the induced dipole of the gas molecule. The reason is that we used nitrogen gas instead of helium gas as the collision gas, N_2 being much more polarizable than He. As reported by Bush *et al.*,[102] when the charge state of cytochrome c increases from 6 to 7, its CCS on N_2 increases by 7%, whereas the its CCS on He only increases by 3%, while the structure stays the same (native). They also report a similar phenomenon for b-lactoglobulin in the same article. When the charge state of b-lactoglobulin increases from 7 to 8, its CCS on N_2 increases by 4% while its CCS on He increases by only 2%.

To quantitatively analyze these collision cross sections in Figure 3.9, we calculate them using the commercial software DataAnalysisViewer (Bruker Daltonics). The resulting data are given in Table 2. We got five different collision cross sections for the same ion because the commercial software gives different collision cross sections when we select different isotope peaks of the same ion. In principle, they should be the same since the only difference of the isotopes is the neutron number, which should not have a big influence on the collision cross section. The difference mainly comes from the uncertainty of the measurement. The uncertainty of these five collision cross sections is also given in Table 2. The uncertainty is equal to the standard deviation of these five collision cross sections. The CCS of the dimer 5- is 6% higher than that of the dimer 4-, which is consistent with the results of Bush *et al.* for protein cations discussed in the previous paragraph. Thus, the structure of the dimer 4- is most probably mainly a zipped helix like for the dimer 5-. For monomers, increasing the charge state from 3- to 4- leads to a 9% higher CCS, which is thus mostly due to charge-dipole interactions and not structural change.

Table 2: Collision cross-sections (CCS) of negative ions from the dCGCGGGCCCGCG oligonucleotide obtained from ion-mobility spectra.

ion	CCS isotope 1 (Å^2)	CCS isotope 2 (Å^2)	CCS isotope 3 (Å^2)	CCS isotope 4 (Å^2)	CCS isotope 5 (Å^2)	Average of the five CCS (Å^2)	Uncertainty of CCS (Å^2)
$[d(CGCGGGCCCGCG)_2\text{-}5H]^{5-}$	910.4	909.2	910.5	909.7	910.8	910.12	0.7
$[d(CGCGGGCCCGCG)_2\text{-}4H]^{4-}$	872.4	857.4	856.7	858.1	862.3	861.38	6.5
$[dCGCGGGCCCGCG\text{-}4H]^{4-}$	629.4	628.8	628.8	629	628.8	628.96	0.3
$[dCGCGGGCCCGCG\text{-}3H]^{3-}$	575.8	575.5	575.4	575.1	574.4	575.24	0.5

In this table, if we compare the collision cross section of $[(dCGCGGGCCCGCG)_2\text{-}4H]^{4-}$ with the one of $[dCGCGGGCCCGCG\text{-}4H]^{4-}$, we can see that the former one is far less than twice of the latter, though they have the same charge state. It makes sense because the monomers are not rigid and they are tightly bound to each other to form the dimer.

However, we cannot convert all these mobilities in the mobilograms to the CCS. This is because the CCS strongly depends on the charge of the ion, according to Equation (4). In mass spectra, it is possible to have the same m/z for different ions with different masses and charges. Especially in our case, since we are using an oligonucleotide that can self-assemble itself into a DNA dimer, it is not surprising that we have a peak that can be assigned to both a monomer and a dimer. As we mentioned earlier in this chapter, all the peaks of $[dCGCGGGCCCGCG\text{-}3H]^{3-}$ overlap with some of $[d(CGCGGGCCCGCG)_2\text{-}6H]^{6-}$ (see Figure 3.4). It is therefore impossible to obtain the mobilogram of a pure $[dCGCGGGCCCGCG\text{-}3H]^{3-}$: for instance, if we select its highest isotope peak (*m/z*=1214.8670 in Figure 3.3 c), as the result is presented in Figure 3.10. The mobilogram is composed of three peaks, and the mass spectrum of each peak can be acquired by the commercial software. It is clear that only for peak 3 (corresponding to the highest CCS) we can see the isotopic pattern of an almost pure $[dCGCGGGCCCGCG\text{-}3H]^{3-}$. In the first and second peaks (corresponding to lower CCS), the amount of double strands ($[d(CGCGGGCCCGCG)_2\text{-}6H]^{6-}$) increases.

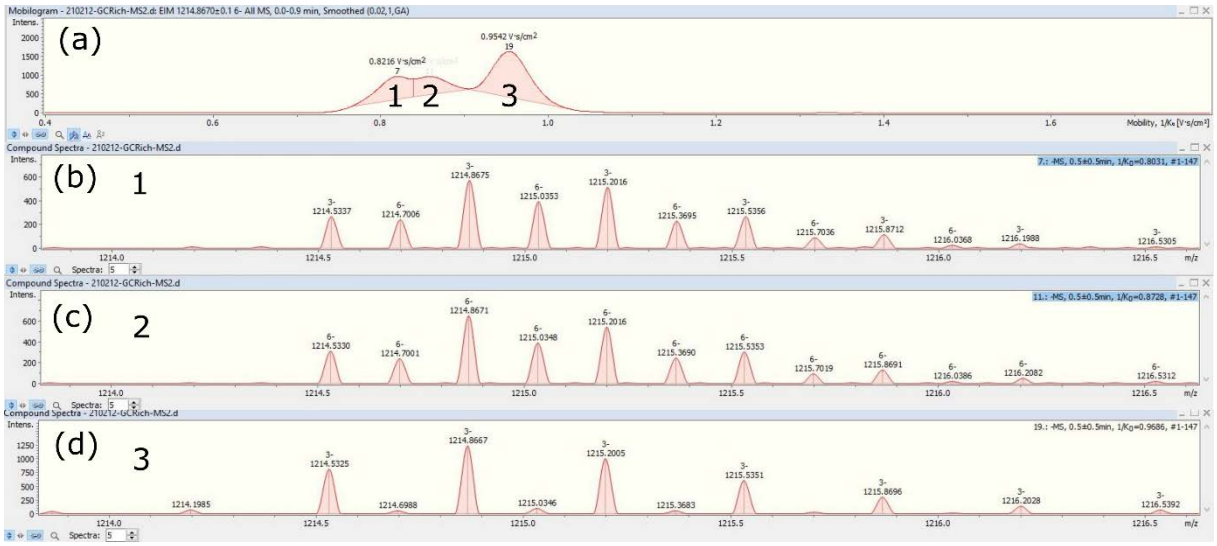

Figure 3.10: (a) The mobilogram of [dCGCGGGCCCGCG-3H]$^{3-}$. (b-d):The different mass spectra of of [dCGCGGGCCCGCG-3H]$^{3-}$ with different collisional cross sections.

On the other hand, not all the peaks of [d(CGCGGGCCCGCG)$_2$-6H]$^{6-}$ overlap with those of [dCGCGGGCCCGCG-3H]$^{3-}$, which means that we may get a "clean" mobilogram of [d(CGCGGGCCCGCG)$_2$-6H]$^{6-}$ when we select one of the isotope peaks that corresponds only to [d(CGCGGGCCCGCG)$_2$-6H]$^{6-}$ (*m/z* = 1214.7005, in Figure 3.3 c). The resulting mobilogram does not have a single peak (see Figure 3.11 a): it means that several structures are present.

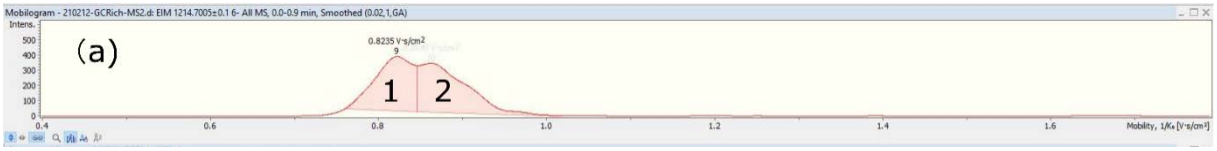

Figure 3.11: (a) The mobilogram of [d(CGCGGGCCCGCG)$_2$-6H]$^{6-}$ obtained by selecting the peak at m/z = 1214.7005 in the MS.

When we calculate the CCS of [d(CGCGGGCCCGCG)$_2$-6H]$^{6-}$ according to the highest-intensity peak in Figure 3.11 (a) using the commercial software, the cross section of this dimer is 991 Å^2, about 9% higher than that of the 5- dimer. This increase cannot be accounted for only by the charge-dipole interaction, thus the structure of the 6- dimer must be more unfolded than the zipped helix. Interestingly, 991 Å^2 is close to the cross section of the canonical B-helix on nitrogen (1080 Å^2), as we discussed above. Peak 2 should be even closer in CCS. It is an evidence for the partial survival of this canonical B-helix conformation for this charge state. Since the structure of the same DNA sequence becomes less compact and closer to the canonical B-helix when the charge state increases, it also indicates that the [d(CGCGGGCCCGCG)$_2$-7H]$^{7-}$ double strand that we irradiated with carbon ions (see the results in Chapter 5) may have a canonical B-helix structure in the gas phase.

3.4 Conclusions

In summary, we have identified many different DNA ions in the gas phase from the solution of the dCGCGGGCCCGCG oligonucleotide. We have successfully obtained and preserved the DNA dimer in the gas phase using an ESI source and ion traps, which is a good guide for our future studies on the irradiation of DNA dimers. Among the different dimers, we found that the dimers with an unambiguous *m/z* (with *z* = 5 or 7 for instance) are the ideal targets for studying dimers, because they cannot be mixed with the monomers in the MS. We therefore chose the $[d(CGCGGGCCCGCG)_2\text{-}5H]^{5-}$ as the target dimer. We have studied the CID of this ion and found the dissociation pattern due to collision induced dissociation, which can be a reference for the fragmentation pattern due to irradiation.

In addition, we have analyzed the structure of different DNA ions with the ion mobility spectrometry. The collision cross section of the dimer with 5 negative charges is more compact compared to the canonical B-helix, possibly a zipped B-helix, due to novel phosphate-phosphate interactions. Besides, we found that the CCS of dCGCGGGCCCGCG dimers increases with the charge state, due to the stronger gas-molecular ion (charge-induced dipole) interaction when going from 4- to 5- charge states, and but also due to structural unfolding for the 6-. We also found that the collision cross section of the DNA dimer is much less than twice of the monomer, because the monomers are not rigid and they are tightly bound together to form the dimer.

4 Irradiation of isolated DNA oligonucleotides by X-ray photons

4.1 Introduction

The initial phases of ionizing radiation's impact on biological systems involve primary processes of radiation-induced excitation and/or ionization. These are succeeded by a sequence of events involving the transfer of charge, energy, and matter. To study these processes in detail, it is better to localize the initial excitation/ionization event. However, achieving this level of precision is an experimental challenge, especially at the molecular scale. In the field of molecular collision studies involving projectile ions or electrons, achieving site selectivity means narrowing down the range of impact parameters with precision. This precision allows the selective ionization or excitation of a single atom, or at least a particular chemical group within the molecule. However, this is not possible from a technical point of view. Thus, considerable focus has been directed towards photoabsorption in the UV, VUV, and X-ray ranges. In these ranges, it becomes feasible to finely adjust photon energy, allowing for the precise targeting of individual atoms or specific groups within a molecular system. Gas-phase investigations are exceptionally well-suited for the exploration of VUV and soft X-ray-induced processes in molecules. Because they provide an opportunity to delve into the authentic molecular reactions, free from the influences of a surrounding medium. Focusing on molecular ions rather than neutrals opens up the possibility of manipulating them with electric and magnetic fields. It also allows molecular analysis by mass spectrometry. Specifically, this approach enables the precise selection of target molecular ions for irradiation and the determination of the mass-to-charge (*m/z*) ratio of the resulting product ions. This advantage is invaluable in revealing processes such as ionization, fragmentation and electron, proton or hydrogen transfer.

In the context of site-selective ejection of electrons from molecular systems in the gas phase, UV lasers have been shown to be effective in triggering electron photodetachment from deprotonated groups of oligonucleotides,[105] peptides and proteins,[106] as well as lipids and polysaccharides.[107] Notably, it has been discovered that inducing backbone fragmentation of radicals generated by electron detachment from polymer molecules is of significant value for their sequencing.[108] VUV photons have been used for the valence ionization of biomolecular ions.[64,66,109,110] However, pinpointing the exact location of the ionization event can be challenging, mainly because valence electrons tend to exhibit greater delocalization compared to core electrons. To overcome this challenge, derivatized peptides containing aromatic tags

with lower ionization energies than any other group within the peptide can be employed. For example, one such tag designed by Edirisinghe *et al.* allows ionization to occur after the absorption of a single 7.9 eV photon from a fluorine laser.[111] The resulting radical cation has been observed to achieve stabilization through charge delocalization across the molecular backbone. To improve precision, it is a straightforward approach to focus on targeting core electrons within atomic orbitals. Using gas-phase soft X-ray photoelectron spectroscopy coupled to synchrotron radiation, Ueda has studied the binding energies of the 1s electrons of light atoms. He has investigated carbon and oxygen atoms in small molecules like CO_2 or H_2O, shedding light on the Auger electron emission processes resulting from the formation of a 1s vacancy.[112] More recently, this method has been extended to study neutral amino acids,[113,114] small peptides,[115] and nucleobases.[116,117] This expanded application has provided evidence that the binding energy of 1s electrons exhibits relatively low sensitivity to the presence of neighboring atoms. However, for more biologically significant systems such as peptides, proteins and DNA oligonucleotides, a soft approach is required to bring them into the gas phase. Techniques such as electrospray ionization (ESI) or matrix-assisted laser-induced desorption ionization are used. Once in the gas phase, these molecules are accumulated in ion traps to achieve a sufficient molecular density to provide a satisfactory signal-to-noise ratio for the detection of product ions formed during ionization and/or fragmentation processes resulting from photoabsorption. Hence, since 2010, researchers have been exploring these systems using a combination of near-edge X-ray absorption fine structure action spectroscopy and mass spectrometry. In the process, they've revealed that the excitation or ejection of 1s electrons from carbon, nitrogen, or oxygen atoms results in Auger electron emission.[64,118,119] Nevertheless, these atoms are scattered throughout these molecules, making it difficult to link a product ion to a specific absorption site. This is why Schwob and his colleagues decided to investigate the methionine enkephalin peptide by examining its photoabsorption at the sulfur L-edge.[120] This choice was made because this particular molecule contains just one sulfur atom. They have shown that specific photoabsorption causes fragmentation to occur close to the excited site. Recently, Wang et al. have performed specific photoabsorption experiments at the K-edge of the fluorine atom in the fluorouracil nucleobase of a trinucleotide. Surprisingly, these experiments predominantly yielded product ions originating from the other two nucleobases.[65] A similar counter-intuitive result has been documented when nitrogen atoms within the same oligonucleotide are ionized.[121] However, the exact mechanism responsible for this phenomenon remains poorly understood. To selectively target the DNA backbone, one can tune the photon energy to target the phosphorus core electrons in the 1s orbitals, typically around 2150 eV.

Earlier investigations have documented the precise fragmentation of a phosphorus-oxygen (P-O) bond in a dinucleotide in the solid phase.[122] This method has also been found to enhance the efficiency of inducing double-strand breaks in DNA plasmids,[123] and it can even lead to chromosome aberrations in cellular structures.[124]

In this study, we investigate the photoabsorption of an isolated oligonucleotide at the phosphorus K-edge. We have studied the product anions and cations resulting from single photon absorption via mass spectrometry. Our aim is to illustrate that the selective absorption at phosphorus atoms induces a transfer of charge, energy, and hydrogen from the DNA backbone to the nucleobases.

This oligonucleotide used here (dCGCGGGCCCGCG) contains 11 phosphorus atoms and has 50% guanine and 50% cytosine in terms of nucleobase content. Since guanine has the lowest ionization energy of all nucleobases, it is known to be a hole sink in nucleosides as well as oligonucleotides in the gas phase.[66,125] If the initial ionization event occurs at the backbone, the probability for the hole to be transferred to one of the bases should be high. This oligonucleotide is thus a good candidate for backbone-base charge transfer.

Studying X-ray absorption around the phosphorus K-edge is challenging, because the absorption cross-section at this photon energy (around 2150 eV) is one order of magnitude lower than that of carbon around 300 eV. In detail, the absorption cross-section at phosphorus K-edge is 2.6×10^3 cm^2/g (1.34×10^5 barns/atom), while the absorption cross-section at carbon K-edge is 4.6×10^4 cm^2/g (9.18×10^5 barns/atom).[126] What's more, oligonucleotides contain many more carbon than phosphorus atoms, for instance 114 against 11 in dCGCGGGCCCGCG. In order to compensate for the low absorption probability, X-ray exposure times had to be increased by almost 5 times as compared to our previous study at C K-edges.[67] In this study, at C K-edges we set the exposure time as 1000 ms against 4750 ms at P K-edge.

4.2 Experimental details

4.2.1 Experimental setup and materials

X-ray photoabsorption experiments were carried out to study photofragmentation and electron photodetachment of isolated DNA. In these experiments, a home-built tandem mass spectrometer developed by the group of Thomas Schalthölter (University of Groningen, Netherlands) was used. It has already been described in detail in these articles[127,128] as well as in Section 2.1 of this thesis. It was interfaced with the variable polarization XUV beamline P04[79] at the PETRA III synchrotron light source facility (Hamburg, Germany). The photon

energy range of this beamline was 250-3000 eV. The gratings used in our experiments were G1200 6nm near P K-edge (2150 eV) and G400 15 nm near C K-edge (300 eV). The exit slits were 1.5 mm near P K-edge and 0.5 mm near C K-edge, leading to energy resolutions of 8 eV and 0.5 eV, respectively. Mass spectra were recorded near carbon K-edge and phosphorus K-edge energies. To record these mass spectra, a powder of the dCGCGGGCCCGCG oligonucleotide of up to 85% purity (Reverse-Phase HPLC purified, Eurogentec, Seraing, Belgium) was dissolved without further purification in a mixed solvent of 75% HPLC methanol, 25% deionized water and 5% ammonium hydroxide, at a final concentration of 100 µM. To avoid sodium adducts, this oligonucleotide was desalted by a gel filtration medium called Sephadex G25, which is commonly used in affinity chromatography, protein chromatography and gel filtration chromatography. The desalting process was done by the Eurogentec company before shipping. The oligonucleotide solution was then introduced in a syringe and pushed towards the needle of an in-house-built electrospray ionization (ESI) source under atmospheric conditions, using a syringe pump with a flow rate of about 0.15 mL/h. All anions produced by the ESI source in the negative mode were then guided into a first vacuum chamber where a radio frequency (RF) ion funnel locates in. After phase space compression in the funnel, the ion beam had further phase space compression in an octopole RF ion guide. Subsequently, the deprotonated oligonucleotide ion of a given charge state was selected by mass over charge (*m/z*) ratio in a quadrupole mass filter. These selected ions are called precursors and were accumulated in a three-dimensional RF ion trap for a controlled time (typically 50 ms) to get sufficient target density. In the trap, a helium buffer gas pulse was used to cool down the precursors to room temperature by collisions. After accumulation, the photon beam went through the center of the trap to interact with the precursors. The interaction time was adjusted between 1000 and 4750 ms to ensure that less than 10% of the precursors were depleted. In this case, single interaction processes dominated. Because the multiple photon absorption is a sequential process at these photon fluxes, typically 10^{12} s^{-1} – 10^{13} s^{-1}, the absorption events are independent. Thus, if we set the probability for absorbing one photon as p, then the probability for absorbing two photons will be p^2. If we neglect the absorption of more than two photons, we can obtain $p + p^2 < 0.1$ and therefore $p < 0.09$ and $p^2 < 0.0081$. It means less than 9% of the product ions come from the absorption of one photon and less than 0.81% from two-photon absorption, in another word, more than 90% of the product ions come from the absorption of one single photon. After interaction, either the negatively charged products and precursors left or the positively charged products were extracted from the trap by a pulsed electric field, depending on the polarity of the bias voltages on the RF trap end caps. Then, the ions entered

into a reflectron time-of-flight (Re-TOF) mass spectrometer where they were accelerated by a uniform electric field, then reflected by an electrostatic mirror, and finally detected by a microchannel plate (MCP) detector. The MCP had a front plate biased at -2.5 kV and an anode plate at ground potential for detecting cations, but these values were +2.5 and +4.5 kV for anions.

The signal from the anode was sent to an oscilloscope (Teledyne Lecroy, waveRunner 625Zi), triggered on the extraction pulse rising edge, to record the analog trace as a TOF spectrum. For technical reasons, the oscilloscope cannot deal with a too wide range of signals, so the TOF of the ions was restricted to 200 µs. Then, this TOF spectrum was sent to a computer program that accumulates a controlled number of spectra (200-600 scans according to the signal intensity) to get the final averaged TOF spectrum. The experiment was running in cycles of two TOF spectra. The first one was recorded when the ionic trap content was not irradiated by the photon beam (labeled as ONLY ESI) and the second one was recorded when the ionic trap content was irradiated by the photon beam (labeled as ESI + BEAM). The entire 2-step cycle was repeated typically for several hundred times to get sufficient statistics and satisfactory signal to noise ratio. The final mass spectrum was the result of the subtraction of the ONLY ESI spectrum from the ESI + BEAM spectrum, which reflects the net effect of the irradiation beam on the trapped ions.

4.2.2 Energy calibration

To calibrate the beamline photon energy from 1700 eV to 2500 eV, we used an electron spectrometer developed at DESY for beamline diagnostic.[129] The main principle is the following: the time-of-flight (TOF) of electrons coming from photoionization of a gas is recorded by 16 spectrometers arranged in the geometry shown in Figure 4.1. The plane of these spectrometers is perpendicular to the photon beam being examined. The gas is injected via a thin capillary to the interaction region near the center of the 16 electron time-of-flight spectrometers. The pressures in the operating chamber are typically in the range of 10^{-6} mbar. In the interaction region, the effective target pressure is about 1-2 orders of magnitude higher than the operating pressure and a base pressure about 3 orders of magnitude lower than the operating pressure is usually achieved. Each spectrometer has its own entrance apertures and is well shielded from the others, thus, different retarding potentials for the electrostatic mirrors can be applied to the four isolated flight tube sections of each electron analyzer.

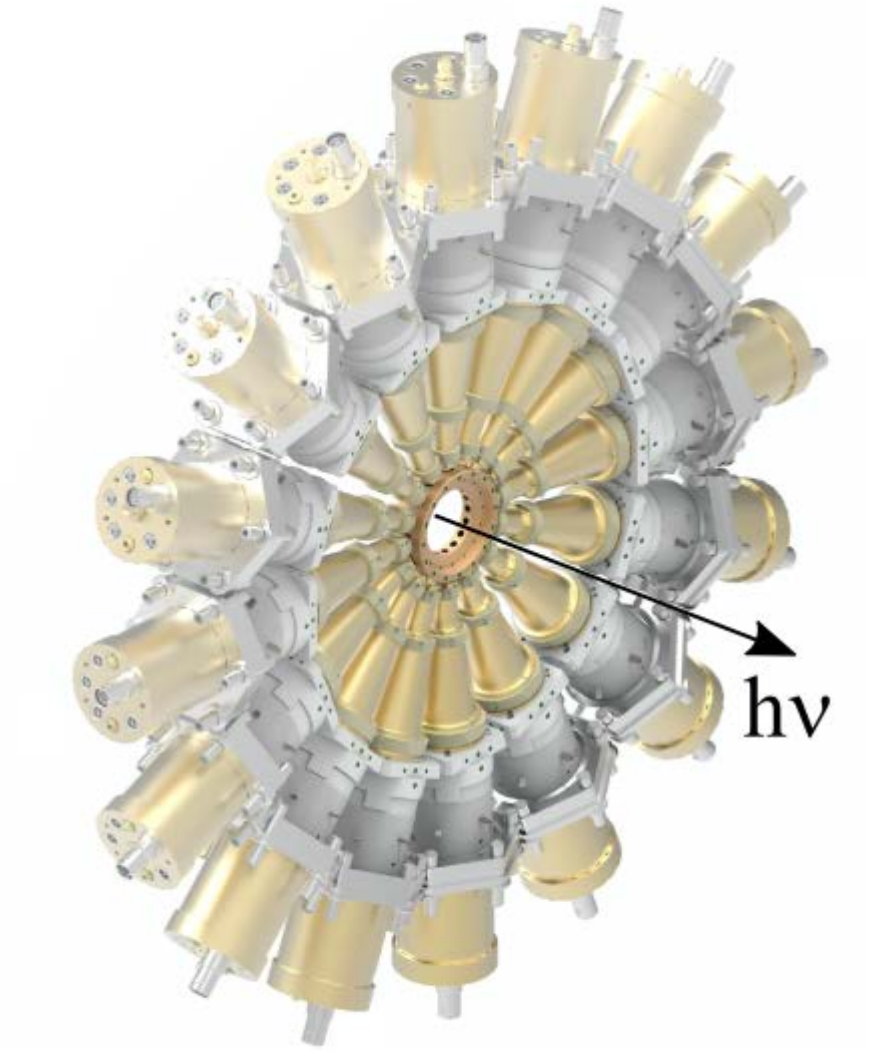

Figure 4.1: Schematic drawing of the 16 electron time-of-flight spectrometers. Reprinted from J. Buck, AIP Conference Proceedings 2054, 060057 (2019), with the permission of AIP Publishing.

The electrons are detected by multi-channel-plates (MCP) fixed on modified hex-cut CF40-feedthrough-flanges. All detectors contain 3 MCPs with a Z-stack configuration. Every MCP detector voltage can be optimized for the best detector response (usually less than 3 kV across all three MCPs). In this electron spectrometer, the FWHM spike width is below 1 ns with amplitudes in an order of 10 mV in the capacitively decoupled and pre-amplified (> x15) signal output. The data acquisition electronics (DAQ) include constant fraction discriminators and a time-to-digital converter (120 ps bins). By plotting the flight time of each electron detected, 16 electron time-of-flight spectra are obtained. The high flux of beamline P04 allows typical acquisition times to be reduced to a few seconds to obtain meaningful statistics.

Here, we used two gases, Kr and SF_6. In Figure 4.2, we show measurements of the signal due to electrons coming from photoexcitation of SF_6 around the sulfur K-edge followed by Auger decay and emission of an electron of 2486 eV[130], as well as from photoionization at threshold of the $2p_{1/2}$ orbital of krypton (1729 eV[131]). From these measurements, we extracted the two corresponding values of the beamline photon energy, and plotted the real photon energy as a function of beamline photon energy (see Figure 4.2). We assumed a linear relationship between the real and beamline values of photon energy in this range, and thus fitted a linear function to the two data points in Figure 4.2. From this linear function, we can know that the real photon energy is about 3 eV higher than the beamline value in this energy range.

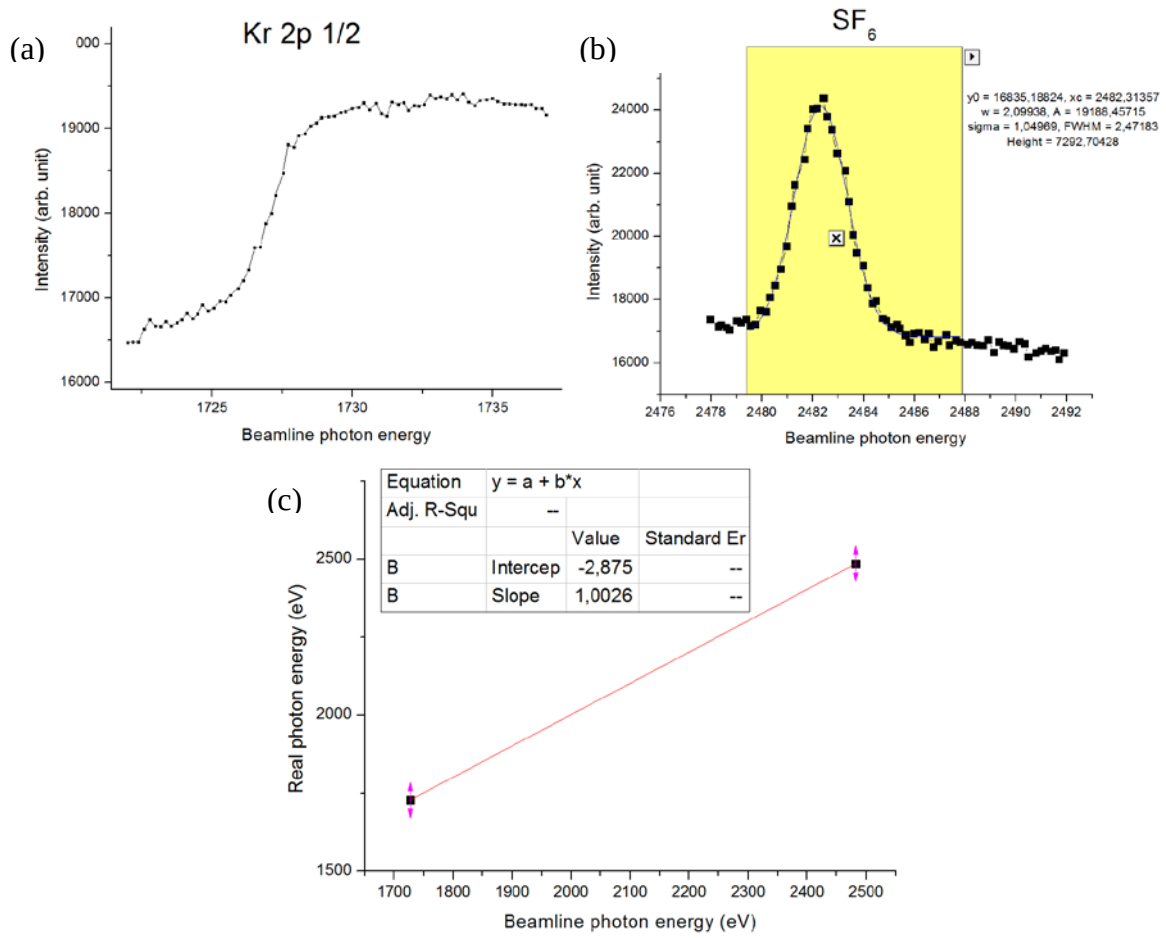

Figure 4.2: (a) Intensity of the signal from electrons coming from photoionization of krypton at the threshold of the $2p_{1/2}$ orbital as a function of photon energy (b) Intensity of the signal from electrons coming from photoionization of SF_6 around the sulfur K-edge as a function of photon energy (c) Linear fit of the real value of photon energy and the beamline value of photon energy.

4.3 Results and Discussion

4.3.1 Specific photoabsorption at the phosphorus atoms

First of all, we need to prove that in our experiment, around the phosphorus K-edge energy (2150 eV), the photon is indeed absorbed specifically by the backbone phosphorus atoms of the isolated deprotonated DNA oligonucleotide of sequence dCGCGGGCCCGCG.

Although the phosphorus K-edge energy of phosphorus atom is reported as 2145.5 eV in condensed phase[126], it could vary with the atomic environment[132]. This change is sometimes negligible, for example, the phosphorus binding energies shift is less than 3 eV with the chemical changes (from the covalent orthophosphates to the alkaline and earth-alkaline phosphates and the ionic transition-metal phosphates). What's more, an early previous work on isolated proteins has demonstrated that resonant features in K-shell X-ray photoabsorption spectra are energetically very similar to the respective data from condensed-phase experiments.[118] For example, the lowest-energy C 1s $\rightarrow \pi^*$ transitions is located at about 285.5 eV in the gas phase while the same feature has been reported at 285.13 – 285.15 eV for the protein solid films. Therefore, even though there is no report about the specific photoabsorption at the phosphorus atoms in DNA molecules in the gas phase, we can still refer to the studies in the condensed phase. Thanks to the X-ray absorption studies on DNA in aqueous solution by Czapla-Masztafia *et al.*[133], we know that the 2145 – 2185 eV energy range features a sharp resonance around 2150 eV, due to excitation of a phosphorus 1s electron into an unoccupied molecular orbital with overlapping P sp^3 and O 2p atomic orbitals (*cf.* Figure 4.3).

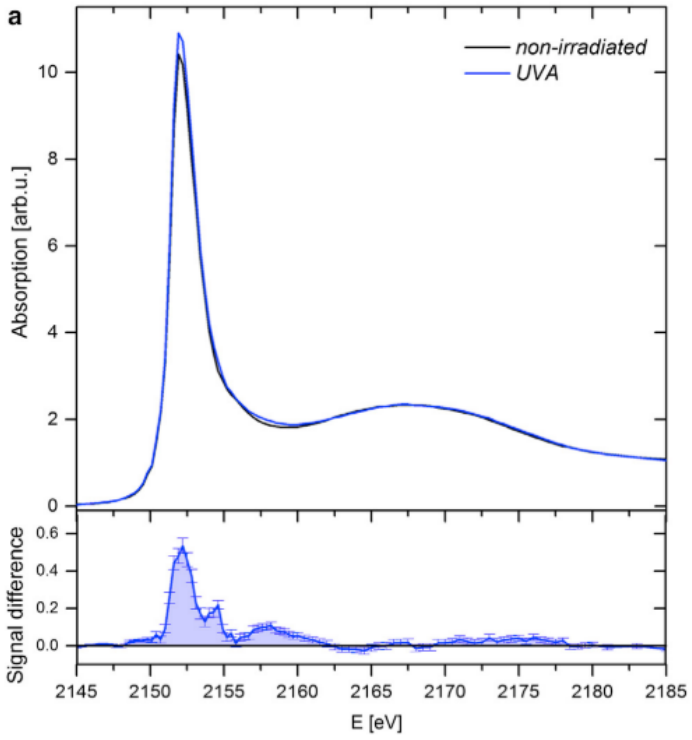

Figure 4.3: Top: phosphorus K-edge X-ray absorption spectra of intact and UVA-irradiated aqueous DNA samples. Bottom: difference between the two above spectra. Reprinted from Joanna Czapla-Masztafia, Biophysical Journal 110, 1304–1311, March 29, 2016 Copyright (2016), with permission from Elsevier.

In addition, there is a much broader peak around 2165 – 2170 eV, which has been assigned to photoelectron scattering on oxygen atoms of phosphate groups. Thus, in our measurements, photoabsorption mass spectra for anionic and for cationic products of the dCGCGGGCCCGCG oligonucleotide were recorded for X-ray photon energies in this range, namely 2143 eV (below K-edge), 2151 (on the resonance), 2163 and 2178 eV. For both 4- and 5- charge states of the oligonucleotide (*m/z* 911 and 728, respectively), the most abundant negative ion created by single-photon absorption is due to non-dissociative single electron detachment (NDSED), as shown in the mass spectra of Figure 4.4: indeed, mostly one peak is observed at *m/z* 1215 for $[dCGCGGGCCCGCG\text{-}4H]^{4-}$ or at *m/z* 911 for $[dCGCGGGCCCGCG\text{-}5H]^{5-}$. This is not surprising to observe electron detachment, given the very low electron detachment energy compared to these photon energies: indeed, the binding energy of outer valence electrons drops with the charge state of the oligonucleotide procursor, for instance from 3.2 eV for the 2- charge state of deprotonated dGGGTTT to -0.2 eV for the 5-.[105] Thus, the probability to observe electron detachment increases with the charge. In the spectra of $[dCGCGGGCCCGCG\text{-}5H]^{5-}$, other peaks are also observed at lower *m/z*, but their intensity is lower, and the relative abundance of the corresponding ions is even lower because of the falling of MCP detection efficiency with ion velocity and thus *m/z*. In addition, we have also obtained the

photoabsorption mass spectra of anionic and for cationic products of the $[dCGCGGGCCCGCG\text{-}4H]^{4-}$ precursor around the carbon K-edge, namely 288 eV (on the resonance), 300 eV (above K-edge). We observed the most abundant negative ion due to NDSED at *m/z* 1215, and additional peaks at the same *m/z* (466 and 506) as those present at the P K-edge of $[dCGCGGGCCCGCG\text{-}5H]^{5-}$.

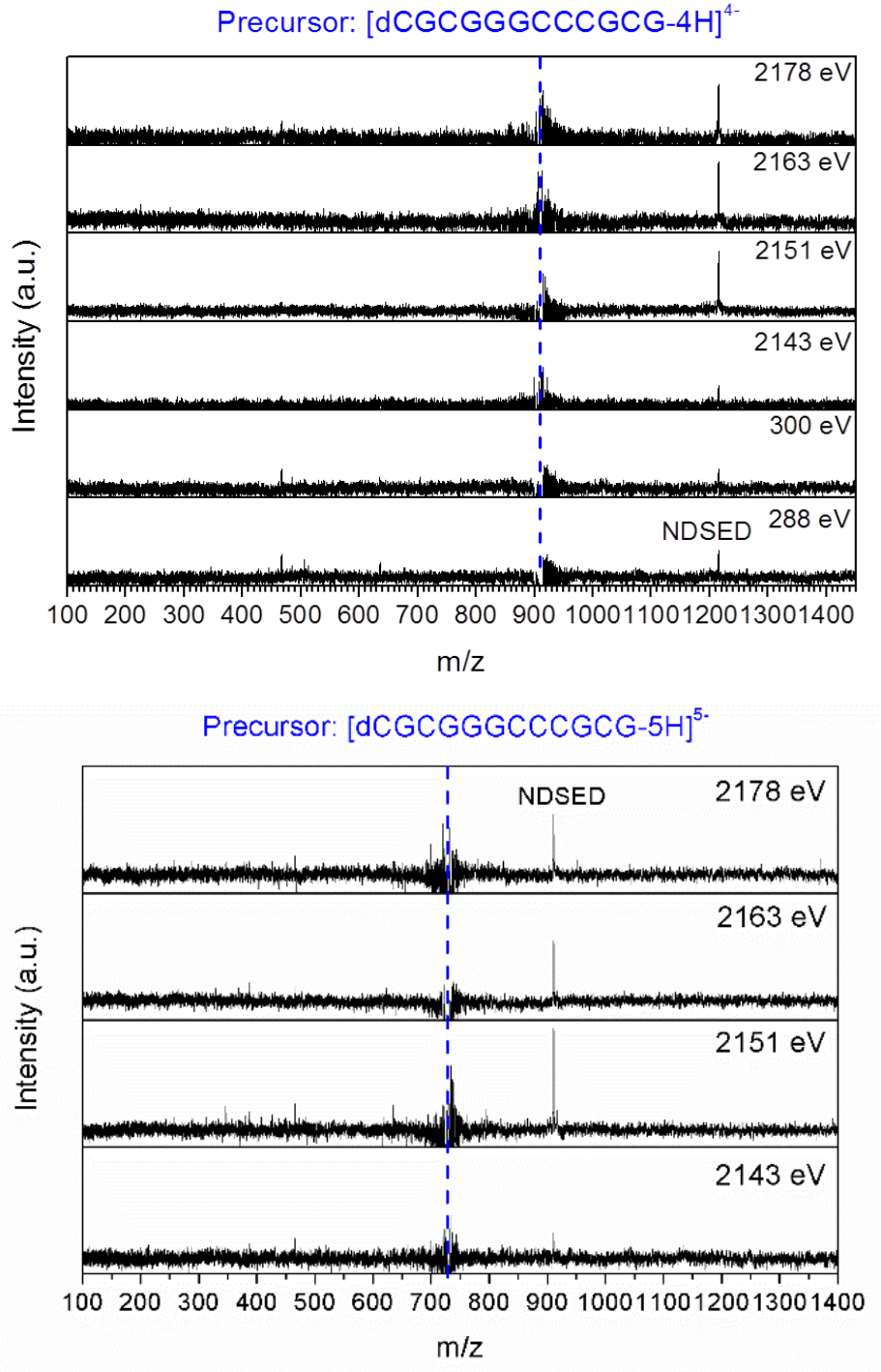

Figure 4.4: Mass spectra of the negative products of $[dCGCGGGCCCGCG\text{-}4H]^{4-}$ and $[dCGCGGGCCCGCG\text{-}5H]^{5-}$ after single photon absorption. NDSED stands for non-dissociative single electron detachment. The precursor ions' m/z are indicated by blue dashes.

In Figure 4.4, the peaks at *m/z* 466 and 506 are attributed to anions formed after scission of the DNA backbone. The possible structure and bond cleavage positions of the resulting internal fragments are given in Scheme 1: the one at *m/z* 466 containing cytosine is named as iC^-, and the one at *m/z* 506 containing guanine is named as iG^-. It is worth noting that these two fragments are the result of the indicated bond cleavage in the deprotonated DNA oligonucleotide, accompanied by the loss or transfer of one hydrogen from the fragment if the GC sequence is initially deprotonated. The same internal fragments after infrared multiphoton dissociation (IRMPD) of a 50-mer DNA containing 34% C, 20% A, 26% G and 20% T were also reported by Little *et al.*[134], but at *m/z* 467 and *m/z* 507, respectively. The one mass difference might be due to the presence of H transfer in the case of photoelectron detachment and thus formation of radicals. Compared to IRMPD, the loss of hydrogen highlights the fact that *m/z* 466 and *m/z* 506 are the results of an ionization process. Since the DNA oligonucleotide sequence used in our experiment only contains guanine and cytosine with the same ratio, we can assume that there is an equal chance to get an internal fragment with guanine and another internal fragment with cytosine, if the energetics are similar. This is not the case, since our results show that these two peaks at *m/z* 466 and 506 have different intensities in the mass spectra (Figure 4.4). Moreover, as already pointed out, the corresponding fragment ions have much lower yields as compared to NDSED, especially taking into account the lower detection efficiency at higher *m/z* ratios. This very low fragmentation yield is probably due to the large size of the system: it indicates that fragmentation occurs in the electronic ground state of the system, after intramolecular vibrational energy redistribution (IVR). We have observed such a phenomenon after VUV and X-ray photoabsorption of deprotonated oligonucleotides as well as protonated peptides and proteins.[66,67,128,135]

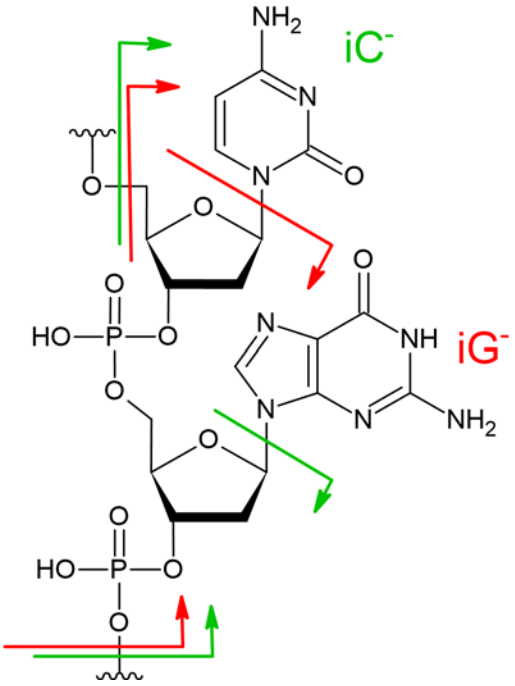

Scheme 1: Chemical structure of an internal CG sequence from the dCGCGGGCCCGCG oligonucleotide. The bonds that need to be cleaved to form the iC^- and iG^- fragments are spotted with green and red lines with arrows indicating on which side of the bond the negative charge is located.

In Figure 4.5, we show the relative yield of NDSED from $[dCGCGGGCCCGCG\text{-}4H]^{4-}$ after single-photon absorption. Around the carbon K-edge, this yield slightly decreases from 288 to 300 eV, consistent with the transition from single to multiple ionization observed in this range for protonated peptides and proteins.[118,136] Strikingly, from 2143 (below edge) to 2151 eV (on the resonance), the relative yield of NDSED increases by more than a factor of two, which is expected from the absorption of phosphorus atoms. Indeed, one P 1s electron is excited to an unoccupied P=O molecular orbital,[132] and Auger decay ejects one electron, resulting in single electron detachment. At 2163 eV, the yield of NDSED from dCGCGGGCCCGCG stays roughly constant, but it decreases at 2178 eV, consistent with the transition from excitation to ejection of 1s electrons, leading to more multiple- and thus less single-electron detachment. The same conclusions can be made for $[dCGCGGGCCCGCG\text{-}5H]^{5-}$ from the data appearing in Figure 4.5. However, the multiple-electron detachment product is not observed in our data set, indicating that the multiple-electron detachment products can be fragmented further and thus not detected. Since this behavior has also been observed at the C, N and O K-edges of proteins[118] as well as the C K-edge of deprotonated DNA oligonucleotides[67], it supports our present attribution of specific photoabsorption at the backbone phosphorus atoms of the studied oligonucleotide at photon energies of 2151, 2163 and 2178 eV. This is the first time that this process is reported for isolated DNA.

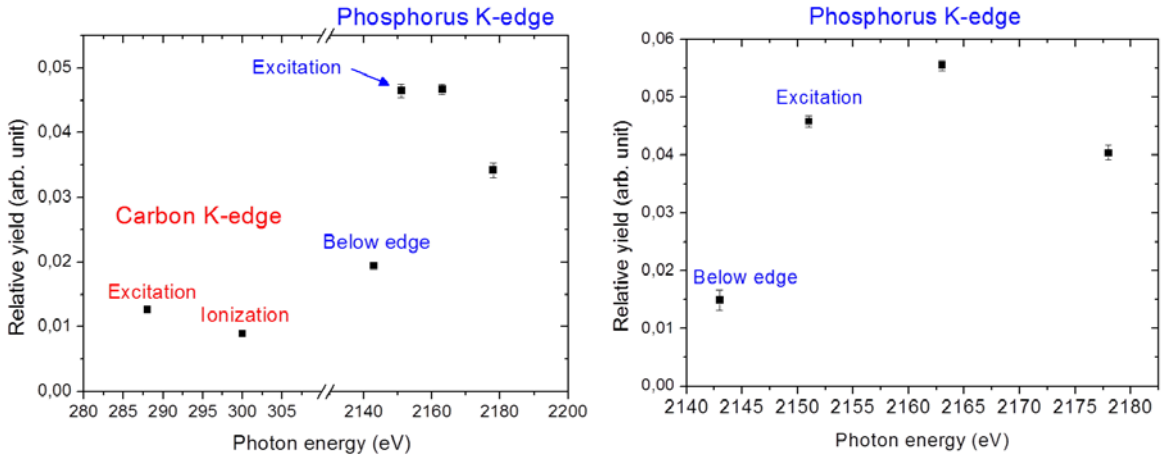

Figure 4.5: Relative yield of non-dissociative single electron detachment from [dCGCGGGCCCGCG-4H]$^{4-}$ (left) and [dCGCGGGCCCGCG-5H]$^{5-}$ (right) after single photon absorption, as a function of photon energy, obtained by calculating the area under the peak in the mass spectrum and normalizing by the area under the precursor depletion peak. Error bars represent the standard deviation of the average value from three independent calculations (n = 3). The energy regions corresponding to carbon and phosphorus K-edges are indicated in red and blue, respectively.

In Figure 4.6, we show the relative yield of internal fragments whose m/z equal to 466 and 506 (iC$^-$ and iG$^-$, respectively). Interestingly, both of them show a trend opposite to NDSED: it falls from below edge (2143 eV) to on the resonance (2151 eV), and increases at higher photon energy, especially for iG$^-$. This behavior indicates that NDSED and formation of these fragments are in competition, which can imply that fragmentation is subsequent to single electron detachment, but also putatively to multiple-electron detachment. Indeed, we will see in the next section that many electrons can be detached from the precursor as a result of X-ray photoabsorption.

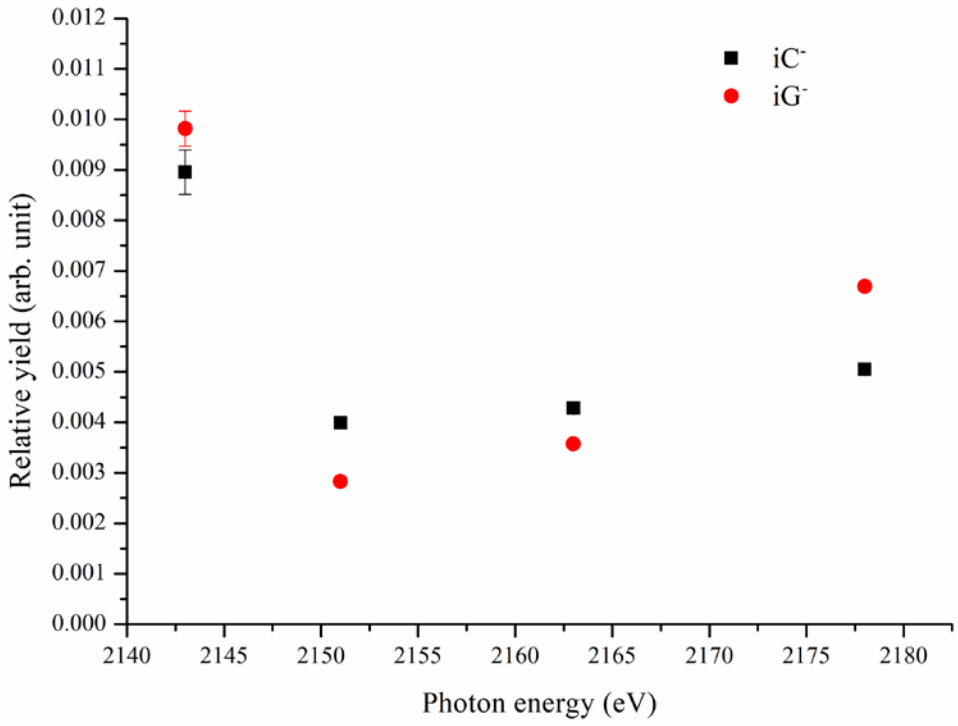

Figure 4.6: Relative yield of internal fragments from [dCGCGGGCCCGCG-5H]$^{5-}$ after single photon absorption, as a function of photon energy around the P K-edge, obtained by calculating the area under the peak in the mass spectrum and normalizing by the area under the precursor depletion peak. Error bars represent the standard deviation of the average value from three independent calculations (n = 3).

4.3.2 Charge, energy and hydrogen/proton transfer after photoionization

This section will show that charge and/or energy as well as H/H$^+$ are transferred from backbone to nucleobases within the dCGCGGGCCCGCG oligonucleotide after photoionization. In the previous section, we have seen that NDSED is the main process responsible for the formation of negative ions from [dCGCGGGCCCGCG-4H]$^{4-}$ and [dCGCGGGCCCGCG-5H]$^{5-}$ following photoabsorption around the C and P K-edges. However, the NDSED relative yield is low, as it appears to be much more probable that the decay of an initial 1s vacancy involves detachment of several valence electrons. This process is followed by extensive fragmentation, as very recently demonstrated for deprotonated oligonucleotides.[67] Consistently, in the present case, we detected abundant small fragment cations from deprotonated [dCGCGGGCCCGCG-4H]$^{4-}$ and [dCGCGGGCCCGCG-5H]$^{5-}$ after photoabsorption around the C and/or P K-edges. These results are shown in Figure 4.7 and Figure 4.8.

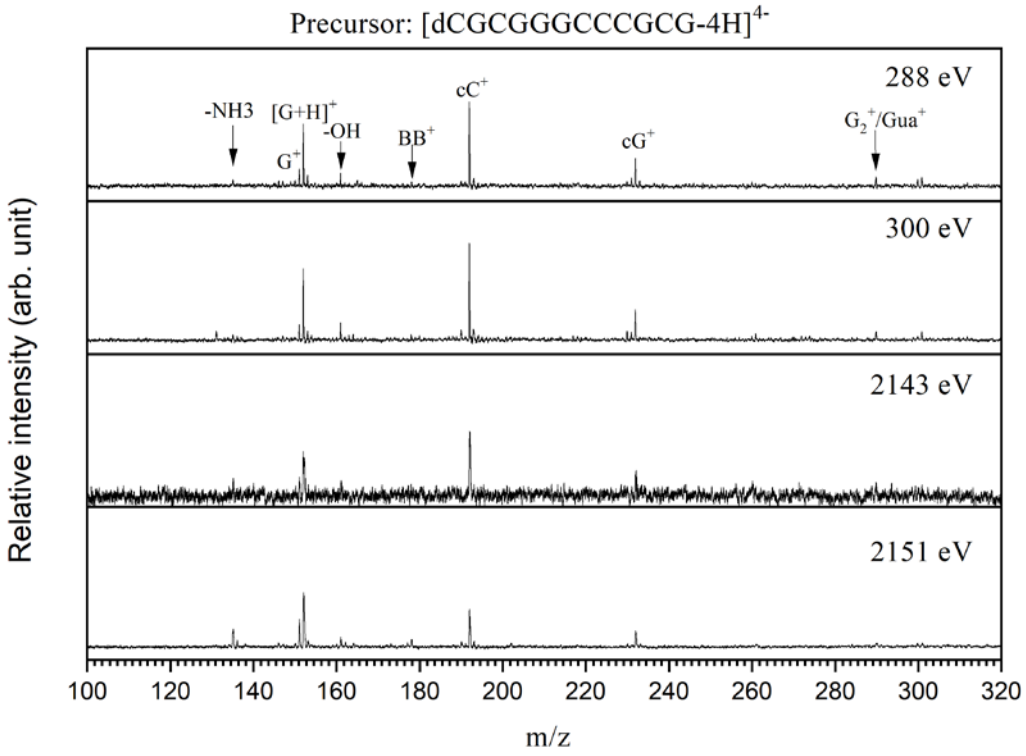

Figure 4.7: Mass spectra of cations formed from [dCGCGGGCCCGCG-4H]$^{4-}$ after single photon absorption around carbon (photon energy 288 and 300 eV) and phosphorus K-edges (photon energy 2143 and 2151 eV). Guanine radical cation and protonated guanine are denoted G^+ and $[G+H]^+$, respectively. cC^+ and cG^+ correspond to cyclic cytidine and guanosine nucleosides, BB^+ to a backbone fragment, G_2^+ to the guanine dimer and Gua^+ to a fragment shown in Scheme 2.

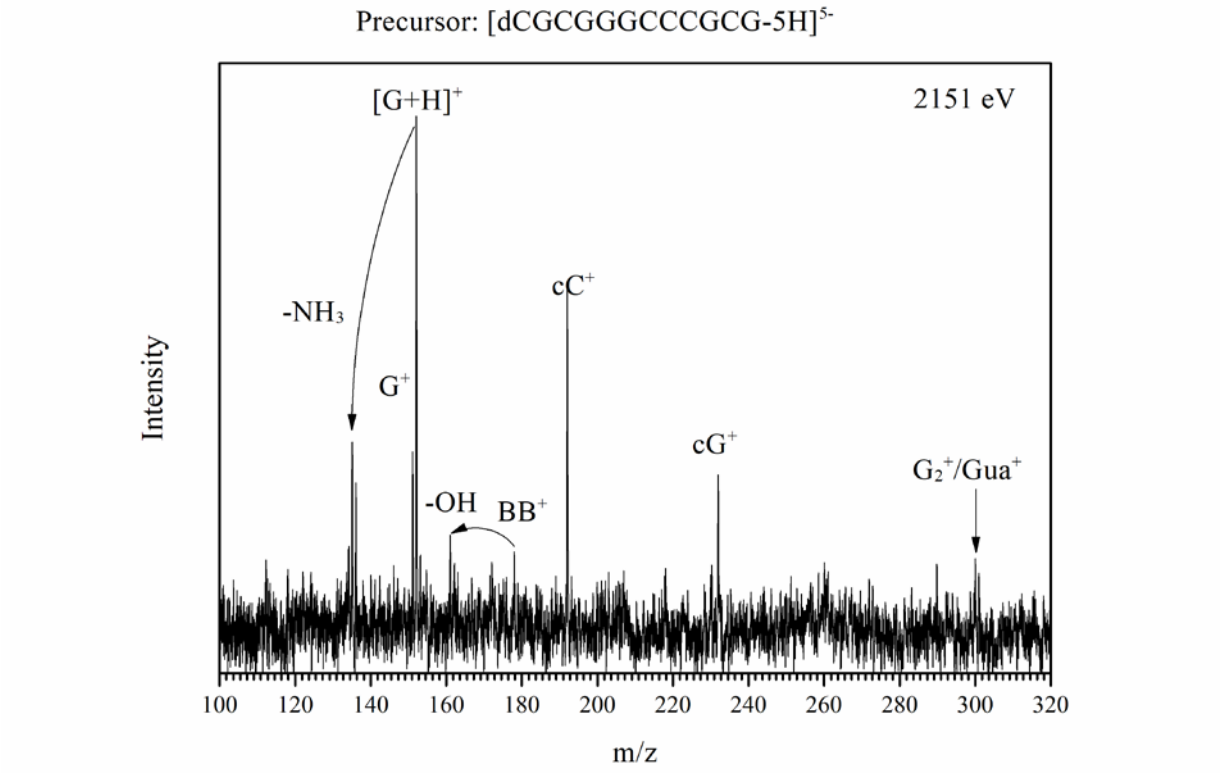

Figure 4.8: Mass spectra of cations formed from [dCGCGGGCCCGCG-5H]$^{5-}$ after single photon absorption around the phosphorus K-edge (photon energy 2151 eV). Guanine radical cation and protonated guanine are denoted G^+ and $[G+H]^+$, respectively. cC^+ and cG^+ correspond to cyclic cytidine and guanosine nucleosides, BB^+ to a backbone fragment, G_2^+ to the guanine dimer and Gua^+ to a fragment shown in Scheme 2.

In positive mode, the precursor is not visible because it is negatively charged. In these mass spectra, the most intense peaks can be assigned to the same singly-charged fragments as for other deprotonated oligonucleotides. The lightest ones are the guanine radical cation and protonated guanine (*m/z* = 151 and 152, respectively) as well as loss of NH_3 from the latter. Cytosine-related ions are not observed because their *m/z* ratios (around 110) are below the low-mass cutoff of the Paul ion trap. The peaks at *m/z* = 232 and 192 are due to fragments containing the guanine or cytosine nucleobase, respectively, and one sugar ring (see Scheme 2): they have been observed after collision-induced dissociation (CID) as well as ionization of multiply-protonated oligonucleotides,[64,137] and assigned to cyclic nucleosides, they are thus noted cG^+ and cC^+. The peak at *m/z* = 301 has previously been assigned to the guanine dimer formed after cleavage of two glycosidic bonds and one H or proton transfer[67], but another fragment might also explain the presence of this peak: it is noted Gua^+, and includes part of a neutral phosphoric acid group as well as one guanine moiety (see Scheme 2): this fragment requires the transfer of two H atoms or one H and one proton. Note that the fragments at *m/z* = 232 and 192 require the cleavage of backbone bonds (see Scheme 2) that have been shown to be also broken in the case of irradiation of DNA in solution by UV or protons at 70 MeV kinetic energy.[133] Nucleobase-related ions are formed after cleavage of the glycosidic bonds linking the backbone to nucleobases. Interestingly, the two peaks assigned to the fragments noted BB^+ and BB^+-OH are more intense for dCGCGGGCCCGCG than for previously studied oligonucleotides: these fragments both contain a sugar moiety and a phosphate group, and are therefore only due to backbone bond cleavage (*cf.* Scheme 2).

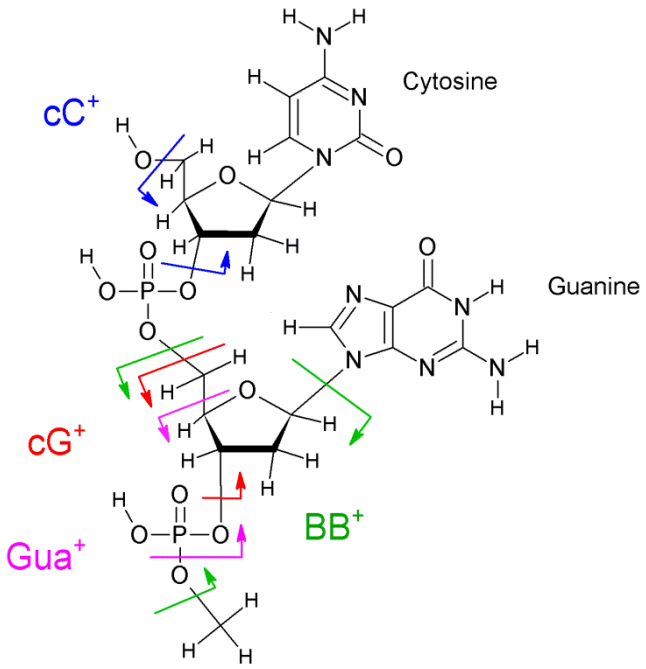

Scheme 2: Chemical structure of the two first nucleotides of the dCGCGGGCCCGCG oligonucleotide. The bonds that need to be cleaved to form the BB^+, cG^+, cC^+ as well as Gua^+ fragments are spotted with green, red, blue and purple lines with arrows indicating on which side of the bond the positive charge is located.

The mass spectrum of $[dCGCGGGCCCGCG\text{-}4H]^{4-}$ at 2143 eV photon energy is very similar to the ones at the C K-edge (288 and 300 eV), as shown in Figure 4.7. The reason is that DNA is mainly composed of carbon atoms, thus the cross-section for ejection of electrons from carbon dominates at photon energies much higher than the C, N and O K-edges, but lower than the P K-edge, such as 2143 eV. When increasing the photon energy in the P K-edge region, the main peaks in the MS are the same, though the intensity of each peak differs. That indicates no new ion channel is created when the energy increases from the C K-edge energy to phosphorus K-edge, which is quite surprising. It indicates that no matter which atom absorbs the photon energy (carbon or phosphorus), the energy tends to be transferred to the same bonds, causing the same bonds breaking and thus fragmentation. However, BB^+ becomes much more abundant at the P K-edge excitation energy of 2151 eV. This increase indicates localized fragmentation after site-specific photoabsorption at the phosphorus atoms and thus at the oligonucleotide's backbone. In addition, a surprising increase of the relative abundance of guanine-related ions is also observed at 2151 eV and above. Since phosphate groups are the most acidic sites in oligonucleotides, nucleobases are not expected to carry charge in deprotonated oligonucleotides, if the oligonucleotide's charge state is lower than the number of phosphate groups (which is the case here), as found by CID experiments.[138] The increase in G-related cations thus clearly demonstrates that inner-shell ionization in the backbone either facilitates hole transfer to the respective nucleobase, or that emission of valence electrons localized on the nucleobases is part

of the de-excitation process of the photoinduced P 1s hole. For instance, in the case of $[dG_6\text{-}3H]^{3-}$, Daly *et al.*[105] have found by quantum-chemical calculations that the electron density of molecular orbitals close to the HOMO in energy is high in guanines. Moreover, we have previously shown that several valence electrons are emitted from deprotonated oligonucleotides as a result of hole formation in C 1s orbitals.[67] Holes located in valence orbitals are likely to be transferred to guanine-rich regions,[66] which would then lead to guanine-related cations after glycosidic bond cleavage. It is important to notice that in the present case, the observation of positive fragments from 4- and 5- molecular anions implies ejection of at least five or six electrons. It is more than previously reported, but the binding energy of outer valence electrons drops with the charge state of the oligonucleotide procursor, for instance from 3.2 eV for the 2- charge state of deprotonated dGGGTTT to -0.2 eV for the 5-.[105] Negative values of the electron binding energy do not necessarily imply spontaneous electron emission, because of the Coulomb barrier between the ejected electron and the negative product ion. Our present results unambiguously demonstrate transfer of charge and/or energy from backbone to nucleobases after photoabsorption and ionization.

Formation of protonated nucleobases is a common process after ionization of neutral nucleosides,[58,125] but also after ionization of protonated or deprotonated oligonucleotides,[64,67] for a variety of ionizing particles. It is interesting to notice that starting from neutral nucleobase moieties, this process requires the transfer of two H atoms or of one H and one proton in addition to cleavage of one of the glycosidic bonds linking nucleobase and sugar moieties. For instance, here, to create protonated guanine, glycosidic bond cleavage is typically followed by H-transfer to form either neutral guanine or its radical cation, and a subsequent proton or H transfer is needed. Although transfer from another nucleobase is in principle possible, it is not supported by the observation of protonated nucleobases after ionization of sugar groups in neutral nucleosides, which only contain one nucleobase.[58,125]

4.3.3 Positive fragments yields

In order to quantitatively study the relationship between the yield of fragment cations from deprotonated $[dCGCGGGCCCGCG\text{-}4H]^{4-}$ after photoabsorption and the photon energy, we plot the yield of fragment cations from $[dCGCGGGCCCGCG\text{-}4H]^{4-}$ after single photon absorption as a function of photon energy (Figure 4.9). In general, the yields of some fragment cations increase from the carbon K-edge to the phosphorus K-edge energy, including $[G+H]^+$-NH_3, G^+, $[G+H]^+$. These cations are all base-related fragments. They probably all come from the same largest fragments that further break into these smaller base-related fragments. One of

these fragments can be cG^+ since its yield decreases from the carbon K-edge to the phosphorus K-edge energy. The yield of cC^+ shows the same behavior, even more pronounced, unfortunately the cytosine-related ions have m/z lower than the trapping cut-off related to the RF amplitude and thus cannot be detected. It indicates that the amount of vibrational energy of the oligonucleotide is higher after photoabsorption at the phosphorus K-edge. This might be linked to the much higher K-edge energy of phosphorus compared to carbon, allowing for a higher residual energy, even after ejection of the two 2s electrons (2*190 eV=380 eV) and three 2p electrons (3*130 eV=390 eV). It means that after subtraction of the total 770 eV electron binding energy, the remaining energy (1381 eV) from the 2151 eV photon energy is still much higher than that of the carbon K-edge energy. This remaining energy is distributed between kinetic energy of the ejected electrons and internal energy of the molecule. More information would be gained by measuring the kinetic energy of the ejected electrons.

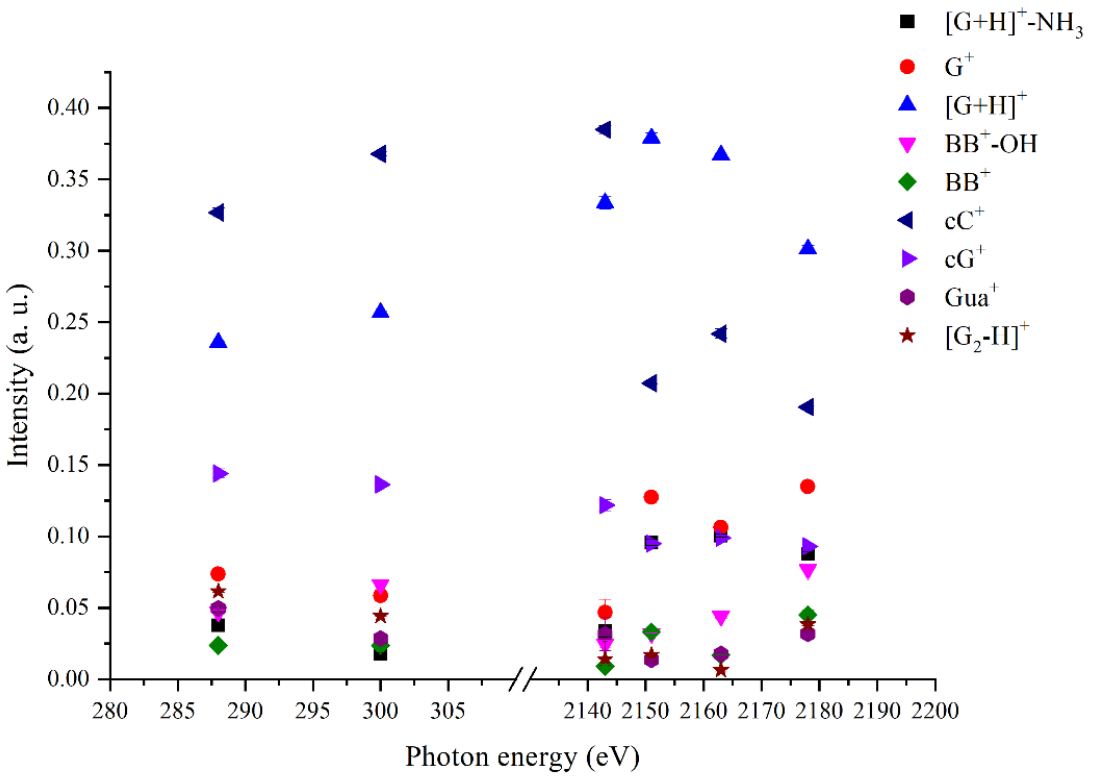

Figure 4.9: Relative yield of fragment cations from $[dCGCGGGCCCGCG-4H]^{4-}$ after single photon absorption, as a function of photon energy around the C K-edge and P K-edge, obtained by calculating the area under the peak in the mass spectrum and normalizing by the total area under all the listed ion peaks. Error bars represent the standard deviation of the average value from three independent calculations (n = 3).

4.4 Conclusions

In this chapter, we have investigated the outcomes of selective photoabsorption occurring at the DNA oligonucleotide backbone in the gas phase, focusing on its effects on charge, energy,

and hydrogen transfer processes. By interfacing our setup with the variable polarization XUV beamline P04 at the PETRA III synchrotron, we are able to tune the X-ray photon energy around 2160 eV, which corresponds to the K-edge of the phosphorus atoms at the isolated DNA oligonucleotide backbone. In this way, we have targeted the backbone of DNA. With this setup, we have analyzed the ionic products by mass spectrometry. We have identified the X-ray spectral signatures of selective photoabsorption at the DNA oligonucleotide backbone, and clearly showed the charge, energy and hydrogen transfer from the backbone to the nucleobases.

In the future, we plan to study the timescale of these transfer processes. In addition, further experiments will be carried out on non-covalent DNA models such as the Watson–Crick double helix, the i-motif, or the G-quadruplex. It will be interesting to study these non-covalent DNA systems and see if the H-bond network alters the processes for the covalent DNA system which we have studied in this chapter.

5 Irradiation of isolated DNA oligonucleotides by 0.8 MeV/amu carbon ions

5.1 Introduction

In the previous chapter, we have discussed the irradiation of isolated DNA oligonucleotides by photons, which reveals the mechanism of radiotherapy at the molecular level. In particular, we observed the charge, energy and H transfer between backbone and nucleobases in isolated DNA oligonucleotides. As we know, hadrontherapy with a hadron beam, such as protons and carbon ions, is considered as a potential competitor to conventional photon radiotherapy, thanks to its advantages of precise tumor targeting, superior ballistic properties and biological efficiency in killing cells.[139] With the fundamental interest of comparing the effects of two different ionizing particles (photons and carbon ions) that have different interaction characteristics, we wondered if we could observe the same or similar charge, energy and H transfer in the same DNA sequences.

Among all kinds of ion species for hadrontherapy, carbon ions are widely used worldwide due to their exceptional properties, which provide the most optimal balance between physical and biological effective dose localization in tumors.[140] This is because the carbon ion beams offer superior precision in dose delivery compared to photon beams. The key factor contributing to this precision is the presence of a Bragg peak in the energy deposition profile of the carbon ion beam. Unlike photon beams, which deliver radiation uniformly along their path, carbon ion beams concentrate the majority of their energy release at a fixed depth within the tissue, resulting in the Bragg peak and minimizing radiation exposure to the neighboring healthy tissues. Moreover, owing to their greater mass compared to protons, carbon ions exhibit a biological effectiveness that increases as they penetrate deeper into tissue. This effectiveness peaks at the terminus of the beam's range. Notably, this property is particularly well suited to the goals of cancer radiotherapy, rendering carbon ions an exceptionally promising choice.

Thus, we have used carbon ion beam for the irradiation of isolated DNA oligonucleotides in the experiments discussed in this chapter. When recording these mass spectra, we used the same oligonucleotide sequence and the same setup in the previous chapter, in order to compare the same ions in positive and negative mode under the similar experimental conditions.

During the beamtime, to simulate the clinical case, the carbon ion beam kinetic energy was set around 1 MeV/amu because it corresponds to the Bragg-peak energy of the ions used in

hadrontherapy. In the previous studies, there are some works on ions at this Bragg-peak energy, targeting peptides[136] or RNA nucleobases[141,142] but so far only experiments at keV kinetic energy on oligonucleotides[64]. However, since genomic DNA that is not at the transcription stage is mostly in the form of double strand instead of single strand to carry the gene information, it is of great importance to investigate the effect of irradiation on double strand DNA. Although there are many works that study the irradiation of double strand DNA in the condensed phase by ionizing radiation,[133,143–147] such a study of double strand DNA in the gas phase has never been reported before, to the best of our knowledge. One great challenge is to retain the noncovalently-bound double helix DNA structure from solution to the gas phase. We have solved the problem and confirmed the presence of the double helix DNA structure in the gas phase for high charge states of the double strand of the dCGCGGGCCCGCG oligonucleotide (results shown in Chapter 3). Here, by means of an electrospray ionization source in soft mode (see the experimental section for details), we have successfully isolated and irradiated deprotonated oligonucleotide monomers and a double helical dimer by carbon ions in the gas phase.

5.2 Experimental details

A powder of the dCGCGGGCCCGCG oligonucleotide of up to 85% purity (Reverse-Phase HPLC purified, Eurogentec, Seraing, Belgium) was dissolved without further purification in a mixed solvent of 50% HPLC methanol, 50% deionized water and 1% ammonium hydroxide, at a final concentration of 100 µM. To make double strand DNA from single strand DNA in this aqueous solution with ammonium hydroxide, we first performed DNA annealing with the dCGCGGGCCCGCG self-complementary sequence oligonucleotide. DNA annealing is the process of heating and cooling two single strand oligonucleotides with complementary sequences. The heating process (95ºC for 2 mins) breaks all hydrogen bonds, and then the cooling process (slowly cooling to room temperature) allows new hydrogen bonds to form between the two sequences. It should be noted that even without annealing, two complementary sequences in the solution at room temperature can form double strand DNA spontaneously. However, the annealing procedure, heating followed by cooling, facilitates the formation of double strand DNA, because the heating process will break the undesired, no-specific duplexes or intramolecular hairpins. In this way, even though the hydrogen bonds do not become more "tight", the number of hydrogen bonds is increased. In other words, the concentration of the dimers is higher. Therefore, we have more dimers to be sent to the Paul trap. What's more, we tried to minimize collision-induced dissociation when the double strand DNA molecules enter

the vacuum chamber after the ESI source. To achieve this, we had optimized all the optic parameters all the way from the capillary to the Paul trap to make sure that the DNA dimers were in a soft environment before irradiation. The method was to try to get as much precursor ions as possible during optimization.

Irradiation of DNA oligonucleotides by carbon ions were carried out at the GANIL facility in Caen (France). It was achieved by coupling the tandem mass spectrometer described in Section 2.1 to the IRRSUD beamline described in Section 2.3.

The oligonucleotide solution was introduced in a syringe and pushed towards the needle of an in-house-built electrospray ionization (ESI) source under atmospheric conditions, using a syringe pump with a flow rate of about 0.10 mL/h. By applying a high voltage around -3.7 kV to the metal needle of the ESI source placed under atmospheric pressure, a high electric field was created between the needle and a metal capillary, which played the role of a counter electrode (-250 V). After the solvent evaporation process between the needle and the capillary, the ions are transported to the first vacuum chamber at a pressure of about 10^{-1} mbar and focused along a funnel of 26 electrodes on which a radio frequency of about 730 kHz was applied. Then they are guided into the next vacuum chamber. The pressure there is close to 10^{-3} mbar. Then the ions are guided using the octopole in this chamber with a radio frequency of 370 kHz and amplitude of 470 V. Subsequently, the molecular ion of interest is injected during a controlled time (about 50 ms) and selected according to its mass to charge ratio (*m/z*) in a quadrupole mass analyzer (QMS). The filtered ions are then accumulated in a three-dimensional RF trap (Paul trap) whose annular electrode is brought to a radio frequency voltage whose amplitude is variable from 0 to 2 kV. After accumulation, the trapped ions are irradiated by MeV ions during a controlled time. After interaction, either the negatively charged products and precursors left or the positively charged products were extracted from the trap by a pulsed electric field, depending on the polarity of the bias voltages on the RF trap end caps. Then, the ions entered into a reflectron time-of-flight (Re-TOF) mass spectrometer where they were accelerated by a uniform electric field, then reflected by an electrostatic mirror, and finally detected by a microchannel plate (MCP) detector. The MCP had a front plate biased at -2.5 kV and an anode plate at ground potential for detecting cations, but these values were +2.5 and +4.5 kV for anions.

The same data acquisition method as the one described in Section 4.2.1 was used to extract mass spectra. During data processing, we had performed the "Fast Fourier Transform" (FFT)

filtering to remove the noise from the mass spectra. This filtering was done in the software of OriginPro 8.5. The filter type was low pass and the cutoff frequency was 20 MHz.

5.3 Results and discussion

5.3.1 Negative and positive ions from the oligonucleotide monomer

In Chapter 4, we presented the results of irradiation of isolated DNA oligonucleotides by X-ray photons. Here, we irradiated the same deprotonated DNA oligonucleotide (dCGCGGGCCCGCG) by $^{13}C^{3+}$ carbon ions at 10.4 MeV kinetic energy. The corresponding mass spectrum for the negative ionic products of the 4- precursor (*m/z* 911) is shown in Figure 5.1. The signal corresponding to the precursor ion depletion is negative due to data analysis (see section 2.1). Positive peaks appear only around *m/z* 1214, and are assigned to non-dissociative single electron detachment (NDSED). We also observed NDSED in the case of X-ray photons (*cf.* Chapter 4), but two peaks assigned to internal fragments due to backbone cleavage were present as well, their intensity being much lower (except when the photon energy was set to 288 eV). It means we observed similar results with both $^{13}C^{3+}$ carbon ions and X-ray photons. We expected such similarity since both particles interact with the electrons of the precursor and eject at least one of them. The absence of fragments in the case of carbon ions can be linked to the different orbitals targeted by ions at this kinetic energy. Indeed, for MeV projectiles, the cross-section σ for an ion of charge *q*, mass *M* and kinetic energy *E* interacting with one electron of mass *m* and binding energy I_P is, according to a classical calculation of ion-electron momentum transfer:

$$\sigma = \pi \frac{M}{m} \left(\frac{e}{4\pi\epsilon_0} \right)^2 \frac{q^2}{I_P E}$$

Thus ejection of electrons from valence orbitals dominate with the carbon ions at MeV kinetic energy, whereas photons of energy close to atomic K-edges excite 1s core electrons and thus leave the molecule with a higher excess vibrational energy (around 20 eV for the carbon K-edge) after Auger electron emission.[135] Similar results for protonated peptides after irradiation by X-ray photons and carbon ions were also reported by Lalande *et al.*[136] It is worth noting that we observed several peaks at higher *m/z* (around 1222, 1229, and 1236) than the peak at *m/z* 1215 (shown in the insert of Figure 5.1). The same additional peaks are also observed for the precursor, and in both cases their *m/z* ratio correspond to additional masses of +22, +44 and +66 amu: thus, we attribute them to sodium adducts substituting protons in the

oligonucleotide. These sodium adducts also confirmed that the peak around *m/z* 1215 corresponds to NDSED instead of a fragment which would have the same *m/z* ratio. Their presence is due to the fact that this DNA oligonucleotide had not been desalted by the gel filtration medium (Sephadex G25) used in Chapter 4, where the mass spectra showed no such peaks assigned to sodium adducts. Non-dissociative multiple electron detachment is not observed after carbon ion impact on $[dCGCGGGCCCGCG\text{-}4H]^{4-}$, in contrast with the case of VUV photon (15 - 30 eV) absorption by other deprotonated oligonucleotides of similar length[66], despite the fact that valence electrons are mostly targeted in both cases.

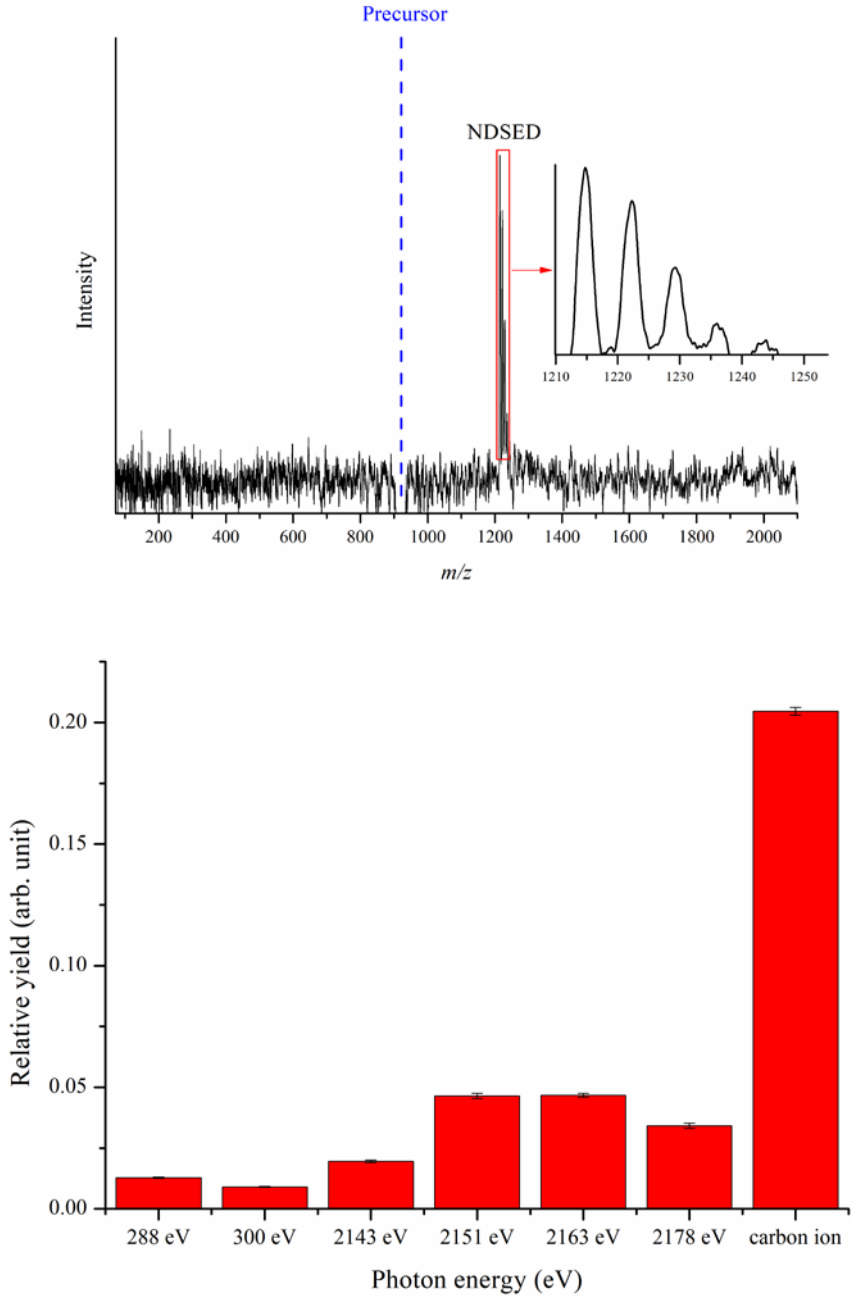

Figure 5.1: Top: mass spectra of the negative products of [dCGCGGGCCCGCG-4H]$^{4-}$ after irradiation by $^{13}C^{3+}$ carbon ions at 10.4 MeV kinetic energy. Bottom: relative yield of non-dissociative single electron detachment from [dCGCGGGCCCGCG-4H]$^{4-}$ after single photon absorption and carbon ion collision. The precursor peak position is indicated by blue dashes. Error bars represent the standard deviation of the average value from three independent calculations (n = 3).

To calculate the NDSED yield resulting from carbon ion colliding with [dCGCGGGCCCGCG-4H]$^{4-}$, the integrated area under the NDSED product peaks (including the sodium adducts) is divided by the integrated area under the precursor peaks (also including the sodium adducts). No correction to account for the difference in detection efficiency was made, since the *m/z* of the two species are not strongly different. The same calculation is also done for the NDSED yield resulting from X-ray photons interacting with [dCGCGGGCCCGCG-4H]$^{4-}$, except that there are no sodium adducts peaks in that case. Surprisingly, the NDSED yield after carbon ion collision is much higher than after X-ray photon absorption (factors of about 4 and 10 compared to P and C K-edges, respectively), as shown in Figure 5.1. In the case of [dTG$_4$T-2H]$^{2-}$, the NDSED yield was very low for both photoabsorption at the C K-edge (288 and 300 eV) and collision with $^{12}C^{4+}$ at 11.76 MeV.[67] Interestingly, for carbon ion collision, this low yield was not compensated by the yield of positive fragments formed after the detachment of at least 3 electrons from [dTG$_4$T-2H]$^{2-}$, which had been explained by formation of neutrals after the detachment of 2 electrons. Here, for [dCGCGGGCCCGCG-4H]$^{4-}$, we do not detect non-dissociative double-electron detachment (*m/z* 1824), neither negative fragments, and we will see later that abundant positive fragments are created after carbon ion collision. Therefore, we suspect that formation of negative fragments as well as detachment of 2 electrons are quenched by the size of dCGCGGGCCCGCG that is twice larger than dTG$_4$T, due to redistribution of the deposited vibrational energy into the molecular degrees of freedom. It is surprising because single and multiple electron detachment are believed to be non-statistical.[106]

It should also be noticed that in previous and present collisions between oligonucleotides and carbon ions, the charge state (q = 3 *vs.* 4) and mass (M = 13 *vs.* 12) of the carbon projectile ion were different. However, we do not expect the consequences on electron emission and fragmentation to be significant, given the results of experiments performed by the group of L. Tribedi, consisting in irradiating gas-phase uracil molecules by carbon and oxygen ions in the 1 – 10 MeV/amu kinetic energy range: they found very similar mass spectra for the 4+, 5+ and 6+ charge states of carbon as well as for oxygen ions.[141]

As we mentioned, for [dCGCGGGCCCGCG-4H]$^{4-}$, we do not detect non-dissociative double-electron detachment (m/z 1824), neither negative fragments that could provide the yield

of 80% complementary to that of non-dissociative single-electron detachment (see Figure 5.1). Therefore, we expect that abundant positive fragment ions are created after carbon ion collision. To confirm this, we have switched the detection mode from negative to positive with the same precursor. The resulting mass spectra are shown in Figure 5.2 and Figure 5.3. Interestingly, the mass spectrum in Figure 5.2 contains all the peaks observed in the mass spectrum after X-ray irradiation (Figure 4.7). In addition, they are quite similar even in relative intensity: for example, the most intense peaks are assigned to protonated guanine, the cyclic guanine nucleoside (cC^+) and the guanine radical cation. On the other hand, we can observe some new peaks compared to the one after X-ray irradiation at 174, 201, 214, 223, 254, 281 *m/z*, respectively.. These peaks are also observed in Figure 5.3, which has eliminated the influence of the residual gas irradiation. Thus, we can conclude that these peaks are the products of the oligonucleotide after carbon ion irradiation, although we cannot assign it for this moment.

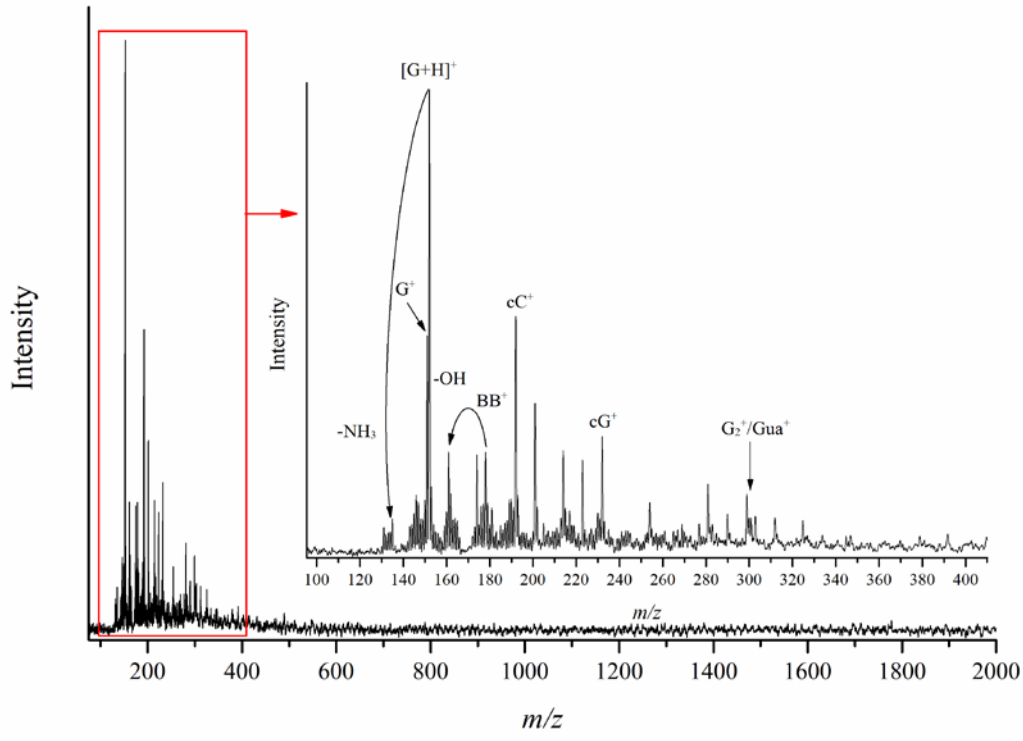

Figure 5.2: Mass spectrum of the positive products of [dCGCGGGCCCGCG-4H]$^{4-}$ after irradiation by $^{13}C^{3+}$ carbon ions at 10.4 MeV kinetic energy for a trap RF voltage of 2000 V.

The experimental mass spectrum shown in Figure 5.3 was recorded in similar conditions with respect to the one in Figure 5.2. However, the data analysis is different in the case of Figure 5.3. As we have described in the experimental part of section 4.2.1, we have recorded an ONLY ESI spectrum in order to subtract it from the ESI + BEAM spectrum. However, here we have

also recorded a mass spectrum of the ionized content of the Paul trap filled only by the residual gas. This spectrum is labeled as ONLY BEAM. To get the mass spectrum in Figure 5.3, the ONLY ESI and the ONLY BEAM spectra are subtracted from the ESI + BEAM spectrum. Because the ONLY BEAM spectrum is taken after the ONLY ESI and ESI + BEAM spectra, the experimental conditions might not be exactly the same. It induces the few undesirable negative peaks in Figure 5.3. Due to the fact that negative peaks are present here, we will not go too far in the analysis of this spectrum. We will only comment on some important peaks here.

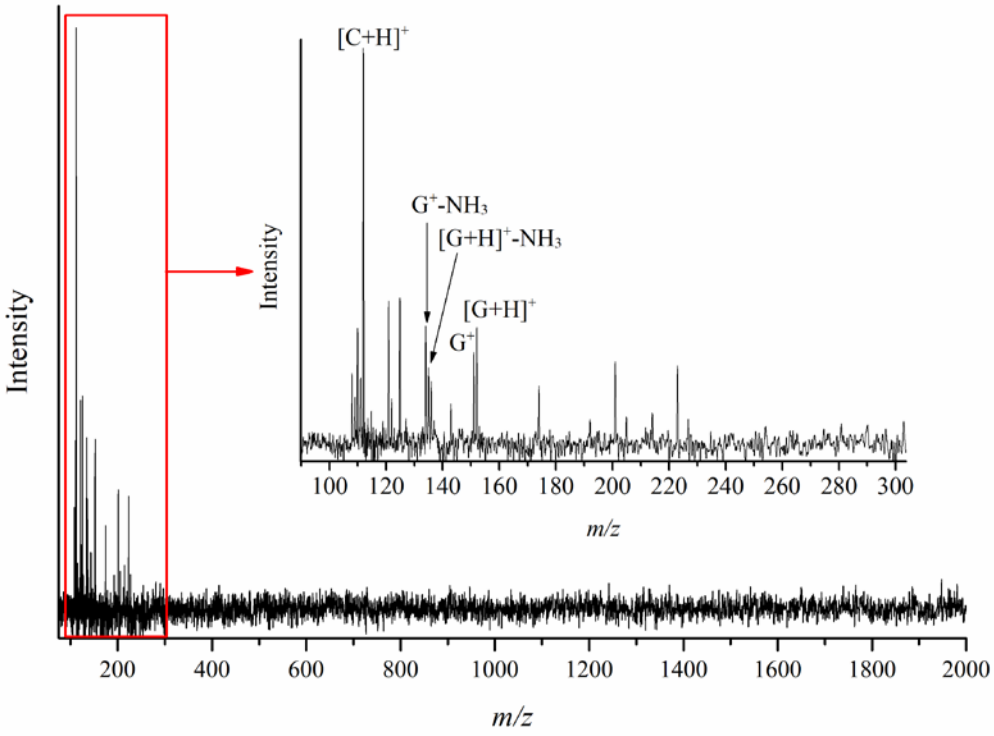

Figure 5.3: Mass spectrum of the positive products of [dCGCGGGCCCGCG-4H]$^{4-}$ after irradiation by $^{13}C^{3+}$ carbon ions at 10.4 MeV kinetic energy for a trap RF voltage of 1650 V.

Importantly, in the mass spectrum of Figure 5.3, we have observed a peak at 112 *m/z*, which can be attributed to protonated cytosine, $[C+H]^+$. This peak could not be detected in the case of photoabsorption in Chapter 4 (*cf.* Figure 4.7) or in the mass spectrum of Figure 5.2, because of the higher *m/z* threshold of the Paul trap. In this experiment, the RF voltage amplitude of the Paul trap is lower so it can trap ions with lower *m/z*. We can also observe a smaller peak at 111 *m/z*, which can be attributed to the cytosine radical cation. The ratio of $C^+/[C+H]^+$ (0.018) is much lower than $G^+/[G+H]^+$ (0.81), which is consistent with a previous report[64], where the intensity of C^+ is negligible after ionization of the protonated dGCAT oligonucleotide by

energetic photons ($h\nu$ = 10 – 570 eV) and keV C^{q+} ions. It points towards an intrinsic property of cytosine, maybe its high proton affinity (9.85 eV according to the NIST), which would mean that proton transfer is responsible for the formation of protonated cytosine, whatever the ionizing radiation used. Note that H transfer to cytosine is also required to form this ion, in addition to glycosidic bond cleavage. Furthermore, considering the fact that there are equal amounts of C and G in this oligonucleotide, it is surprising that the $[C+H]^+$ peak dominates in the mass spectrum. The same has been reported for protonated dGCAT oligonucleotide by energetic photons ($h\nu$ = 10 – 570 eV) and keV C^{q+} ions.[64] It cannot be explained by proton transfer or hole transfer because guanine has the highest proton affinity and lowest ionization energy.[125] It might be linked to the process of multiple electron detachment after decay of a 1s vacancy created by the ejection of one core electron, a process that has been shown to occur for carbon ions,[67] even though ejection of valence electrons is dominant.

5.3.2 Negative ions from the GC oligonucleotide dimer

We have succesfully accumulated the dimer of the dCGCGGGCCCGCG oligonucleotide with 7 negative charges in the Paul trap. Then we have irradiated it with $^{13}C^{3+}$ carbon ions at the same kinetic energy as the monomer oligonucleotide and the corresponding mass spectrum for negative ions is shown in Figure 5.4. The negative intensity peaks around 1041 *m/z* are due to the precursor ion $[d(CGCGGGCCCGCG)_2\text{-}7H]^{7-}$ and its sodium adducts. There is only one group of positive peaks around 1240 *m/z*. If we zoom in to have more details, we can see that this peak includes many peaks. The interval between each peak is 3.66 *m/z*. When we multiply it by 6, we get 22 *m/z*, which means these peaks can also be attributed to the sodium adducts with 6 negative charges. Therefore, we assign these peaks to product ions from non-dissociative single-electron detachment (NDSED) from the $[d(CGCGGGCCCGCG)_2\text{-}7H]^{7-}$ precursor dimer.

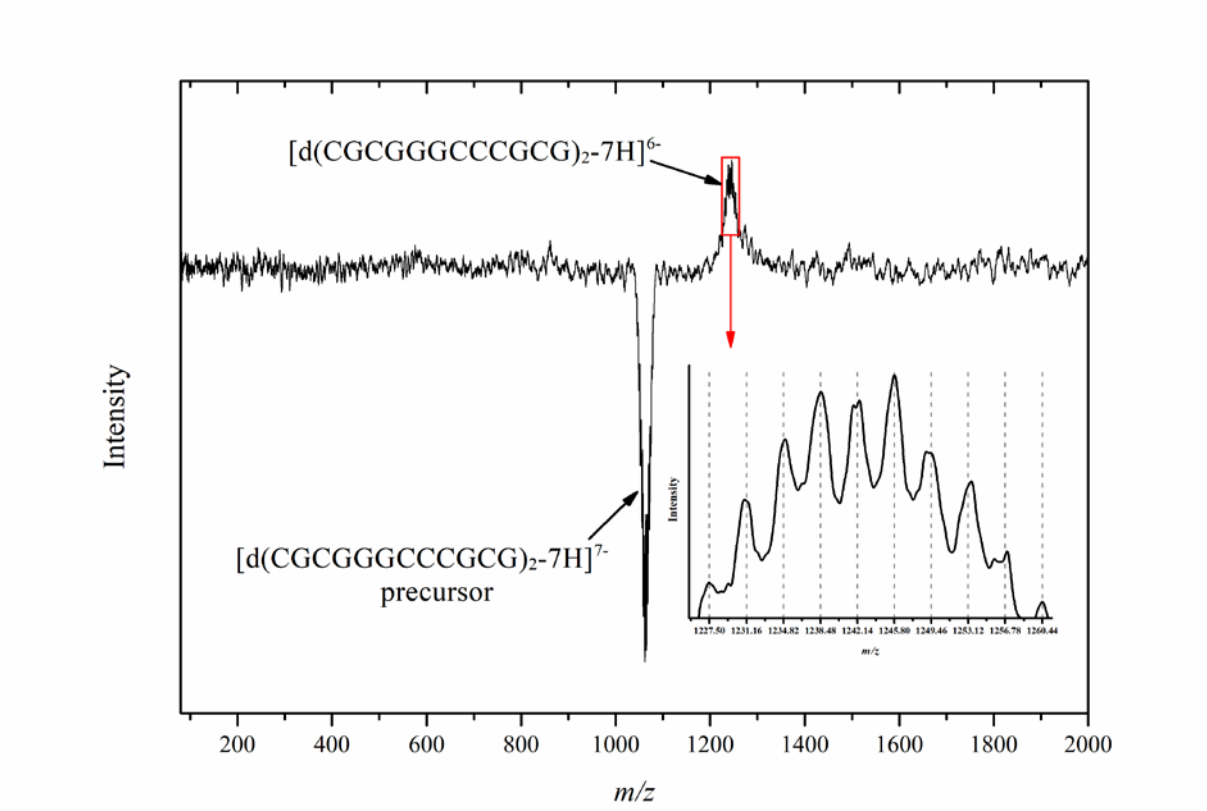

Figure 5.4: Mass spectrum of the negative products of [d(CGCGGGCCCGCG)$_2$-7H]$^{7-}$ after carbon ion irradiation. The dash line is used to show the same interval (3.66 m/z) between each peak.

Because the precursor dimer [d(CGCGGGCCCGCG)$_2$-7H]$^{7-}$ is composed of two identical molecules, its 7 charges should be statistically distributed, thus we expect it to contain one oligonucleotide [dCGCGGGCCCGCG-3H]$^{3-}$ and one [dCGCGGGCCCGCG-4H]$^{4-}$. After irradiation and electron detachment, the [d(CGCGGGCCCGCG)$_2$-7H]$^{6-}$ dimer may dissociate into two monomers. The most likely is symmetrical charge separation to form two 3- monomers. The theoretical average *m/z* ratios of the 3- monomer and the 6- dimer are quite close to each other. However, the interval between the peaks due to sodium adducts for the 3- monomer is twice that for the 6- dimer. Thus, any significant contribution of the 3- monomer would result in alternately high and low peak intensities. Figure 5.4 gives evidence that the peaks in this *m/z* range are only due to the 6- dimer: the distribution looks mostly gaussian, reflecting a statistical distribution of sodium atoms in the dimer. Therefore, we conclude that after $^{13}C^{3+}$ carbon ion irradiation, dissociation of the [d(CGCGGGCCCGCG)$_2$-7H]$^{6-}$ dimer into two [dCGCGGGCCCGCG-3H]$^{3-}$ is negligible.

When we compare the mass spectra of the negative product ions of the dimer [d(CGCGGGCCCGCG)$_2$-7H]$^{7-}$ after carbon ion irradiation with the one of the monomer [dCGCGGGCCCGCG-4H]$^{4-}$, we find that both of them only contain peaks assigned to NDSED

products. However, a strong difference appear if we compare the relative yield of their NDSED products, as shown in Figure 5.5, we find that it is 70% for the dimer $[d(CGCGGGCCCGCG)_2\text{-}7H]^{7-}$, which is much higher than that of the monomer $[dCGCGGGCCCGCG\text{-}4H]^{4-}$ (20%). In the latter case, intense positive ions were detected (see the previous sub-section 5.3.1), which accounted for at least part of the complementary 80% depletion of the precursor ions due to carbon ion collision. Formation of positive ions from a 4- precursor ion most probably requires detachment of at least 5 electrons, while for a 7- it would increase to 8 electrons, strongly decreasing the probability of this process and providing an explanation for the sharp increase of the NDSED yield for the 7- dimer. However, we should also consider the twice larger size of the dimer, which may bring several additional effects. The first is the higher probability of multiple collisions between the carbon ion and electrons of the precursor target, which has been shown to cause more fragmentation of a multiply-protonated peptide trimer compared to the monomer.[136] On the other hand, the larger size of the dimer makes it more capable of absorbing the excess vibrational energy resulting from collision by the carbon ion, which reduces fragmentation after redistribution of the excess energy into the vibrational degrees of freedom. One could argue that the hydrogen bonds between the two single strands of the dimer are one order of magnitude weaker than the covalent bonds of a monomer, but the dimer contains 36 H-bonds if its geometrical structure is a double helix (see Section 1.2), which makes the dimer binding energy much higher than a single covalent bond. An estimation of this energy can be given by multiplying the experimental binding enthalpy of the isolated guanine-cytosine base pair (about 1 eV[148]) by 12, giving 12 eV, eventually a very high value compared to covalent bonds in DNA. As we see a great majority of intact dimers after carbon ion irradiation, it means that the average vibrational energy present in the dimer after carbon ion collision is lower than 12 eV. This is lower than the value of 20 eV obtained in the case of photoabsorption of a 288 eV photon by peptides and proteins, corresponding to excitation of a 1s electron of carbon.[128] It would be highly valuable to perform X-ray photoabsorption experiments on the $[d(CGCGGGCCCGCG)_2\text{-}7H]^{7-}$ dimer to see if dissociation occurs.

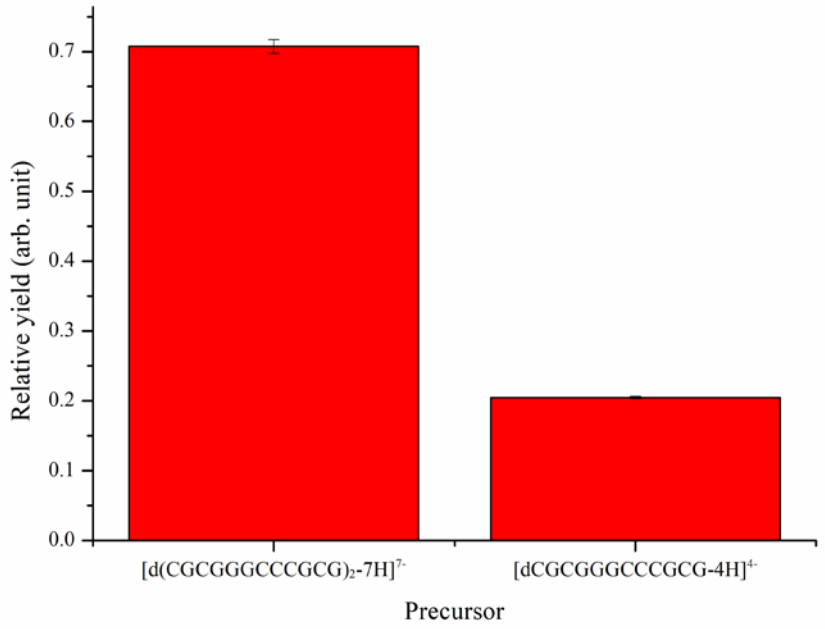

Figure 5.5: Relative yield of non-dissociative single electron detachment from the dimer $[d(CGCGGGCCCGCG)_2\text{-}7H]^{7-}$ and the monomer $[dCGCGGGCCCGCG\text{-}4H]^{4-}$ after irradiation by $^{13}C^{3+}$ carbon ions at 10.4 MeV kinetic energy. Error bars represent the standard deviation of the average value from three independent calculations (n = 3).

5.4 Conclusions

In this chapter, we have studied the results of irradiation of the DNA oligonucleotides by $^{13}C^{3+}$ carbon ions in the gas phase. By interfacing a tandem mass spectrometer with the IRRSUD beamline at the GANIL facility, we were able to tune the kinetic energy of the carbon ion beam to 0.8 MeV/amu, which is at the Bragg-peak energy. For the oligonucleotide monomer, we have observed non-dissociative single electron detachment (NDSED) as well as extensive dissociation following the detachment of more than 4 electrons, which is similar as the case of irradiation by X-ray photons. However, there is no non-dissociative multiple electron detachment after carbon ion impact, which is different from the case of VUV photon absorption. Moreover, the NDSED yield is much higher than after X-ray photon absorption. This is broadly consistent with the fact that carbon ions in the MeV kinetic energy range eject mainly valence but also core electrons, creating 1s vacancies with low but not negligible probability.

What's more, we have for the first time successfully irradiated a DNA double helix in the gas phase. After carbon ion irradiation, mainly NDSED occurs, and no single strand products dissociated from the double strands are observed. Interestingly, the NDSED product yield is much higher than that for the single strand DNA, because a DNA double strand ion with 7 negative charges most probably requires detachment of at least 8 electrons to form a positive

ion from the precursor ion. The low probability of this event may explain the sharp increase of the NDSED yield for the $[d(CGCGGGCCCGCG)_2\text{-}7H]^{7-}$ dimer.

In the future, we plan to perform more experiments for the same DNA oligonucleotide after X-ray photoabsorption, in order to check the difference between X-ray photoabsorption and carbon ion impact. In addition, we will explore more non-covalent DNA structures such as i-motif and G-quadruplex after irradiation by carbon ions.

6 Summary and perspectives

Ionizing radiation is a type of radiation that removes electrons from atoms and molecules found in materials such as air, water, and living tissue, thereby ionizing them. Since the groundbreaking discovery of X-rays by Wilhelm Röntgen in 1895 scientists from around the globe have dedicated their efforts to investigate the characteristics, mechanisms, and impact of ionizing radiation on human health. The most common and important lesions caused by ionizing radiation are those that affect DNA, which is the focus of this thesis.

Taking advantage of the DNA damage caused to cancer cells by ionizing radiation, researchers have developed radiation therapy to treat cancer. In the clinical application of radiation therapy, several beams of different particles are used: electron beams, photon beams and hadron beams. We focus mainly on the latter two types of beam, photon beams and ion beams in this thesis.

In order to study the processes that take place after direct interaction between DNA and ionizing radiation, such as the transfer of charge, atoms and energy within DNA molecules, we performed our experiments in the gas phase rather than in the condensed phase. To carry out the analysis in the gas phase, the experiments were carried out using a powerful gas-phase analysis tool, the tandem mass spectrometer. We have used two different tandem mass spectrometers in this thesis. One is a commercial tandem mass spectrometer with an ion mobility analyzer. It helped us to get the *m/z* and the ion mobility of the DNA ions we were interested in. Moreover, it can perform CID experiments. Another is a home-built tandem mass spectrometer from Thomas Schlathölter's group. It has a Paul trap, which allows the accumulation of gas-phase DNA molecules to reach sufficient target density to carry out mass spectroscopic studies of DNA molecules in response to ionizing radiation. In addition, it is flexible and portable enough to interface with various sources of ionizing radiation, such as synchrotron user facilities and heavy ion accelerators. Therefore, it allows us to study and compare the processes within DNA induced by photons and heavy ions.

In Chapter 3, we have studied a DNA oligonucleotide using ion mobility-tandem mass spectrometry. The basic aim is to study the geometrical structure of a double strand DNA in the gas phase and to investigate its CID processes. The sequence of the DNA oligonucleotide is dCGCGGGCCCGCG, which means that it can self-assemble into a DNA duplex in the solution. The same sequence is used in Chapters 4 and 5 for the irradiation of isolated DNA oligonucleotide, in order to compare the different effects of photons and carbon ions. In the MS

mode, we have identified many different DNA ions with different charges or structures, including single strand DNA and double strand DNA. We found that the DNA dimers with an unambiguous mass-over-charge ratio are the ideal targets for studying double strand DNA, thanks to their purity. In the MS/MS mode, by selecting the double strand DNA with the quadrupole mass filter, we can trap and accumulate the double strand DNA molecules in the ion trap, and use them for the following CID experiments. In the CID experiments, we observed that the precursor $[d(CGCGGGCCCGCG)_2\text{-}5H]^{5-}$ dimer was separated into two monomers ($[dCGCGGGCCCGCG\text{-}3H]^{3-}$ and $[dCGCGGGCCCGCG\text{-}2H]^{2-}$) due to the increase in vibrational energy caused by multiple collisions with the gas, but other channels are also present, such as loss of guanine or cytosine without dissociation of the dimer. In addition, we have obtained the ion mobilities of the DNA ions in the MS mode, which can be converted to the CCS. The CCS of the $[d(CGCGGGCCCGCG)_2\text{-}5H]^{5-}$ dimer is lower than the expected one for the canonical B-helix, possibly due to novel phosphate-phosphate interactions.[101] Besides, we found that the CCS of DNA increases with the charge state, due to the unfolding the DNA structure and the stronger gas-molecular ion (charge-induced dipole) interaction. The structure of $[d(CGCGGGCCCGCG)_2\text{-}6H]^{6-}$ is closer to a canonical B-helix, thus we expect $[d(CGCGGGCCCGCG)_2\text{-}7H]^{7-}$ to be even closer.

In Chapter 4, we present experimental results from specific photoabsorption at the backbone of the dCGCGGGCCCGCG DNA oligonucleotide. In particular, we targeted on the phosphorus atoms, which are located only at the backbone of DNA oligonucleotides by tuning the X-ray photon energy to about 2160 eV (the phosphorus K-edge) at the U49/2-PGM1 beamline of the BESSY II synchrotron facility. After specific photoabsorption, we analyzed the ionic products by mass spectrometry. Remarkably, the most abundant negative ion produced by single-photon absorption is due to non-dissociative single electron detachment (NDSED). The yield of negative fragments is very low compared to the NDSED yield. This very low fragmentation yield is probably due to the large size of the system: it suggests that fragmentation occurs in the electronic ground state of the system, after intramolecular vibrational energy redistribution (IVR). We have observed such a phenomenon after VUV and X-ray photoabsorption of deprotonated oligonucleotides as well as protonated peptides and proteins.[66,67,128,135]

Returning to the question we proposed in the introduction, what is the relationship between the fragmentation pattern and the initial photoabsorption site on DNA? Our results show that no new ion channel is observed as the energy increases from the C K-edge energy to the P K-edge energy, indicating that no matter which atom absorbs the photon energy (carbon or

phosphorus), the energy tends to be transferred to the same bonds, causing the same bonds to break and thus fragmentation. On the other hand, although the ion channels remain the same, the abundance of each ion channel differs when the initial photoabsorption site changes. For example, a fragment due to backbone bond cleavage (BB^+) becomes much more abundant at the P K-edge excitation energy. This increase indicates localized fragmentation after site-specific photoabsorption at the phosphorus atoms and thus at the oligonucleotide's backbone. In addition, an increase in the relative abundance of guanine-related ions is also observed around the P K-edge, which can be explained by three possible mechanisms: the first is ionization of the backbone succeeded by hole transfer to the base, the second is electronic excitation of the backbone and the subsequent transfer of this excitation energy to a base followed by ionization of this base, and the third is proton transfer to the base.

In Chapter 5, we have studied the consequences of irradiating the dCGCGGGCCCGCG DNA oligonucleotide with $^{13}C^{3+}$ carbon ions in the gas phase. As already mentioned in the introduction, what are the differences and similarities between ion-induced and photon-induced ionization of DNA? For the same oligonucleotide, we have observed similar NDSED and similarly abundant positive fragment ions after carbon ion impact as in the case of irradiation by X-ray photon irradiation. However, there is no non-dissociative multiple electron detachment after carbon ion impact, which is different from the case of VUV photon absorption.[66] Nevertheless, valence electrons are mostly targeted in both cases. In addition, the NDSED yield after carbon ion impact is much higher than after X-ray photon absorption. This indicates that the NDSED process is most likely due to the emission of valence orbital electrons, which is different from that after photoabsorption.

The final question is how do the hydrogen bonds between the two strands of the double helix DNA affect the fragmentation after irradiation? As we have successfully irradiated the DNA double strands in the gas phase by carbon ion impact for the first time, we observed that although no single strand products dissociated from the double strands are observed, the NDSED products from the DNA double strands are in high abundance, and much higher than that for the single strand DNA. Considering that we used a DNA double strand ion with 7 negative charges, which most probably requires the removal of at least 8 electrons to form a positive ion from the precursor ion, the low probability of this event may explain the sharp increase in the NDSED yield for the $[d(CGCGGGCCCGCG)_2\text{-}7H]^{7-}$ dimer. Meanwhile, the dimer contains 36 H-bonds if it is a double helix (see Section 1.2). The total energy of all the 36 H-bonds is much higher than that of a single covalent bond. This explains how do the

hydrogen bonds between the two strands of the double helix DNA affect the fragmentation after irradiation.

In the future, we plan to perform more experiments for the same DNA dimer after X-ray photoabsorption, in order to compare the difference between carbon ion impact and X-ray photoabsorption. We can also extend the target models to more DNA non-covalent structures such as i-motif and G-quadruplex. The timescale of the processes after carbon ion impact and X-ray photoabsorption is also worth investigating. Such studies will help us to understand more about the intrinsic mechanism of radiation therapy.

7 Appendix: UV-VUV Photofragmentation Spectroscopy of Isolated Neutral Fragile Macromolecules

7.1 Introduction

UV spectroscopy is one of the most widely used techniques in analytical chemistry, especially for measuring the absorption of molecules in solution. The obtained spectra are crucial for identifying whole molecules or chemical groups within a larger system. UV spectroscopy also allows probing the electronic structure of molecular systems, which is useful to understand and predict the consequences of light-molecule interaction, as well as the reactivity of these systems. However, solution-phase spectra suffer from the dependence towards the solvent, and the difficulty in controlling the stoichiometry of noncovalent complexes, which are key issues in many fields of chemistry and biology, including host-guest chemistry, molecular recognition, drug screening, sensors, etc. UV spectroscopy of molecular systems in the gas phase is an alternative approach that probes the intrinsic molecular properties, which can directly be modelled by state-of-the-art calculations.[149]

One major advantage of studying isolated molecular systems is the ability to extend the spectral range to the short wavelengths, *i.e.* in the VUV or even soft X-ray regions, increasing the amount of information obtained, by allowing electrons from inner-valence and even core orbitals to be excited or ejected from the molecule. Such investigations have benefited, in the last decades, from the advent of high-flux and tunable sources of ionizing photons such as synchrotrons, triggering a wealth of studies on small neutral systems.[150–152] However, they all rely on detecting the product ions coming from ionization of the target neutral molecular system, which is not always possible with UV light. Therefore, several experimental techniques have been applied to the measurement of the absorption of neutral molecular systems without ionizing them, notably cavity ring-down spectroscopy.[153] Nevertheless, in all these studies, the size of the molecule is limited, because the vaporization techniques used most often involve thermal heating, which induces chemical reactivity for relatively large thermolabile and floppy molecules. Notably, regarding biologically-relevant molecules,[154–156] a trade-off between thermal decomposition and signal intensity exists.[57,157] The use of aerosol thermodesorption may allow a slight extension of the size range of neutral studies but with limited target densities.[158–160]

An alternative consists in taking advantage of the soft ion sources such as electrospray ionization (ESI) or matrix-assisted laser desorption ionization (MALDI): they have allowed action spectra of molecular ions to be measured in the UV, VUV or soft X-ray ranges, notably of biologically-relevant systems,[109] in particular proteins[106,118,161] but also peptides,[120,127,162–164] carbohydrates[165] and DNA strands.[94,121] In action spectroscopy, the mass spectrum of ionic products from photoabsorption is usually recorded as a function of photon energy. A great advantage of action spectroscopy as compared to direct absorption lies, in certain cases, in its very high sensitivity as a zero-background technique. However, very often, the action spectrum of an isolated molecular system depends on charge state: for instance, the number of protons in a protonated molecule usually changes its fragmentation yield and channels, because proton transfer can lead to bond cleavage, for instance in protonated peptides.[166] Increasing the charge state has also an effect on the geometrical structure of the system, it often induces unfolding of proteins for instance, and can thus influence reactivity (notably charge transfer).[161,167] These undesired effects can be circumvented by studying the neutral molecule and record its photofragmentation yield as a function of photon energy. But then one is facing the issues of bringing intact fragile neutral molecules into the gas phase. In this context, we propose here the following strategy: in order to detect, by mass spectrometry, the fragment ions from photofragmentation of a given neutral molecule, the latter can be noncovalently bound to an ion acting as a charged tag: such a noncovalent complex can be brought intact into the gas phase by ESI or MALDI for instance. Several conditions must be fulfilled in order to obtain the photofragmentation spectrum of the neutral molecule:

1. The yield of product ions formed after photoabsorption by the tag ion is negligible compared to that of the neutral molecule in the photon energy range considered,
2. The noncovalent interactions between the tag ion and the neutral molecule do not strongly modify the electronic states of the latter.

Condition 1 might be fulfilled in the UV-VUV range by using singly-charged negative ions as tags: indeed, their electron photodetachment energy is very low (on the order of a few eV, for instance 2.15±0.15 eV for deprotonated phenol and 2.31±0.15 eV for deprotonated indole)[168], so they are expected to mainly create *neutrals* after photoabsorption at higher photon energy, which are not detected by mass spectrometry. Therefore, these events will not pollute the photofragmentation spectrum of the neutral molecule. Note that in the high energy VUV range, two electrons will possibly be ejected from the tag anion, leading to the formation of a monocation: however, it is not expected to dominate below 14 eV, in the photon energy range

studied here. Besides, electron detachment is known to be a process occurring before inter- and intramolecular vibrational energy redistribution (IVR), thus noncovalent binding with a large molecule would not quench it.[106] However, electronic excitation without electron detachment might still happen, and must be quantified in the singly-charged negative tag ion. Positive tag ions are not expected to be a good choice, because their photoabsorption can trigger ionization and/or fragmentation of the complex, and thus positive ions that may pollute the spectrum of the neutral molecule. Condition 2 must be checked case-by-case by considering the type of noncovalent interactions existing in the complex and the photon energy range probed.

In this article, we report the proof-of-principle that the UV-VUV photofragmentation spectrum of an isolated fragile neutral macromolecule can be obtained by action spectroscopy of its noncovalent complex with a small anion. We use synchrotron radiation as a source of photons, irradiate the anionic complexes in an ion trap, and detect photoabsorption thanks to mass spectrometry analysis of the produced anionic fragments. As a test-case, we choose the noncovalent complex between vancomycin (denoted V) and the deprotonated $Ac_2{}^{L}K{}^{D}A{}^{D}A$ peptide (denoted R). Vancomycin is a last-resort antibiotic against infections caused by Gram-positive bacteria: it specifically recognizes a precursor of the main constituent of the bacterial cell wall, preventing its renewal and leading to cell death. Previous studies have established that the peptidic C-terminal ${}^{D}A{}^{D}A$ sequence is mandatory for high affinity between vancomycin and the receptor.[169] The noncovalent interactions responsible for this behavior have been revealed by structural investigation of the crystallized V+R complex by X-ray diffraction,[170] and they are depicted in Figure 7.1. Five H-bonds link the two peptidic moieties, three of them with ionic character since they involve the CO_2^- group of $[R\text{-}H]^-$. By means of infra-red multiphoton dissociation (IRMPD) spectroscopy, this biologically-active structure has been found to be conserved for deprotonated V+R complexes in the gas phase,[171] but not for the doubly-protonated complex,[172] in line with early low-energy collision-induced dissociation experiments.[173] Indeed, in the protonated complex, R is neutral and the native H-bonding network is lost, thus noncovalent binding is not specific anymore.[172] The advantages of the $[V+R\text{-}H]^-$ complex as a test-case for this study are the following:

1. The 3D geometrical structure of the complex in the gas and condensed phases is known, establishing that vancomycin is neutral and R is deprotonated in the complex. Moreover, the noncovalent interactions do not involve the aromatic chromophores of vancomycin, namely modified side-chains of the amino acid tyrosine, indicating that condition 2 above is fulfilled.

2. R does not contain any aromatic UV chromophore, and it is relatively small compared to vancomycin, we thus expect its absorption cross-section to be lower than that of vancomycin (condition 1 above), with little contribution in the UV range.

3. Photoabsorption of $[V\text{-}2H]^{2-}$ as well as of the $[V+R\text{-}2H]^{2-}$ complex in the gas phase has been studied previously, notably with synchrotron radiation in a complementary VUV range of higher energy.[174] Thus, the reported fragmentation channels will provide a basis for our present investigation.

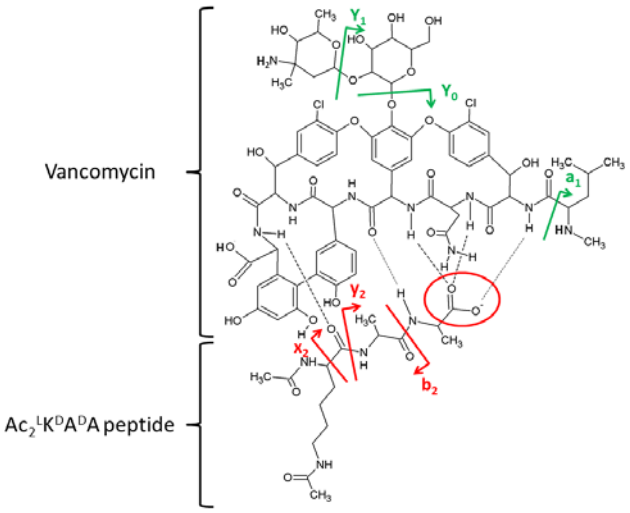

Figure 7.1: Chemical structure of vancomycin ($C_{66}H_{75}Cl_2N_9O_{24}$, average mass 1449.3 amu) bound to the $Ac_2{}^LK^DA^DA$ peptide that mimics the receptor. The standard nomenclature is used for the peptide backbone as well as for oligosaccharide fragmentation, and hence for the main fragments observed after photoabsorption. Arrows indicate on which side of the cleaved bond the charge is located.

7.2 Experimental details

Vancomycin hydrochloride and $Ac_2{}^LK^DA^DA$ have been purchased from Sigma-Aldrich as powders of over 80 % purity, and used without further purification. Electrospray solutions have been prepared in 50:50 (volume ratio) water/methanol at 50 µM concentration with 1 % of ammonia to deprotonate the molecules. For the experiments conducted with a UV-visible spectrophotometer, the concentration of the solution sample was 6.7 µM in deionized water. The UV-visible spectroscopy experiments in solution phase were conducted at CIMAP using a Varian Cary 300 spectrophotometer in the 190-900-nm range, with a 1 nm step. The solution was located in a quartz cell with an optical path of 10 mm. The blank solution was made of deionized water, and the “blank spectrum” was subtracted from the spectrum of vancomycin in deionized water.

The UV-VUV gas phase tandem mass spectrometry experiments were performed using a commercial mass spectrometer (Thermo Finnigan LTQ XL) coupled to the DESIRS beamline

at the SOLEIL synchrotron radiation facility.[175] The set-up has previously been described in detail,[176] only a brief description is given here. The molecular ions were put in the gas phase from the solution by electrospray ionization using a syringe pump with a flow rate of about 5 µL/min and a needle biased at 5 kV in front of a capillary held at 35 V. Ions were then guided through a quadrupole and an octopole, before being injected, thermalized by helium buffer gas and trapped in a commercial linear triple quadrupole ion trap. In this trap, the ions of interest were selected by mass-to-charge ratio (*m/z*) with an isolation width of 6 – 10 depending on the ion; for example, for deprotonated vancomycin (*m/z* 1446.42) all ions with *m/z* between 1443.42 and 1449.42 were trapped, in order to obtain the main isotopic pattern. After isolation, the ions were irradiated by photons from the DESIRS VUV beamline of the SOLEIL synchrotron facility in Saint-Aubin (France).[175] Product anions from photoabsorption as well as remaining precursors were then analyzed with respect to *m/z* in the ion trap, and these mass spectra were accumulated until sufficient statistics was reached (typically 30 spectra).

Mass spectra were recorded for different photon energies, using 0.2 eV steps between 4.5 and 7.5 eV and between 7.2 and 13.8 eV. The UV/VUV beam was free of high harmonics owing to the use of a Kr gas filter (7.2 – 13.8 eV) and a quartz window (4.5 – 7.5 eV). The photon flux was in the 10^{12} – 10^{13} photons/s range and was measured independently using an AXUV100 photodiode (International Radiation Detectors) under the measurement conditions. The total number of photons for a given ion and energy was tuned to obtain a maximum of 10% conversion of the precursor ions to photoproducts, in order to limit the occurrence of sequential two-photon processes. It was regulated by adjusting the exit slit (100 – 600 µm) of the monochromator and a mechanical shutter that controlled the irradiation time of the trapped ions between 200 and 1000 ms.

Results were obtained in the form of one mass spectrum for each photon energy. To quantify the formation of photoproducts as a function of photon energy, action spectra were constructed. These spectra show the yield of each photoproduct as a function of photon energy. This yield has been calculated from the intensity of the peaks in the mass spectra, corrected for the number of incident photons (to account for photon flux variations upon scanning) and for the precursor ion intensity (to account for fluctuations of the number of precursor ions in the ion trap). The yield of photoproduct A can thus be calculated for a given photon energy according to the following:

$$I_{A(rel)} = \frac{I_A}{I_{pre} \cdot N_{phot}}$$

where I_A is the abundance of photoproduct A, measured by the sum of the peak intensities of all isotopes. I_{pre} is the abundance of the precursor ion peak (sum of all isotopes). The incident number of photons N_{phot} is given by:

$$N_{phot} = \Phi_q \cdot \Delta t \cdot \frac{w_{exp}}{w_{ref}}$$

where Φ_q is the photon flux measured in the reference scan with the photodiode, Δt is the irradiation time, w_{exp} is the slit width during the experiment, and w_{ref} is the slit width during the reference scan.

7.3 Results and discussion

First, we explain our method to obtain the UV-VUV photofragmentation spectra and demonstrate that in this photon energy range, the probability of fragmentation following photoabsorption of the deprotonated R peptide ($[R\text{-}H]^-$) is negligible compared to that of deprotonated vancomycin ($[V\text{-}H]^-$). In Figure 7.2, the mass spectra of these two anions after single photon absorption at 6.5 eV are shown: the peaks observed can only be due to photofragmentation, not to photodetachment of one electron, because the latter process creates a neutral that is not detected with the present mass spectrometer. For $[R\text{-}H]^-$, the most intense fragment is detected at *m/z* 223, which we attribute to cleavage of the peptidic backbone to give the $[b_2\text{-}H]^-$ fragment of *m/z* 282, together with loss of CH_3CONH_2 from either the N terminal or the lysine side-chain, after H transfer from the fragment. We also observe loss of one as well as two CH_3CO radicals from the precursor, but also backbone cleavage leading to the $[y_2\text{-}H]^-$ fragment ion, as minor channels. Backbone cleavage and loss of neutrals are very common in photofragmentation[177] or collision-induced dissociation (CID) of deprotonated peptides.[178] Loss of radicals are less common, although Brunet *et al.*[177] reported loss of radical tryptophan and tyrosine side-chains from deprotonated peptides upon photoabsorption in the same photon energy range as the one studied here. The most abundant process detected after photoabsorption by $[V\text{-}H]^-$ is loss of CO_2, which has already been reported for mass spectrometry activation techniques such as CID,[173] surface-induced dissociation (SID)[179] and IRMPD,[171] where fragmentation occurs in the electronic ground state of the system. This channel is also common in organic molecules containing a deprotonated carboxyl group, which is an indication of the deprotonation site of vancomycin. HCl can also be lost in addition to CO_2, but to a much lower extent. Other minor channels are loss of H_2O and H_2O+CO_2.

We plot the photofragmentation yield of the main channels for $[V\text{-}H]^-$ and $[R\text{-}H]^-$ as a function of photon energy in Figure 7.2, in the UV-VUV range 4.5 – 13.8 eV. One can see that for both molecules, the fragmentation yield is much higher in the low photon energy region, which might be explained by a higher absorption cross-section in this region and/or the increase of electron detachment cross-section with photon energy. The spectrum for $[R\text{-}H]^-$ features a maximum around 6.3 eV (~ 197 nm), which is consistent with the peak observed around 6 eV in the action spectra reported for $[WVVVV\text{-}H]^-$ and [YVVVV-H] deprotonated peptides.[177] Electronic π-π* transitions involving the peptide backbone have been predicted around this energy by *ab initio* quantum chemical calculations on peptides.[180] In the case of $[V\text{-}H]^-$, the peak is broadened towards low photon energy, and the fragmentation yield is still high at 4.5 eV. This is due to the presence of five aromatic rings coming from modified tyrosine side-chains (*cf.* Figure 7.1): indeed, tyrosine strongly absorbs light around 275 nm (4.5 eV) in the gas phase, due to π-π* transitions located in the phenol moiety.[106] Note that these rings also contribute to absorption at higher photon energy, since phenol has excited states with very high oscillator strength around 6.8 eV, and also Rydberg states at even higher energy but with lower oscillator strength,[181] the latter probably being responsible for the still high level of CO_2 losses well above 6 eV in Figure 7.2. The crucial conclusions here are: first, in the whole photon energy range, the probability of photoexcitation leading to fragmentation of $[R\text{-}H]^-$ is clearly negligible compared to that of $[V\text{-}H]^-$ (by about two orders of magnitude), and second, the fragmentation signal of these singly-charged species becomes much lower for photon energies over 7 eV, notably due to the increasing yield of electron photodetachment processes as compared to photofragmentation, as we will demonstrate in the next paragraph.

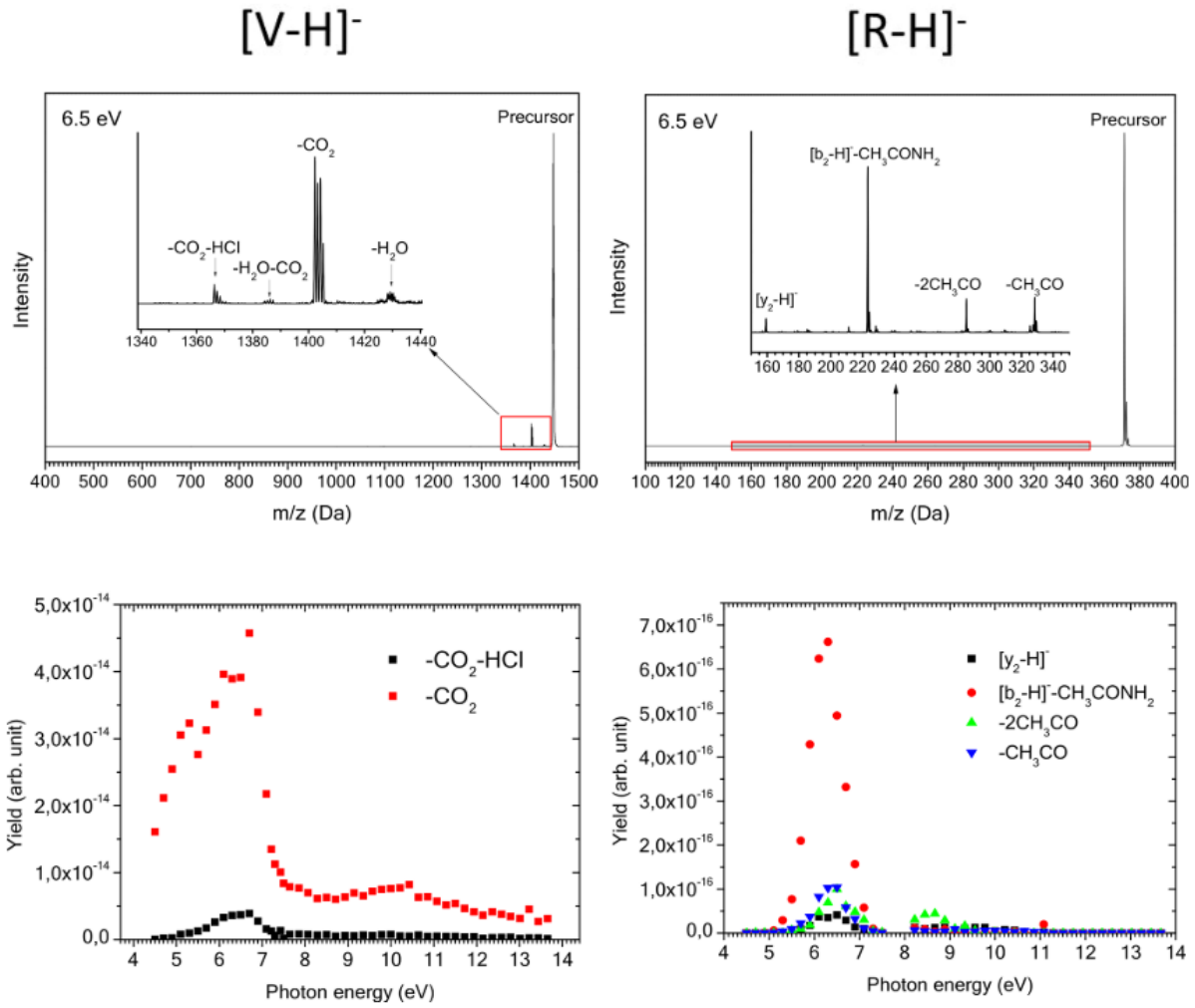

Figure 7.2: Mass spectra after single photon absorption at 6.5 eV (top) and partial fragmentation yields in the UV-VUV range 4.5 – 13.8 eV (bottom) of $[V-H]^-$ (left) and $[R-H]^-$ (right), for the main fragmentation channels observed (for $[R-H]^-$, the lack of data between 7.6 and 8.2 eV is due to a technical problem). The arbitrary units for the yields are the same for both $[V-H]^-$ and $[R-H]^-$, the yields can thus be directly compared.

Second, we confirm that charge state influences the UV-VUV spectrum of deprotonated vancomycin, and we present the electron detachment-related processes. In Figure 7.3, the mass spectrum of $[V-2H]^{2-}$ after absorption of a single 6.5 eV photon is depicted: loss of CO_2 from the precursor anion is a major channel (and much weaker subsequent loss of $2H_2O$ is also present), like for $[V-H]^-$, but here loss of CO_2 is also abundant from the radical anion $[V-2H]^-$ formed as a consequence of single electron photodetachment. We have already observed the latter process from the same molecular system after single-photon absorption at 16 eV,[174] as well as formation of the Y_1^- fragment after glycosidic bond cleavage, which is also detected in the present lower-energy range, but as a minor process. Other low-intensity peaks are attributed to non-dissociative electron detachment and subsequent peptidic backbone cleavage leading to loss of the a_1 fragment. In Figure 7.3, we show the evolution of the yield of channels associated with loss of CO_2 as a function of photon energy in the 4.5 – 11.2 eV range. Although the yield

of CO_2 loss is dominant in the low photon-energy region, its evolution looks different from the case of $[V\text{-}H]^-$: there is only one maximum around 6.2 eV, the shoulder around 5.2 eV is almost vanishing. This shows that charge state has an effect on the UV-VUV excitation spectra of gas-phase vancomycin. CO_2 loss associated with electron detachment has lower yield between 4.5 and 9 eV, but progressively increases from 8 eV and dominates at high photon energy (see Figure 7.3). This is consistent with our previous mass spectrum at 16 eV photon energy,[174] and confirms our hypothesis of photodetachment quenching the photofragmentation of singly-deprotonated vancomycin at high photon energy (see previous paragraph). At low photon energy, the yield of $[V\text{-}2H\text{-}CO_2]^-$ shows a maximum at 6.6 eV, and then falls with the same yield as CO_2 loss from the precursor. It is unusual for the yield of electron detachment-related processes to show a peak falling to almost zero in this low photon energy range, since the cross-section for ejection of one valence electron usually rises monotonically with photon energy from the detachment threshold energy, as electrons from deeper valence orbitals can be involved in the photodetachment process. Therefore the peaked shape of the CO_2 loss associated to photodetachment might be the signature of photo-induced resonant transitions to electronic states of $[V\text{-}2H]^{2-}$ followed by CO_2 loss and subsequent delayed electron detachment. Such an assumption is supported by the fact that the peaks for the yield of both CO_2 loss without and with electron detachment are observed in the same photon energy range (5 – 7 eV). Delayed electron detachment has only been reported once, in the doubly deprotonated peptide gramicidin, by photoelectron spectroscopy.[182] Furthermore, this process most probably occurs after internal conversion to the ground state of the radical anion, because it is associated with CO_2 loss, the main fragmentation channel of $[V\text{-}H]^-$ and $[V\text{-}2H]^{2-}$ after UV photofragmentation but also CID at low collision energy.

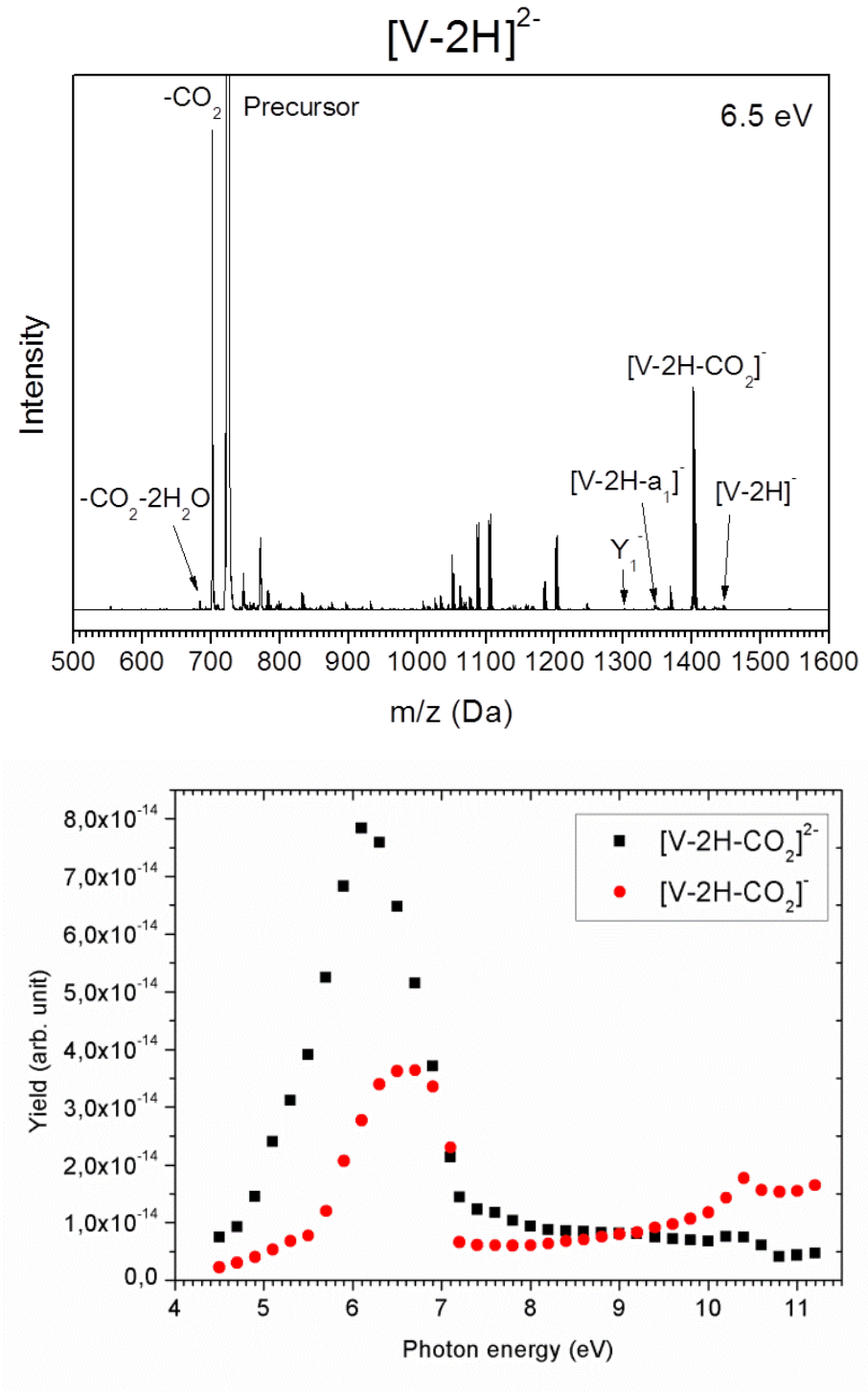

Figure 7.3: Top: mass spectrum of $[V\text{-}2H]^{2-}$ after single photon absorption at 6.5 eV. The unassigned peaks are unaffected by the photon beam. Bottom: partial fragmentation yields of $[V\text{-}2H]^{2-}$ in the UV-VUV 4.5 – 11.2 eV range for the main fragmentation channels observed.

In order to show that the UV-VUV spectrum of neutral vancomycin can be obtained by recording, as a function of photon energy, the photofragmentation of the $[V+R\text{-}H]^-$ noncovalent complex between neutral vancomycin and the deprotonated Ac_2KAA receptor, we have to investigate the mass spectra of $[V+R\text{-}H]^-$ after photoabsorption. In Figure 7.4, the mass spectra of $[V+R\text{-}H]^-$ at 6.5 and 12 eV photon energies are visible and appear to be strongly different.

After absorption of a single photon of 6.5 eV, the mass spectrum is dominated by loss of neutral molecules from the precursor (H_2O, HCl and CO_2), which implies covalent bond cleavage (and rearrangement for HCl and H_2O, see Fig. 1) without breaking of the H bonds linking the complex. This process is highly unusual for closed-shell noncovalent complexes, in contrast to the case of radicals: indeed, we have already observed CO_2 loss from $[V+R-2H]^-$ after electron photodetachment from $[V+R-2H]^{2-}$ in the 16 – 24 eV range.[174] Loss of H_2O, HCl and CO_2 has also been observed from deprotonated vancomycin (see Figure 7.2), whereas CH_3CO loss occurs from $[R-H]^-$ (*cf.* Figure 7.2), which strongly indicates that H_2O, HCl and CO_2 are lost from neutral vancomycin in the $[V+R-H]^-$ complex. These losses are much less abundant after photoabsorption at 12 eV, while $[V-H-CO_2]^-$ is the most abundant species, like in other activation techniques such as CID,[173] SID[179] and IRMPD[171] where it is formed in the electronic ground state of the system. This is somehow surprising, since we would expect $[V-H-CO_2]^-$ to dominate at low photon energy after internal conversion. This behavior indicates a key role played by excited electronic states of vancomycin in the loss of neutral molecules observed at low photon energy. On the contrary, observing $[V-H-CO_2]^-$ at 12 eV photon energy implies dissociation of the complex, and thus substantial redistribution of the available energy into the vibrational modes of the system, in line with dissociation occurring in the electronic ground state, as in CID, SID and IRMPD.

Moreover, we know from previous studies (see the introduction) that vancomycin is initially neutral in the $[V+R-H]^-$ noncovalent complex, thus the negative charge of $[V-H-CO_2]^-$ means that intermolecular charge transfer has been triggered upon photoabsorption. $[V-H-CO_2]^-$ can be formed by proton transfer from neutral vancomycin to $[R-H]^-$, followed by CO_2 loss, which would imply photoabsorption by vancomycin. $[V-H-CO_2]^-$ may also come from electron transfer from $[R-H]^-$ to vancomycin, followed by CO_2H loss, which would mean that the photon has been absorbed by $[R-H]^-$. However, we have shown earlier in this article that the photofragmentation yield of $[R-H]^-$ is negligible compared to that of vancomycin in the whole photon energy range studied here (see Figure 7.2). Therefore, we attribute the formation of $[V-H-CO_2]^-$ to the sole photoexcitation of neutral vancomycin followed by proton transfer to $[R-H]^-$, associated with the formation of $[V-H]^-$ and CO_2 loss. This is supported by the presence of $[V-H]^-$ in the mass spectra of $[V+R-H]^-$ (see Figure 7.4). To our knowledge, proton transfer within a negatively-charged molecular system in the gas phase has never been reported, additional work is thus needed to confirm this interpretation. A reasonable hypothesis for the origin of the proton relies on the observation of massive CO_2 loss from deprotonated

vancomycin in our mass spectra: it is the lowest-energy decay channel of deprotonated vancomycin in its electronic ground state.[171] Vancomycin is deprotonated at the C-terminus of the peptidic moiety, and CO_2 loss occurs from this carboxylate group. Therefore, the proton most probably comes from the carboxyl group of vancomycin. A low-intensity peak present at 6.5 and 12 eV photon energy is observed at *m/z* 1633: from the isotopic pattern, we assign it to bond cleavage in $[R\text{-}H]^-$ to form the x_2 fragment, without dissociation of the complex: we call this species $[x_{2R}+V\text{-}H]^-$. Again, the negligible photofragmentation yield of $[R\text{-}H]^-$ implies photoabsorption in vancomycin followed by energy transfer and fragmentation of $[R\text{-}H]^-$ within the complex. Note that the x_2 fragment has not been observed after photoabsorption by the isolated $[R\text{-}H]^-$, consistent with this mechanism. This is also supported by the crucial fact that none of the fragmentation channels observed for the isolated $[R\text{-}H]^-$ is present for $[V+R\text{-}H]^-$.

Now, let us investigate the evolution of the photofragments from $[V+R\text{-}H]^-$ as a function of photon energy (*cf.* Figure 7.4). The low-energy part is dominated by loss of neutral molecules from the complex, the shape of their peaks being similar to the cases of $[V\text{-}H]^-$ and $[V\text{-}2H]^{2-}$ (*cf.* Figure 7.2 and Figure 7.3). It supports our conclusion that these losses come from vancomycin in the complex (see the previous paragraph). In the high-energy range (9 – 13.8 eV), the most abundant species is $[V\text{-}H\text{-}CO_2]^-$, and from our measurements, we can extract its appearance energy at 8.2±0.4 eV. Its yield smoothly increases up to 12 eV, and then falls. This kind of behavior has been reported for a protonated peptide after photoabsorption in the same energy range,[164] and has been attributed to excitation in high-lying electronic states: we can assume that the same process occurs here. Moreover, electronic transitions over 8 eV have been predicted in peptides, formamide and N-methylacetamide by *ab initio* calculations.[180,183] These transitions are not visible in $[V\text{-}H]^-$ (*cf.* Figure 7.2), probably because they are associated with electron detachment (which does not apply to neutral vancomycin): this is supported by the spectra measured for $[V\text{-}2H]^{2-}$ (see Figure 7.3).

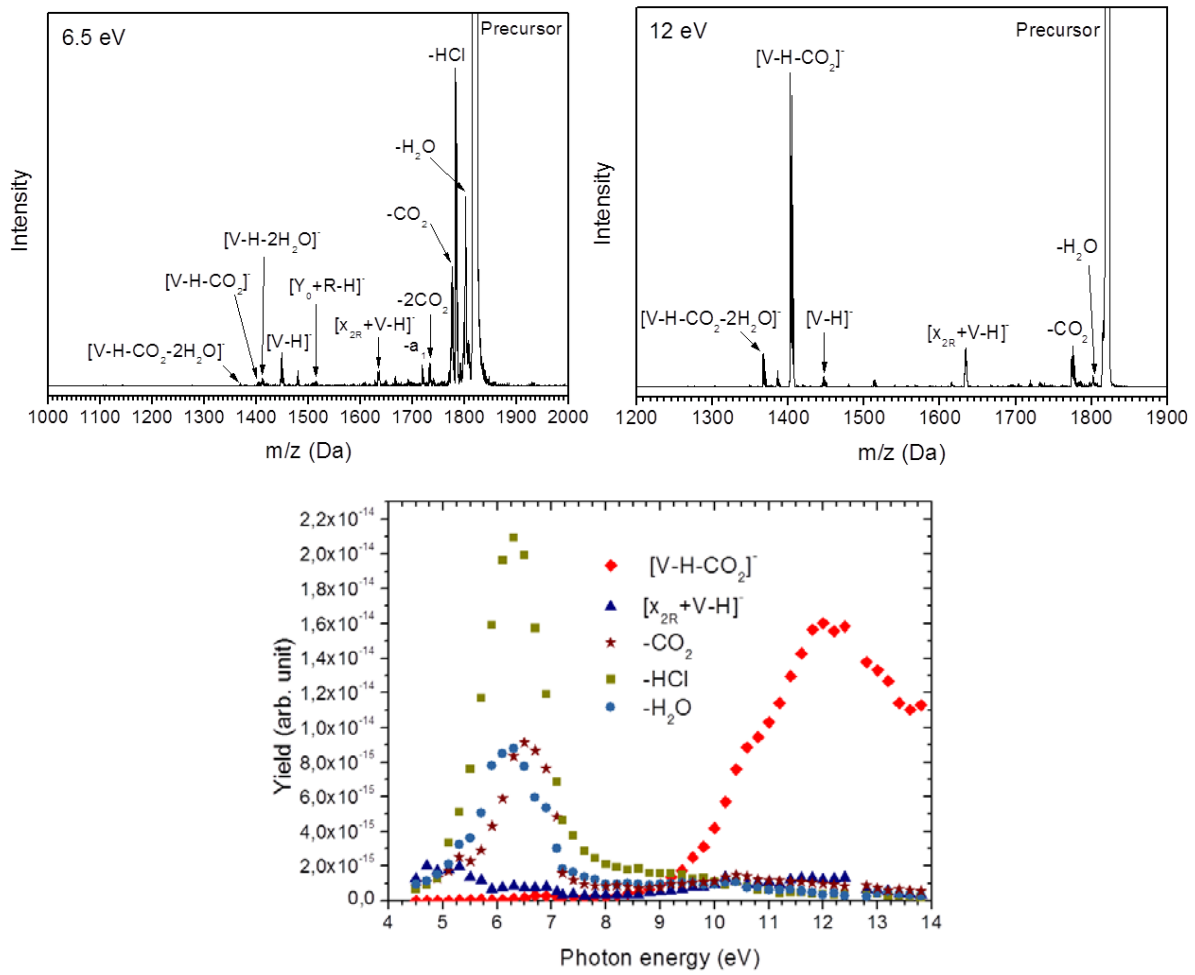

Figure 7.4: Top: mass spectra of [V+R-H]⁻ after single photon absorption at 6.5 eV (left) and 12 eV (right). Bottom: partial fragmentation yields of [V+R-H]⁻ in the UV-VUV 4.5 – 13.8 eV range for the main fragmentation channels observed.

After having commented the main channels after photofragmentation of [V+R-H]⁻ in the 4.5 – 13.8 eV range, we now present in Figure 7.5 the overall UV-VUV photofragmentation spectrum of [V+R-H]⁻, obtained by summing the yield of all fragments. [V+R-H]⁻ is a noncovalent complex composed of neutral vancomycin and [R-H]⁻, and we have shown that in this photon energy range, the photofragmentation probability of [R-H]⁻ is negligible compared to that of vancomycin (see Figure 7.2 and Figure 7.3). Moreover, photoabsorption by vancomycin does not seem to massively induce electron detachment from [R-H]⁻ since we still detect abundant negative ions up to 14 eV (*cf.* Figure 7.4), even if electron detachment dominates for negatively-charged molecules in the high photon energy range (see Figure 7.3). Therefore, the spectrum of Figure 7.5 can be considered as the UV-VUV photofragmentation spectrum of neutral vancomycin, to a first approximation. Strictly speaking, some of the photo-induced electronic transitions within vancomycin are, of course, influenced by the presence of [R-H]⁻, but the H-bonds between the two molecules do not involve the aromatic chromophores

of vancomycin, and these H-bonds are expected to induce only modest shifts in the energy of electronic states relative to the ground state. For instance, for neutral serotonin (an important neurotransmitter), UV-UV hole-burning spectroscopy experiments have shown that the transition from the ground state to the first excited state is red-shifted by only 0.1 eV upon H-bonding to two water molecules (that would induce a shift of about 3 nm at 200 nm).[184] The limited resolution of our measurements made at room temperature makes our spectrum insensitive to such small shifts. One might also argue that the proton transfer process observed here (from neutral vancomycin to $[R\text{-}H]^-$ in the complex) can change the photofragmentation spectrum of neutral vancomycin. However, it is most probably not the case here. Indeed, this proton transfer process occurs in the electronic ground state of the system, and is therefore decoupled from the formation of the excited states of vancomycin. As soon as photoexcitation eventually leads to fragmentation in a hot ground state, which is the case for photons of 8 – 14 eV absorbed by these systems,[174] the VUV action spectrum is unaffected by the subsequent proton transfer. That said, to our knowledge, Figure 7.5 displays the first photofragmentation spectrum of such a large neutral organic molecule in the gas phase. Moreover, the wavelength range extends down to 90 nm, which is unreachable by absorption spectroscopy in solution. An example of such a spectrum is given in Figure 7.5 for vancomycin in aqueous solution: in the 290 – 200 nm region, the absorbance rises, in good agreement with the gas-phase spectrum. The latter allows recording the whole band peaking around 195 nm, in addition to another band with a maximum around 100 nm, attributed to high lying excited states of neutral vancomycin (see previous paragraph).

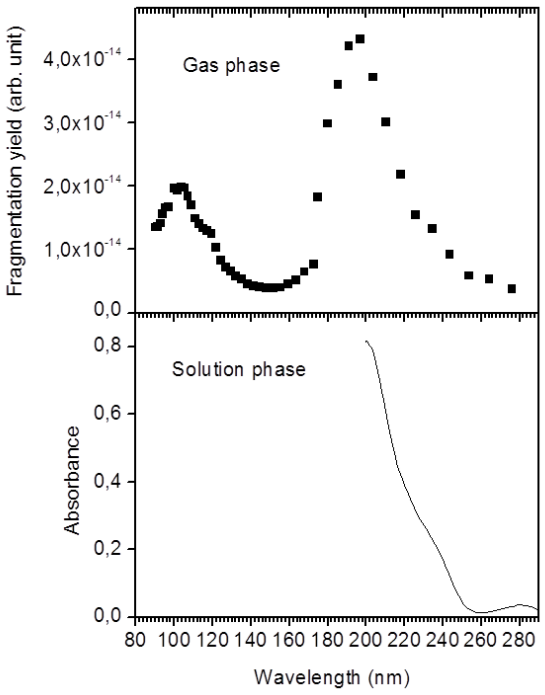

Figure 7.5: Top: total fragmentation yield of isolated $[V+R-H]^-$ in the UV-VUV 4.5 – 13.8 eV range. The yields of all channels have been added and the photon energy has been converted to wavelength. Bottom: UV spectrum of a solution of vancomycin in deionized water.

7.4 Conclusions

In this article, we have presented data from experiments consisting in irradiating trapped gas-phase molecular anions with a synchrotron beam in the UV-VUV range, and recording the mass spectrum of negatively-charged photoproducts as a function of photon energy. By taking advantage of the fact that electrospray ionization is a soft technique that allows bringing fragile noncovalent complexes in the gas phase, we recorded the photofragmentation spectrum of the complex between neutral vancomycin and the singly-deprotonated $Ac_2{}^{L}K^{D}A^{D}A$ peptide. We show that the recorded spectrum can be considered as the UV-VUV photofragmentation spectrum of neutral vancomycin in the gas phase, because in this wavelength range (90 – 275 nm), the probability of photofragmentation of the singly-deprotonated $Ac_2{}^{L}K^{D}A^{D}A$ is negligible compared to that of vancomycin. Furthermore, noncovalent binding does not induce sufficient spectral shifts to have an influence on our spectrum, given the experimental resolution.

This proof-of-principle of charge-tagging action spectroscopy opens up new possibilities regarding UV-VUV spectroscopy of gas-phase neutral organic/biological molecules, thanks to the versatility of the coupling of electrospray ionization and mass spectrometry techniques. The next step is, first, to test our method with other complexes composed of fragile neutral molecules noncovalently bound to small tag anions. Then, it would be worth exploring the soft X-ray energy range, even if electron detachment is expected to be even more dominant over

photofragmentation than in the UV-VUV range. Another perspective takes advantage of the enantiospecific aspect of noncovalent binding of vancomycin to $Ac_2{}^{L}K^{D}A^{D}A$: it has been shown that the ${}^{D}A^{D}A$ termination is required for the receptor to locate in the binding pocket of vancomycin in the condensed phase,[169] in line with the dissociation energy of the doubly-deprotonated complex being much larger for $Ac_2{}^{L}K^{D}A^{D}A$ than for $Ac_2{}^{D}K^{L}A^{L}A$ in the gas phase.[173] Thus, it would be interesting to record the action spectrum of the singly-deprotonated noncovalent complex between vancomycin and $Ac_2{}^{D}K^{L}A^{L}A$ with the same method as applied here: we expect major differences with the results presented here.

References

(1) World Health Organization. *Ionizing radiation and health effects*. https://www.who.int/news-room/fact-sheets/detail/ionizing-radiation-and-health-effects.

(2) Alizadeh, E.; Orlando, T. M.; Sanche, L. Biomolecular Damage Induced by Ionizing Radiation: The Direct and Indirect Effects of Low-Energy Electrons on DNA. *Annu. Rev. Phys. Chem.* **2015**, *66* (1), 379–398. https://doi.org/10.1146/annurev-physchem-040513-103605.

(3) Becquerel, H. Sur Les Radiations Invisible Emises Par Les Corps Phosphorescents. *Comptes rendus* **1896**, *122*, 501–503.

(4) Curie, P.; Sklodowska-Curie, M. Sur Une Substance Nouvelle Radio-Active, Contenue Dans La Pechblende. *CR Acad. Sci. Paris* **1898**, *127*, 175–178.

(5) Curie, P. Sur Une Nouvelle Substance Fortement Radioactive, Contenue Dans La Pechblende. *Comptes rendus 1'Academie des Sci. Paris* **1898**, *127*, 1215–1217.

(6) Becquerel, A. H. On Radioactivity, a New Property of Matter. *Les prix Nobel* **1903**.

(7) Curie, P. Radioactive Substances, Especially Radium. *Nobel Lect.* **1905**.

(8) JOLIOT, F.; CURIE, I. Artificial Production of a New Kind of Radio-Element. *Nature* **1934**, *133* (3354), 201–202. https://doi.org/10.1038/133201a0.

(9) Joliot, F. F. Chemical Evidence of the Transmutation of Elements. *Nobel Lect. December* **1935**, *12*, 1922–1941.

(10) Havas, M. When Theory and Observation Collide: Can Non-Ionizing Radiation Cause Cancer? *Environ. Pollut.* **2017**, *221*, 501–505. https://doi.org/10.1016/j.envpol.2016.10.018.

(11) Mayles, W. P. M.; Nahum, A. E.; Rosenwald, J.-C. *Handbook of Radiotherapy Physics: Theory and Practice, Second Edition, Two Volume Set*, 2nd, illustr ed.; Philip Mayles, Alan E. Nahum, J. C. R., Ed.; CRC Press, 2021.

(12) Wang, J. song; Wang, H. juan; Qian, H. li. Biological Effects of Radiation on Cancer Cells. *Mil. Med. Res.* **2018**, *5* (1), 1–10. https://doi.org/10.1186/s40779-018-0167-4.

(13) Elgazzar, A. H.; Kazem, N. Biological Effects of Ionizing Radiation. In *The Pathophysiologic Basis of Nuclear Medicine*; Elgazzar, A. H., Ed.; Springer Berlin Heidelberg: Berlin, Heidelberg, 2006; pp 540–548. https://doi.org/10.1007/978-3-540-47953-6_23.

(14) Abu Bakar, N. F.; Amira Othman, S.; Amirah Nor Azman, N. F.; Saqinah Jasrin, N. Effect of Ionizing Radiation towards Human Health: A Review. *IOP Conf. Ser. Earth Environ. Sci.* **2019**, *268* (1), 012005. https://doi.org/10.1088/1755-1315/268/1/012005.

(15) Andreassi, M. G. The Biological Effects of Diagnostic Cardiac Imaging on Chronically Exposed Physicians: The Importance of Being Non-Ionizing. *Cardiovasc. Ultrasound* **2004**, *2* (1), 25. https://doi.org/10.1186/1476-7120-2-25.

(16) Jeggo, P. The Role of the DNA Damage Response Mechanisms after Low-Dose Radiation Exposure and a Consideration of Potentially Sensitive Individuals. *Radiat. Res.* **2010**, *174* (6 B), 825–832. https://doi.org/10.1667/RR1844.1.

(17) Duncan, J. R.; Lieber, M. R.; Adachi, N.; Wahl, R. L. Radiation Dose Does Matter: Mechanistic Insights into DNA Damage and Repair Support the Linear No-Threshold Model of Low-Dose Radiation Health Risks. *J. Nucl. Med.* **2018**, *59* (7), 1014–1016. https://doi.org/10.2967/jnumed.118.210252.

(18) Adalja, A. A.; Watson, M.; Wollner, S.; Toner, E. A Possible Approach to Large-Scale Laboratory Testing for Acute Radiation Sickness after a Nuclear Detonation. *Biosecurity and Bioterrorism* **2011**, *9* (4), 345–350. https://doi.org/10.1089/bsp.2011.0042.

(19) ICRP. *The 2007 Recommendations of the International Commission on Radiological*

Protection. ICRP Publication 103.; 2007; Vol. 37. https://doi.org/10.1016/j.icrp.2007.10.003.
(20) Bolus, N. E. Basic Review of Radiation Biology and Terminology. *J. Nucl. Med. Technol.* **2017**, *45* (4), 259–264. https://doi.org/10.2967/jnmt.117.195230.
(21) National Research Council. *Health Risks from Exposure to Low Levels of Ionizing Radiation: BEIR VII Phase 2*; National Academies Press: Washington, DC, 2006.
(22) Beaglehole, R.; Bonita, R.; Magnusson, R. Global Cancer Prevention: An Important Pathway to Global Health and Development. *Public Health* **2011**, *125* (12), 821–831. https://doi.org/10.1016/j.puhe.2011.09.029.
(23) Gaidai, O.; Yan, P.; Xing, Y. Future World Cancer Death Rate Prediction. *Sci. Rep.* **2023**, *13* (1), 303. https://doi.org/10.1038/s41598-023-27547-x.
(24) Despeignes, V. Observation Concernant Un Cas de Cancer de l'estomac Traite Par Les Rayons Rontgen. *Lyon méd.* **1896**, *82*, 428–430.
(25) Bernier, J.; Hall, E. J.; Giaccia, A. Radiation Oncology: A Century of Achievements. *Nat. Rev. Cancer* **2004**, *4* (9), 737–747. https://doi.org/10.1038/nrc1451.
(26) Mould, R. F. *A Century of X-Rays and Radioactivity in Medicine: With Emphasis on Photographic Records of the Early Years*; CRC Press, 1993.
(27) Thariat, J.; Hannoun-Levi, J. M.; Sun Myint, A.; Vuong, T.; Gérard, J. P. Past, Present, and Future of Radiotherapy for the Benefit of Patients. *Nat. Rev. Clin. Oncol.* **2013**, *10* (1), 52–60. https://doi.org/10.1038/nrclinonc.2012.203.
(28) Bragg, W. H.; Kleeman, R. LXXIV. On the Ionization Curves of Radium. *London, Edinburgh, Dublin Philos. Mag. J. Sci.* **1904**, *8* (48), 726–738.
(29) Lagzda, A. VHEE Radiotherapy Studies at CLARA and CLEAR Facilities, The University of Manchester (United Kingdom), 2019.
(30) Yokoi, T.; Cobb, J.; Ken Peach, J. A. I.; Morgan, G.; Pozimski, J.; Easton, M. Beam Injection Issues of FFAG for Particle Therapy. In *Proceedings of EPAC*; 2008; Vol. 8, p 3401.
(31) Miescher, J. F. *Ueber Die Chemische Zusammensetzung Der Eiterzellen*; 1871.
(32) Mendel, G. Versuche Über Plflanzenhybriden (Experiments in Plant Hybridization). *Verhandlungen des naturforschenden Vereines Brünn* **1865**, *4*, 3–47.
(33) Oswald T. Avery; MacLEOD COLIN; MACLYN, M. Studies on the Chemical Nature of the Substance Inducing Transformation of Pneumococcal Types: Induction of Transformation by a Desoxyribonucleic Acid Fraction Isolated from Pneumococcus Type III. *J. Exp. Med.* **1944**, *79* (2), 137–158.
(34) CHARGAFF, E.; LIPSHITZ, R.; GREEN, C.; HODES, M. E. The Composition of the Deoxyribonucleic Acid of Salmon Sperm. *J. Biol. Chem.* **1951**, *192* (1), 223–230. https://doi.org/10.1016/s0021-9258(18)55924-x.
(35) WATSON, J. D.; CRICK, F. H. C. Genetical Implications of the Structure of Deoxyribonucleic Acid. *Nature* **1953**, *171* (4361), 964–967. https://doi.org/10.1038/171964b0.
(36) WATSON, J. D.; CRICK, F. H. C. Molecular Structure of Nucleic Acids: A Structure for Deoxyribose Nucleic Acid. *Nature* **1953**, *171* (4356), 737–738. https://doi.org/10.1038/171737a0.
(37) Watson, J. D.; Crick, F. H. C. THE STRUCTURE OF DNA. *Cold Spring Harb. Symp. Quant. Biol.* **1953**, *18*, 123–131. https://doi.org/10.1101/SQB.1953.018.01.020.
(38) *Deoxyribonucleic Acid (DNA)*. https://www.genome.gov/genetics-glossary/Deoxyribonucleic-Acid.
(39) Sleno, L.; Volmer, D. A. Ion Activation Methods for Tandem Mass Spectrometry. *J. Mass Spectrom.* **2004**, *39* (10), 1091–1112. https://doi.org/10.1002/jms.703.
(40) Schürch, S. Characterization of Nucleic Acids by Tandem Mass Spectrometry - The

Second Decade (2004-2013): From DNA to RNA and Modified Sequences. *Mass Spectrom. Rev.* **2016**, *35* (4), 483–523. https://doi.org/10.1002/mas.21442.

(41) Mcluckey, S. A.; Van Berkel, G. J.; Glish, G. L. Tandem Mass Spectrometry of Small, Multiply Charged Oligonucleotides. *J. Am. Soc. Mass Spectrom.* **1992**, *3* (1), 60–70. https://doi.org/10.1016/1044-0305(92)85019-G.

(42) Michael, B. D.; O'Neill, P. A Sting in the Tail of Electron Tracks. *Science (80-.).* **2000**, *287* (5458), 1603–1604. https://doi.org/10.1126/science.287.5458.1603.

(43) Nguyena, J.; Maa, Y.; Luoa, T.; Bristowb, R. G.; Jaffrayc, D. A.; Lua, Q. Bin. Direct Observation of Ultrafast-Electron-Transfer Reactions Unravels High Effectiveness of Reductive DNA Damage. *Proc. Natl. Acad. Sci. U. S. A.* **2011**, *108* (29), 11778–11783. https://doi.org/10.1073/pnas.1104367108.

(44) Bald, I.; Illenberger, E.; Kopyra, J. Damage of DNA by Low Energy Electrons (< 3 EV). *J. Phys. Conf. Ser.* **2012**, *373*, 012008. https://doi.org/10.1088/1742-6596/373/1/012008.

(45) Chevalier, F.; Schlathölter, T.; Poully, J. Radiation‐Induced Transfer of Charge, Atoms, and Energy within Isolated Biomolecular Systems. *ChemBioChem* **2023**. https://doi.org/10.1002/cbic.202300543.

(46) Hush, N. S.; Cheung, A. S. Ionization Potentials and Donor Properties of Nucleic Acid Bases and Related Compounds. *Chem. Phys. Lett.* **1975**, *34* (1), 11–13. https://doi.org/10.1016/0009-2614(75)80190-4.

(47) SUKHODUB, L. F.; YANSON, I. K. Mass Spectrometric Studies of Binding Energies for Nitrogen Bases of Nucleic Acids in Vacuo. *Nature* **1976**, *264* (5583), 245–247. https://doi.org/10.1038/264245a0.

(48) Nir, E.; Kleinermanns, K.; de Vries, M. S. Pairing of Isolated Nucleic-Acid Bases in the Absence of the DNA Backbone. *Nature* **2000**, *408* (6815), 949–951. https://doi.org/10.1038/35050053.

(49) Kostko, O.; Bravaya, K.; Krylov, A.; Ahmed, M. Ionization of Cytosine Monomer and Dimer Studied by VUV Photoionization and Electronic Structure Calculations. *Phys. Chem. Chem. Phys.* **2010**, *12* (12), 2860–2872. https://doi.org/10.1039/b921498d.

(50) Golan, A.; Bravaya, K. B.; Kudirka, R.; Kostko, O.; Leone, S. R.; Krylov, A. I.; Ahmed, M. Ionization of Dimethyluracil Dimers Leads to Facile Proton Transfer in the Absence of Hydrogen Bonds. *Nat. Chem.* **2012**, *4* (4), 323–329. https://doi.org/10.1038/nchem.1298.

(51) Hartweg, S.; Hochlaf, M.; Garcia, G. A.; Nahon, L. Photoionization Dynamics and Proton Transfer within the Adenine-Thymine Nucleobase Pair. *J. Phys. Chem. Lett.* **2023**, *14* (15), 3698–3705. https://doi.org/10.1021/acs.jpclett.3c00564.

(52) Zappa, F.; Denifl, S.; Mähr, I.; Lecointre, J.; Rondino, F.; Echt, O.; Märk, T. D.; Scheier, P. Electron Impact Ionization of Thymine Clusters Embedded in Superfluid Helium Droplets. *Eur. Phys. J. D* **2007**, *43* (1–3), 117–120. https://doi.org/10.1140/epjd/e2007-00093-9.

(53) Biemann, K.; McCloskey, J. A. Application of Mass Spectrometry to Structure Problems. 1 VI. Nucleosides 2. *J. Am. Chem. Soc.* **1962**, *84* (10), 2005–2007. https://doi.org/10.1021/ja00869a048.

(54) Le Padellec, A.; Moretto-Capelle, P.; Richard-Viard, M.; Champeaux, J. P.; Cafarelli, P. Ionization and Fragmentation of DNA, RNA Bases Induced by Proton Impact. *J. Phys. Conf. Ser.* **2008**, *101* (1). https://doi.org/10.1088/1742-6596/101/1/012007.

(55) Maclot, S.; Delaunay, R.; Piekarski, D. G.; Domaracka, A.; Huber, B. A.; Adoui, L.; Martín, F.; Alcamí, M.; Avaldi, L.; Bolognesi, P.; Díaz-Tendero, S.; Rousseau, P. Determination of Energy-Transfer Distributions in Ionizing Ion-Molecule Collisions. *Phys. Rev. Lett.* **2016**, *117* (7), 073201. https://doi.org/10.1103/PhysRevLett.117.073201.

(56) Levola, H.; Kooser, K.; Itälä, E.; Kukk, E. Comparison of VUV Radiation Induced

Fragmentation of Thymidine and Uridine Nucleosides – The Effect of Methyl and Hydroxyl Groups. *Int. J. Mass Spectrom.* **2014**, *370*, 96–100. https://doi.org/10.1016/j.ijms.2014.07.008.

(57) Levola, H.; Kooser, K.; Rachlew, E.; Nõmmiste, E.; Kukk, E. Fragmentation of Thymidine Induced by Ultraviolet Photoionization and Thermal Degradation. *Int. J. Mass Spectrom.* **2013**, *353*, 7–11. https://doi.org/10.1016/j.ijms.2013.08.008.

(58) Itälä, E.; Huels, M. A.; Rachlew, E.; Kooser, K.; Hägerth, T.; Kukk, E. A Comparative Study of Dissociation of Thymidine Molecules Following Valence or Core Photoionization. *J. Phys. B At. Mol. Opt. Phys.* **2013**, *46* (21), 215102. https://doi.org/10.1088/0953-4075/46/21/215102.

(59) Bocková, J.; Rebelo, A.; Ryszka, M.; Pandey, R.; Mészáros, D.; Limão-Vieira, P.; Papp, P.; Mason, N. J.; Townsend, D.; Nixon, K. L.; Vizcaino, V.; Poully, J.; Eden, S. Thermal Desorption Effects on Fragment Ion Production from Multi-Photon Ionized Uridine and Selected Analogues. *RSC Adv.* **2021**, *11* (34), 20612–20621. https://doi.org/10.1039/d1ra01873f.

(60) Shin, J.-W.; Bernstein, E. R. Vacuum Ultraviolet Photoionization of Carbohydrates and Nucleotides. *J. Chem. Phys.* **2014**, *140* (4), 044330. https://doi.org/10.1063/1.4862829.

(61) Ball, A. T.; Prakash, A. S.; Bristow, A. W. T.; Sims, M.; Mosely, J. A. Characterisation of Phosphorylated Nucleotides by Collisional and Electron - based Tandem Mass Spectrometry. *Rapid Commun. Mass Spectrom.* **2016**, *30* (19), 2155–2163. https://doi.org/10.1002/rcm.7701.

(62) Milosavljević, A. R.; Cerovski, V. Z.; Canon, F.; Ranković, M. L.; Škoro, N.; Nahon, L.; Giuliani, A. Energy-Dependent UV Photodissociation of Gas-Phase Adenosine Monophosphate Nucleotide Ions: The Role of a Single Solvent Molecule. *J. Phys. Chem. Lett.* **2014**, *5* (11), 1994–1999. https://doi.org/10.1021/jz500696b.

(63) Lindner, J.; Grotemeyer, J. Application of Multiphoton Ionization Mass Spectrometry: Protected Dideoxyribonucleotides. *J. Mol. Struct.* **1991**, *249* (1), 81–93. https://doi.org/10.1016/0022-2860(91)85056-9.

(64) González-Magaña, O.; Tiemens, M.; Reitsma, G.; Boschman, L.; Door, M.; Bari, S.; Lahaie, P. O.; Wagner, J. R.; Huels, M. A.; Hoekstra, R.; Schlathölter, T. Fragmentation of Protonated Oligonucleotides by Energetic Photons and C Q+ Ions. *Phys. Rev. A* **2013**, *87* (3), 032702. https://doi.org/10.1103/PhysRevA.87.032702.

(65) Wang, X.; Rathnachalam, S.; Zamudio-Bayer, V.; Bijlsma, K.; Li, W.; Hoekstra, R.; Kubin, M.; Timm, M.; von Issendorff, B.; Lau, J. T.; Faraji, S.; Schlathölter, T. Intramolecular Hydrogen Transfer in DNA Induced by Site-Selective Resonant Core Excitation. *Phys. Chem. Chem. Phys.* **2022**, *24* (13), 7815–7825. https://doi.org/10.1039/D1CP05741C.

(66) Li, W.; Mjekiqi, E.; Douma, W.; Wang, X.; Kavatsyuk, O.; Hoekstra, R.; Poully, J.; Schlathölter, T. Hole Migration in Telomere - Based Oligonucleotide Anions and G - Quadruplexes. *Chem. – A Eur. J.* **2019**, *25* (70), 16114–16119. https://doi.org/10.1002/chem.201904105.

(67) Li, W.; Kavatsyuk, O.; Douma, W.; Wang, X.; Hoekstra, R.; Mayer, D.; Robinson, M. S.; Gühr, M.; Lalande, M.; Abdelmouleh, M.; Ryszka, M.; Poully, J. C.; Schlathölter, T. Multiple Valence Electron Detachment Following Auger Decay of Inner-Shell Vacancies in Gas-Phase DNA. *Chem. Sci.* **2021**, *12* (39), 13177–13186. https://doi.org/10.1039/D1SC02885E.

(68) Paul, W. Electromagnetic Traps for Charged and Neutral Particles. *Rev. Mod. Phys.* **1990**, *62* (3), 531–540. https://doi.org/10.1103/RevModPhys.62.531.

(69) Wang, X. Photon Induced Charge and Structural Dynamics in Gas-Phase DNA, University of Groningen, 2022.

(70) Fenn, J. B.; Mann, M.; Meng, C. K.; Wong, S. F.; Whitehouse, C. M. Electrospray Ionization for Mass Spectrometry of Large Biomolecules. *Science (80-.).* **1989**, *246* (4926), 64–71. https://doi.org/10.1126/science.2675315.
(71) G. Anderson. *About GAA Custom Engineering LLC*. http://www.mstar2k.com/about-us.
(72) Schaffer, S. A.; Tang, K.; Anderson, G. A.; Prior, D. C.; Udseth, H. R.; Smith, R. D. A Novel Ion Funnel for Focusing Ions at Elevated Pressure Using Electrospray Ionization Mass Spectrometry. *Rapid Commun. Mass Spectrom.* **1997**, *11* (16), 1813–1817. https://doi.org/10.1002/(SICI)1097-0231(19971030)11:16<1813::AID-RCM87>3.0.CO;2-D.
(73) Ibrahim, Y. M.; Baker, E. S.; Danielson, W. F.; Norheim, R. V.; Prior, D. C.; Anderson, G. A.; Belov, M. E.; Smith, R. D. Development of a New Ion Mobility Time-of-Flight Mass Spectrometer. *Int. J. Mass Spectrom.* **2015**, *377*, 655–662. https://doi.org/10.1016/j.ijms.2014.07.034.
(74) Mamyrin, B. A.; Karataev, V. I.; Shmikk, D. V.; Zagulin, V. A. The Mass-Reflectron, a New Nonmagnetic Time-of-Flight Mass Spectrometer with High Resolution. *Sov Phys JETP* **1973**, *37* (1), 45–48.
(75) D. Egorov. Photoionization and Excitation Processes in Proteins and Peptide, University of Groningen, 2018.
(76) Douma, W. Radiation Action on Deprotonated DNA in the Gas Phase, University of Groningen, 2018.
(77) Balerna, A.; Mobilio, S. Introduction to Synchrotron Radiation. In *Synchrotron Radiation*; Springer Berlin Heidelberg: Berlin, Heidelberg, 2015; pp 3–28. https://doi.org/10.1007/978-3-642-55315-8_1.
(78) Lightsources.org. *Light sources of the world*. Lightsources.org. https://lightsources.org/lightsources-of-the-world/.
(79) Viefhaus, J.; Scholz, F.; Deinert, S.; Glaser, L.; Ilchen, M.; Seltmann, J.; Walter, P.; Siewert, F. The Variable Polarization XUV Beamline P04 at PETRA III: Optics, Mechanics and Their Performance. *Nucl. Instruments Methods Phys. Res. Sect. A Accel. Spectrometers, Detect. Assoc. Equip.* **2013**, *710*, 151–154. https://doi.org/10.1016/j.nima.2012.10.110.
(80) Grunder, H. A.; Selph, F. B. Heavy-Ion Accelerators. *Annu. Rev. Nucl. Sci.* **1977**, *27* (1), 353–392. https://doi.org/10.1146/annurev.ns.27.120177.002033.
(81) Meier, F.; Brunner, A. D.; Koch, S.; Koch, H.; Lubeck, M.; Krause, M.; Goedecke, N.; Decker, J.; Kosinski, T.; Park, M. A.; Bache, N.; Hoerning, O.; Cox, J.; Räther, O.; Mann, M. Online Parallel Accumulation–Serial Fragmentation (PASEF) with a Novel Trapped Ion Mobility Mass Spectrometer. *Mol. Cell. Proteomics* **2018**, *17* (12), 2534–2545. https://doi.org/10.1074/mcp.TIR118.000900.
(82) Silveira, J. A.; Ridgeway, M. E.; Laukien, F. H.; Mann, M.; Park, M. A. Parallel Accumulation for 100% Duty Cycle Trapped Ion Mobility-Mass Spectrometry. *Int. J. Mass Spectrom.* **2017**, *413*, 168–175. https://doi.org/10.1016/j.ijms.2016.03.004.
(83) Meier, F.; Beck, S.; Grassl, N.; Lubeck, M.; Park, M. A.; Raether, O.; Mann, M. Parallel Accumulation-Serial Fragmentation (PASEF): Multiplying Sequencing Speed and Sensitivity by Synchronized Scans in a Trapped Ion Mobility Device. *J. Proteome Res.* **2015**, *14* (12), 5378–5387. https://doi.org/10.1021/acs.jproteome.5b00932.
(84) Ridgeway, M. E.; Lubeck, M.; Jordens, J.; Mann, M.; Park, M. A. Trapped Ion Mobility Spectrometry: A Short Review. *Int. J. Mass Spectrom.* **2018**, *425*, 22–35. https://doi.org/10.1016/j.ijms.2018.01.006.
(85) Mason, E. A.; McDaniel, E. W. *Transport Properties of Ions in Gases*; Wiley, 1988. https://doi.org/10.1002/3527602852.
(86) Bohrer, B. C.; Merenbloom, S. I.; Koeniger, S. L.; Hilderbrand, A. E.; Clemmer, D. E.

Biomolecule Analysis by Ion Mobility Spectrometry. *Annu. Rev. Anal. Chem.* **2008**, *1* (1), 293–327. https://doi.org/10.1146/annurev.anchem.1.031207.113001.

(87) Wyttenbach, T.; Bowers, M. T. Gas-Phase Conformations: The Ion Mobility/Ion Chromatography Method. In *Modern Mass Spectrometry*; 2003; pp 207–232. https://doi.org/10.1007/3-540-36113-8_6.

(88) Kanu, A. B.; Dwivedi, P.; Tam, M.; Matz, L.; Hill, H. H. Ion Mobility-Mass Spectrometry. *J. Mass Spectrom.* **2008**, *43* (1), 1–22. https://doi.org/10.1002/jms.1383.

(89) Revercomb, H. E.; Mason, E. A. Theory of Plasma Chromatography/Gaseous Electrophoresis. A Review. *Anal. Chem.* **1975**, *47* (7), 970–983. https://doi.org/10.1021/ac60357a043.

(90) Rosu, F.; Pirotte, S.; Pauw, E. De; Gabelica, V. Positive and Negative Ion Mode ESI-MS and MS/MS for Studying Drug–DNA Complexes. *Int. J. Mass Spectrom.* **2006**, *253* (3), 156–171. https://doi.org/10.1016/j.ijms.2005.11.027.

(91) Gabelica, V.; Tabarin, T.; Antoine, R.; Rosu, F.; Compagnon, I.; Broyer, M.; De Pauw, E.; Dugourd, P. Electron Photodetachment Dissociation of DNA Polyanions in a Quadrupole Ion Trap Mass Spectrometer. *Anal. Chem.* **2006**, *78* (18), 6564–6572. https://doi.org/10.1021/ac060753p.

(92) Rosu, F.; Nguyen, C. H.; De Pauw, E.; Gabelica, V. Ligand Binding Mode to Duplex and Triplex DNA Assessed by Combining Electrospray Tandem Mass Spectrometry and Molecular Modeling. *J. Am. Soc. Mass Spectrom.* **2007**, *18* (6), 1052–1062. https://doi.org/10.1016/j.jasms.2007.03.010.

(93) Rosu, F.; Gabelica, V.; De Pauw, E.; Mailliet, P.; Mergny, J. L. Cooperative 2:1 Binding of a Bisphenothiazine to Duplex DNA. *ChemBioChem* **2008**, *9* (6), 849–852. https://doi.org/10.1002/cbic.200700572.

(94) Rosu, F.; Gabelica, V.; De Pauw, E.; Antoine, R.; Broyer, M.; Dugourd, P. UV Spectroscopy of DNA Duplex and Quadruplex Structures in the Gas Phase. *J. Phys. Chem. A* **2012**, *116* (22), 5383–5391. https://doi.org/10.1021/jp302468x.

(95) Burmistrova, A.; Gabelica, V.; Duwez, A. S.; De Pauw, E. Ion Mobility Spectrometry Reveals Duplex DNA Dissociation Intermediates. *J. Am. Soc. Mass Spectrom.* **2013**, *24* (11), 1777–1786. https://doi.org/10.1007/s13361-013-0721-y.

(96) Gabelica, V.; De Pauw, E. Comparison of the Collision-Induced Dissociation of Duplex DNA at Different Collision Regimes: Evidence for a Multistep Dissociation Mechanism. *J. Am. Soc. Mass Spectrom.* **2002**, *13* (1), 91–98. https://doi.org/10.1016/S1044-0305(01)00335-X.

(97) Bishop, G. R.; Chaires, J. B. Characterization of DNA Structures by Circular Dichroism. *Curr. Protoc. Nucleic Acid Chem.* **2002**, 7.11.1-7.11.8. https://doi.org/10.1002/0471142700.nc0711s11.

(98) Vorlíčková, M.; Kejnovská, I.; Bednářová, K.; Renčiuk, D.; Kypr, J. Circular Dichroism Spectroscopy of DNA: From Duplexes to Quadruplexes. *Chirality* **2012**, *24* (9), 691–698. https://doi.org/10.1016/0076-6879(92)11021-A.

(99) Gray, D. M.; Ratliff, R. L.; Vaughan, M. R. Circular Dichroism Spectroscopy of DNA. *Methods Enzymol.* **1992**, *211* (C), 389–406. https://doi.org/10.1016/0076-6879(92)11021-A.

(100) Meija, J.; Coplen, T. B.; Berglund, M.; Brand, W. A.; De Bièvre, P.; Gröning, M.; Holden, N. E.; Irrgeher, J.; Loss, R. D.; Walczyk, T.; Prohaska, T. Isotopic Compositions of the Elements 2013 (IUPAC Technical Report). *Pure Appl. Chem.* **2016**, *88* (3), 293–306. https://doi.org/10.1515/pac-2015-0503.

(101) Porrini, M.; Rosu, F.; Rabin, C.; Darré, L.; Gómez, H.; Orozco, M.; Gabelica, V. Compaction of Duplex Nucleic Acids upon Native Electrospray Mass Spectrometry. *ACS Cent. Sci.* **2017**, *3* (5), 454–461. https://doi.org/10.1021/acscentsci.7b00084.

(102) Bush, M. F.; Hall, Z.; Giles, K.; Hoyes, J.; Robinson, C. V.; Ruotolo, B. T. Collision Cross Sections of Proteins and Their Complexes: A Calibration Framework and Database for Gas-Phase Structural Biology. *Anal. Chem.* **2010**, *82* (22), 9557–9565. https://doi.org/10.1021/ac1022953.
(103) Lalande, M.; Comby-Zerbino, C.; Bouakil, M.; Dugourd, P.; Chirot, F.; Poully, J. C. Isolated Collagen Mimetic Peptide Assemblies Have Stable Triple-Helix Structures. *Chem. - A Eur. J.* **2018**, *24* (52), 13728–13733. https://doi.org/10.1002/chem.201802929.
(104) Garabedian, A.; Butcher, D.; Lippens, J. L.; Miksovska, J.; Chapagain, P. P.; Fabris, D.; Ridgeway, M. E.; Park, M. A.; Fernandez-Lima, F. Structures of the Kinetically Trapped I-Motif DNA Intermediates. *Phys. Chem. Chem. Phys.* **2016**, *18* (38), 26691–26702. https://doi.org/10.1039/c6cp04418b.
(105) Daly, S.; Porrini, M.; Rosu, F.; Gabelica, V. Electronic Spectroscopy of Isolated DNA Polyanions. *Faraday Discuss.* **2019**, *217*, 361–382. https://doi.org/10.1039/C8FD00207J.
(106) Antoine, R.; Dugourd, P. Visible and Ultraviolet Spectroscopy of Gas Phase Protein Ions. *Phys. Chem. Chem. Phys.* **2011**, *13* (37), 16494–16509. https://doi.org/10.1039/c1cp21531k.
(107) Crittenden, C. M.; Escobar, E. E.; Williams, P. E.; Sanders, J. D.; Brodbelt, J. S. Characterization of Antigenic Oligosaccharides from Gram-Negative Bacteria via Activated Electron Photodetachment Mass Spectrometry. *Anal. Chem.* **2019**, *91* (7), 4672–4679. https://doi.org/10.1021/acs.analchem.9b00048.
(108) Antoine, R.; Lemoine, J.; Dugourd, P. Electron Photodetachment Dissociation for Structural Characterization of Synthetic and Bio‐polymer Anions. *Mass Spectrom. Rev.* **2014**, *33* (6), 501–522. https://doi.org/10.1002/mas.21402.
(109) Giuliani, A.; Milosavljević, A. R.; Canon, F.; Nahon, L. Contribution of Synchrotron Radiation to Photoactivation Studies of Biomolecular Ions in the Gas Phase. *Mass Spectrom. Rev.* **2014**, *33* (6), 424–441. https://doi.org/10.1002/mas.21398.
(110) Brunet, C.; Antoine, R.; Dugourd, P.; Canon, F.; Giuliani, A.; Nahon, L. Photo-Induced Electron Detachment of Protein Polyanions in the VUV Range. *J. Chem. Phys.* **2013**, *138* (6), 64301. https://doi.org/10.1063/1.4790165.
(111) Edirisinghe, P. D.; Moore, J. F.; Calaway, W. F.; Veryovkin, I. V.; Pellin, M. J.; Hanley, L. Vacuum Ultraviolet Postionization of Aromatic Groups Covalently Bound to Peptides. *Anal. Chem.* **2006**, *78* (16), 5876–5883. https://doi.org/10.1021/ac0605997.
(112) Ueda, K. High-Resolution Inner-Shell Spectroscopies of Free Atoms and Molecules Using Soft-x-Ray Beamlines at the Third-Generation Synchrotron Radiation Sources. *J. Phys. B At. Mol. Opt. Phys.* **2003**, *36* (4), R1–R47. https://doi.org/10.1088/0953-4075/36/4/201.
(113) Plekan, O.; Feyer, V.; Richter, R.; Coreno, M.; De Simone, M.; Prince, K. C.; Carravetta, V. Investigation of the Amino Acids Glycine, Proline, and Methionine by Photoemission Spectroscopy. *J. Phys. Chem. A* **2007**, *111* (43), 10998–11005. https://doi.org/10.1021/jp075384v.
(114) Farrokhpour, H.; Fathi, F.; De Brito, A. N. Theoretical and Experimental Study of Valence Photoelectron Spectrum of D,L-Alanine Amino Acid. *J. Phys. Chem. A* **2012**, *116* (26), 7004–7015. https://doi.org/10.1021/jp3023716.
(115) Wickrama Arachchilage, A. P.; Wang, F.; Feyer, V.; Plekan, O.; Prince, K. C. Photoelectron Spectra and Structures of Three Cyclic Dipeptides: PhePhe, TyrPro, and HisGly. *J. Chem. Phys.* **2012**, *136* (12), 124301. https://doi.org/10.1063/1.3693763.
(116) Plekan, O.; Feyer, V.; Richter, R.; Coreno, M.; de Simone, M.; Prince, K. C.; Trofimov, A. B.; Gromov, E. V.; Zaytseva, I. L.; Schirmer, J. A Theoretical and Experimental Study of the near Edge X-Ray Absorption Fine Structure (NEXAFS) and X-Ray Photoelectron

Spectra (XPS) of Nucleobases: Thymine and Adenine. *Chem. Phys.* **2008**, *347* (1–3), 360–375. https://doi.org/10.1016/j.chemphys.2007.09.021.

(117) Trofimov, A. B.; Schirmer, J.; Kobychev, V. B.; Potts, A. W.; Holland, D. M. P.; Karlsson, L. Photoelectron Spectra of the Nucleobases Cytosine, Thymine and Adenine. *J. Phys. B At. Mol. Opt. Phys.* **2006**, *39* (2), 305–329. https://doi.org/10.1088/0953-4075/39/2/007.

(118) Milosavljević, A. R.; Canon, F.; Nicolas, C.; Miron, C.; Nahon, L.; Giuliani, A. Gas-Phase Protein Inner-Shell Spectroscopy by Coupling an Ion Trap with a Soft X-Ray Beamline. *J. Phys. Chem. Lett.* **2012**, *3* (9), 1191–1196. https://doi.org/10.1021/jz300324z.

(119) Bari, S.; Egorov, D.; Jansen, T. L. C.; Boll, R.; Hoekstra, R.; Techert, S.; Zamudio-Bayer, V.; Bülow, C.; Lindblad, R.; Leistner, G.; Ławicki, A.; Hirsch, K.; Miedema, P. S.; von Issendorff, B.; Lau, J. T.; Schlathölter, T. Soft X-ray Spectroscopy as a Probe for Gas-Phase Protein Structure: Electron Impact Ionization from Within. *Chem. – A Eur. J.* **2018**, *24* (30), 7631–7636. https://doi.org/10.1002/chem.201801440.

(120) Schwob, L.; Dörner, S.; Atak, K.; Schubert, K.; Timm, M.; Bülow, C.; Zamudio-Bayer, V.; von Issendorff, B.; Lau, J. T.; Techert, S.; Bari, S. Site-Selective Dissociation upon Sulfur L-Edge X-Ray Absorption in a Gas-Phase Protonated Peptide. *J. Phys. Chem. Lett.* **2020**, *11* (4), 1215–1221. https://doi.org/10.1021/acs.jpclett.0c00041.

(121) Wang, X.; Rathnachalam, S.; Bijlsma, K.; Li, W.; Hoekstra, R.; Kubin, M.; Timm, M.; von Issendorff, B.; Zamudio-Bayer, V.; Lau, J. T.; Faraji, S.; Schlathölter, T. Site-Selective Soft X-Ray Absorption as a Tool to Study Protonation and Electronic Structure of Gas-Phase DNA. *Phys. Chem. Chem. Phys.* **2021**, *23* (20), 11900–11906. https://doi.org/10.1039/D1CP01014J.

(122) Frohlich, H.; Le Maire, M.; Guillot, F.; Tronc, M.; Cosset, J. M.; Le Sech, C. Fragmentation of Dinucleotides d(ApAp) Following K Shell Ionization of Phosphorus Atom by Monochromatic Soft X-Rays. *Nucl. Instruments Methods Phys. Res. Sect. B Beam Interact. with Mater. Atoms* **1995**, *105* (1–4), 314–317. https://doi.org/10.1016/0168-583X(95)00541-2.

(123) 2 K. HIEDA , T. HIRONO , A. AZAMI , 1. Single- and Double-Strand Breaks in PBR322 Plasmid DNA by Monochromatic X-Rays on and off the K-Absorption Peak of Phosphorus. *Int. J. Radiat. Biol.* **1996**, *70* (4), 437–445. https://doi.org/10.1080/095530096144914.

(124) Saigusa, S.; Ejima, Y.; Kobayashi, K.; Sasaki, M. S. Induction of Chromosome Aberrations by Monochromatic X-Rays with Resonance Energy of Phosphorus K-Shell Absorption Edge. *Int. J. Radiat. Biol.* **1992**, *61* (6), 785–790. https://doi.org/10.1080/09553009214551651.

(125) Poully, J.-C.; Miles, J.; De Camillis, S.; Cassimi, A.; Greenwood, J. B. Proton Irradiation of DNA Nucleosides in the Gas Phase. *Phys. Chem. Chem. Phys.* **2015**, *17* (11), 7172–7180. https://doi.org/10.1039/C4CP05303F.

(126) Henke, B. L.; Gullikson, E. M.; Davis, J. C. X-Ray Interactions: Photoabsorption, Scattering, Transmission, and Reflection at E = 50-30, 000 EV, Z = 1-92. *Atomic Data and Nuclear Data Tables*. 1993, pp 181–342. https://doi.org/10.1006/adnd.1993.1013.

(127) Bari, S.; Gonzalez-Magaña, O.; Reitsma, G.; Werner, J.; Schippers, S.; Hoekstra, R.; Schlathölter, T. Photodissociation of Protonated Leucine-Enkephalin in the VUV Range of 8–40 EV. *J. Chem. Phys.* **2011**, *134* (2), 024314. https://doi.org/10.1063/1.3515301.

(128) Egorov, D.; Schwob, L.; Lalande, M.; Hoekstra, R.; Schlathölter, T. Near Edge X-Ray Absorption Mass Spectrometry of Gas Phase Proteins: The Influence of Protein Size. *Phys. Chem. Chem. Phys.* **2016**, *18* (37), 26213–26223. https://doi.org/10.1039/C6CP05254A.

(129) Buck, J.; Bagschik, K.; Glaser, L.; Scholz, F.; Seltmann, J.; Viefhaus, J. Progress Report on the XUV Online Diagnostic Unit for the Highly Accurate Determination of SR Properties. *AIP Conf. Proc.* **2019**, *2054* (January 2019), 060057. https://doi.org/10.1063/1.5084688.

(130) LaVilla, R. E. The Sulfur K and L and Fluorine K X-Ray Emission and Absorption Spectra of Gaseous SF 6. *J. Chem. Phys.* **1972**, *57* (2), 899–909. https://doi.org/10.1063/1.1678337.

(131) Kato, M.; Morishita, Y.; Oura, M.; Yamaoka, H.; Tamenori, Y.; Okada, K.; Matsudo, T.; Gejo, T.; Suzuki, I. H. H.; Saito, N. Absolute Photoionization Cross Sections with Ultra-High Energy Resolution for Ar, Kr, Xe and N2 in Inner-Shell Ionization Regions. *J. Electron Spectros. Relat. Phenomena* **2007**, *160* (1–3), 39–48. https://doi.org/10.1016/j.elspec.2007.06.003.

(132) Franke, R.; Hormes, J. The P K-near Edge Absorption Spectra of Phosphates. *Phys. B Phys. Condens. Matter* **1995**, *216* (1–2), 85–95. https://doi.org/10.1016/0921-4526(95)00446-7.

(133) Czapla-Masztafiak, J.; Szlachetko, J.; Milne, C. J.; Lipiec, E.; Sá, J.; Penfold, T. J.; Huthwelker, T.; Borca, C.; Abela, R.; Kwiatek, W. M. Investigating DNA Radiation Damage Using X-Ray Absorption Spectroscopy. *Biophys. J.* **2016**, *110* (6), 1304–1311. https://doi.org/10.1016/j.bpj.2016.01.031.

(134) Little, D. P.; Aaserud, D. J.; Valaskovic, G. A.; McLafferty, F. W. Sequence Information from 42-108-Mer DNAs (Complete for a 50-Mer) by Tandem Mass Spectrometry. *J. Am. Chem. Soc.* **1996**, *118* (39), 9352–9359. https://doi.org/10.1021/ja9533611.

(135) Egorov, D.; Hoekstra, R.; Schlathölter, T. A Comparative VUV Absorption Mass-Spectroscopy Study on Protonated Peptides of Different Size. *Phys. Chem. Chem. Phys.* **2017**, *19* (31), 20608–20618. https://doi.org/10.1039/c7cp03203j.

(136) Lalande, M.; Abdelmouleh, M.; Ryszka, M.; Vizcaino, V.; Rangama, J.; Méry, A.; Durantel, F.; Schlathölter, T.; Poully, J.-C. Irradiation of Isolated Collagen Mimetic Peptides by x Rays and Carbon Ions at the Bragg-Peak Energy. *Phys. Rev. A* **2018**, *98* (6), 062701. https://doi.org/10.1103/PhysRevA.98.062701.

(137) Ni, J.; Mathews, M. A. A.; McCloskey, J. A. Collision-Induced Dissociation of Polyprotonated Oligonucleotides Produced by Electrospray Ionization. *Rapid Commun. Mass Spectrom.* **1997**, *11* (6), 535–540. https://doi.org/10.1002/(SICI)1097-0231(199704)11:6<535::AID-RCM898>3.0.CO;2-P.

(138) Favre, A.; Gonnet, F.; Tabet, J. C. Location of the Negative Charge(s) on the Backbone of Single-Stranded Deoxyribonucleic Acid in the Gas Phase. *Eur. J. Mass Spectrom.* **2000**, *6* (5), 389–396. https://doi.org/10.1255/ejms.360.

(139) Tsujii, H.; Kamada, T.; Shirai, T.; Noda, K.; Tsuji, H.; Karasawa, K. *Carbon-Ion Radiotherapy*; Tsujii, H., Kamada, T., Shirai, T., Noda, K., Tsuji, H., Karasawa, K., Eds.; Springer Japan: Tokyo, 2014. https://doi.org/10.1007/978-4-431-54457-9.

(140) Tsujii, H.; Kamada, T. A Review of Update Clinical Results of Carbon Ion Radiotherapy. *Jpn. J. Clin. Oncol.* **2012**, *42* (8), 670–685. https://doi.org/10.1093/jjco/hys104.

(141) Agnihotri, A. N.; Kasthurirangan, S.; Nandi, S.; Kumar, A.; Galassi, M. E.; Rivarola, R. D.; Fojón, O.; Champion, C.; Hanssen, J.; Lekadir, H.; Weck, P. F.; Tribedi, L. C. Ionization of Uracil in Collisions with Highly Charged Carbon and Oxygen Ions of Energy 100 KeV to 78 MeV. *Phys. Rev. A - At. Mol. Opt. Phys.* **2012**, *85* (3), 1–5. https://doi.org/10.1103/PhysRevA.85.032711.

(142) Agnihotri, A. N.; Kasthurirangan, S.; Nandi, S.; Kumar, A.; Champion, C.; Lekadir, H.; Hanssen, J.; Weck, P. F.; Galassi, M. E.; Rivarola, R. D.; Fojón, O.; Tribedi, L. C. Absolute Total Ionization Cross Sections of Uracil (C 4 H 4 N 2 O 2) in Collisions with MeV Energy Highly Charged Carbon, Oxygen and Fluorine Ions. *J. Phys. B At. Mol.*

Opt. Phys. **2013**, *46* (18), 185201. https://doi.org/10.1088/0953-4075/46/18/185201.
(143) Krisch, R. E.; Flick, M. B.; Trumbore, C. N. Radiation Chemical Mechanisms of Single- and Double-Strand Break Formation in Irradiated SV40 DNA. *Radiat. Res.* **1991**, *126* (2), 251–259. https://doi.org/10.2307/3577826.
(144) Urushibara, A.; Shikazono, N.; O'Neill, P.; Fujii, K.; Wada, S.; Yokoya, A. LET Dependence of the Yield of Single-, Double-Strand Breaks and Base Lesions in Fully Hydrated Plasmid DNA Films by 4 He 2+ Ion Irradiation. *Int. J. Radiat. Biol.* **2008**, *84* (1), 23–33. https://doi.org/10.1080/09553000701616072.
(145) Dang, H. M.; Van Goethem, M. J.; Van Der Graaf, E. R.; Brandenburg, S.; Hoekstra, R.; Schlathölter, T. Plasmid DNA Damage by Heavy Ions at Spread-out Bragg Peak Energies. *Eur. Phys. J. D* **2010**, *60* (1), 51–58. https://doi.org/10.1140/epjd/e2010-00080-1.
(146) Yokoya, A.; Cunniffe, S. M. T.; Stevens, D. L.; O'Neill, P. Effects of Hydration on the Induction of Strand Breaks, Base Lesions, and Clustered Damage in DNA Films by α-Radiation. *J. Phys. Chem. B* **2003**, *107* (3), 832–837. https://doi.org/10.1021/jp0270708.
(147) Ptasińska, S.; Stypczyńska, A.; Nixon, T.; Mason, N. J.; Klyachko, D. V.; Sanche, L. X-Ray Induced Damage in DNA Monitored by X-Ray Photoelectron Spectroscopy. *J. Chem. Phys.* **2008**, *129* (6), 065102. https://doi.org/10.1063/1.2961027.
(148) Sukhodub, L. F. Interactions and Hydration of Nucleic Acid Bases in a Vacuum. Experimental Study. *Chem. Rev.* **1987**, *87* (3), 589–606. https://doi.org/10.1021/cr00079a006.
(149) Schermann, J.-P. *Spectroscopy and Modeling of Biomolecular Building Blocks*; Elsevier: Amsterdam, 2007.
(150) Ahmed, M.; Kostko, O. From Atoms to Aerosols: Probing Clusters and Nanoparticles with Synchrotron Based Mass Spectrometry and X-Ray Spectroscopy. *Phys. Chem. Chem. Phys.* **2020**, *22* (5), 2713–2737. https://doi.org/10.1039/C9CP05802H.
(151) Baer, T.; Tuckett, R. P. Advances in Threshold Photoelectron Spectroscopy (TPES) and Threshold Photoelectron Photoion Coincidence (TPEPICO). *Phys. Chem. Chem. Phys.* **2017**, *19* (15), 9698–9723. https://doi.org/10.1039/C7CP00144D.
(152) Becker, U.; Shirley, D. A. *VUV and Soft X-Ray Photoionization*; Springer New York: New York, 1996.
(153) Berden, G.; Peeters, R.; Meijer, G. Cavity Ring-down Spectroscopy: Experimental Schemes and Applications. *Int. Rev. Phys. Chem.* **2000**, *19* (4), 565–607. https://doi.org/10.1080/014423500750040627.
(154) Schwell, M.; Hochlaf, M. Photoionization Spectroscopy of Nucleobases and Analogues in the Gas Phase Using Synchrotron Radiation as Excitation Light Source; Mario, B., Carlos, B. A., Ullrich, S., Eds.; Springer Cham: Switzerland, 2014; pp 155–208. https://doi.org/10.1007/128_2014_550.
(155) Prince, K. C.; Bolognesi, P.; Feyer, V.; Plekan, O.; Avaldi, L. Study of Complex Molecules of Biological Interest with Synchrotron Radiation. *J. Electron Spectros. Relat. Phenomena* **2015**, *204*, 335–344. https://doi.org/10.1016/j.elspec.2015.08.010.
(156) Meinert, C.; Garcia, A. D.; Topin, J.; Jones, N. C.; Diekmann, M.; Berger, R.; Nahon, L.; Hoffmann, S. V.; Meierhenrich, U. J. Amino Acid Gas Phase Circular Dichroism and Implications for the Origin of Biomolecular Asymmetry. *Nat. Commun.* **2022**, *13* (1), 502. https://doi.org/10.1038/s41467-022-28184-0.
(157) Tia, M.; Cunha de Miranda, B.; Daly, S.; Gaie-Levrel, F.; Garcia, G. A.; Powis, I.; Nahon, L. Chiral Asymmetry in the Photoionization of Gas-Phase Amino-Acid Alanine at Lyman-α Radiation Wavelength. *J. Phys. Chem. Lett.* **2013**, *4* (16), 2698–2704. https://doi.org/10.1021/jz4014129.
(158) Hadidi, R.; Božanić, D. K.; Ganjitabar, H.; Garcia, G. A.; Powis, I.; Nahon, L.

Conformer-Dependent Vacuum Ultraviolet Photodynamics and Chiral Asymmetries in Pure Enantiomers of Gas Phase Proline. *Commun. Chem.* **2021**, *4* (1), 72. https://doi.org/10.1038/s42004-021-00508-z.

(159) Gaie-Levrel, F.; Garcia, G. A.; Schwell, M.; Nahon, L. VUV State-Selected Photoionization of Thermally-Desorbed Biomolecules by Coupling an Aerosol Source to an Imaging Photoelectron/Photoion Coincidence Spectrometer: Case of the Amino Acids Tryptophan and Phenylalanine. *Phys. Chem. Chem. Phys.* **2011**, *13* (15), 7024. https://doi.org/10.1039/c0cp02798g.

(160) Wilson, K. R.; Jimenez-Cruz, M.; Nicolas, C.; Belau, L.; Leone, S. R.; Ahmed, M. Thermal Vaporization of Biological Nanoparticles: Fragment-Free Vacuum Ultraviolet Photoionization Mass Spectra of Tryptophan, Phenylalanine−Glycine−Glycine, and β-Carotene. *J. Phys. Chem. A* **2006**, *110* (6), 2106–2113. https://doi.org/10.1021/jp0543734.

(161) Giuliani, A.; Milosavljević, A. R.; Hinsen, K.; Canon, F.; Nicolas, C.; Réfrégiers, M.; Nahon, L. Structure and Charge-State Dependence of the Gas-Phase Ionization Energy of Proteins. *Angew. Chemie Int. Ed.* **2012**, *51* (38), 9552–9556. https://doi.org/10.1002/anie.201204435.

(162) Hendricks, N. G.; Julian, R. R. Leveraging Ultraviolet Photodissociation and Spectroscopy to Investigate Peptide and Protein Three-Dimensional Structure with Mass Spectrometry. *Analyst* **2016**, *141* (15), 4534–4540. https://doi.org/10.1039/C6AN01020B.

(163) González-Magaña, O.; Reitsma, G.; Tiemens, M.; Boschman, L.; Hoekstra, R.; Schlathölter, T. Near-Edge X-Ray Absorption Mass Spectrometry of a Gas-Phase Peptide. *J. Phys. Chem. A* **2012**, *116* (44), 10745–10751. https://doi.org/10.1021/jp307527b.

(164) Canon, F.; Milosavljević, A. R.; Nahon, L.; Giuliani, A. Action Spectroscopy of a Protonated Peptide in the Ultraviolet Range. *Phys. Chem. Chem. Phys.* **2015**, *17* (39), 25725–25733. https://doi.org/10.1039/C4CP04762A.

(165) Boyarkin, O. V. Cold Ion Spectroscopy for Structural Identifications of Biomolecules. *Int. Rev. Phys. Chem.* **2018**, *37* (3–4), 559–606. https://doi.org/10.1080/0144235X.2018.1547453.

(166) Paizs, B.; Suhai, S. Fragmentation Pathways of Protonated Peptides. *Mass Spectrom. Rev.* **2005**, *24* (4), 508–548. https://doi.org/10.1002/mas.20024.

(167) Milosavljević, A. R.; Nicolas, C.; Ranković, M. L.; Canon, F.; Miron, C.; Giuliani, A. K-Shell Excitation and Ionization of a Gas-Phase Protein: Interplay between Electronic Structure and Protein Folding. *J. Phys. Chem. Lett.* **2015**, *6* (16), 3132–3138. https://doi.org/10.1021/acs.jpclett.5b01288.

(168) McKay, A. R.; Sanz, M. E.; Mooney, C. R. S.; Minns, R. S.; Gill, E. M.; Fielding, H. H. Development of a New Photoelectron Spectroscopy Instrument Combining an Electrospray Ion Source and Photoelectron Imaging. *Rev. Sci. Instrum.* **2010**, *81* (12). https://doi.org/10.1063/1.3505097.

(169) Nieto, M.; Perkins, H. R. Modifications of the Acyl-D-Alanyl-D-Alanine Terminus Affecting Complex-Formation with Vancomycin. *Biochem. J.* **1971**, *123* (5), 789–803. https://doi.org/10.1042/bj1230789.

(170) Nitanai, Y.; Kikuchi, T.; Kakoi, K.; Hanamaki, S.; Fujisawa, I.; Aoki, K. Crystal Structures of the Complexes between Vancomycin and Cell-Wall Precursor Analogs. *J. Mol. Biol.* **2009**, *385* (5), 1422–1432. https://doi.org/10.1016/j.jmb.2008.10.026.

(171) Poully, J. C.; Lecomte, F.; Nieuwjaer, N.; Manil, B.; Schermann, J. P.; Desfrançois, C.; Calvo, F.; Grégoire, G. Probing the Specific Interactions and Structures of Gas-Phase Vancomycin Antibiotics with Cell-Wall Precursor through IRMPD Spectroscopy. *Phys.*

Chem. Chem. Phys. **2010**, *12* (14), 3606. https://doi.org/10.1039/b923787a.

(172) Poully, J. C.; Lecomte, F.; Nieuwjaer, N.; Manil, B.; Schermann, J. P.; Desfrançois, C.; Grégoire, G.; Ballivian, R.; Chirot, F.; Lemoine, J.; Calvo, F.; Antoine, R.; Dugourd, P. Combining Ion Mobility Mass Spectrometry and Infrared Multiphoton Dissociation Spectroscopy to Probe the Structure of Gas-Phase Vancomycin-Ac2LKDADA Non-Covalent Complex. *Int. J. Mass Spectrom.* **2010**, *297* (1–3), 28–35. https://doi.org/10.1016/j.ijms.2010.05.014.

(173) Jørgensen, T. J. D.; Delforge, D.; Remacle, J.; Bojesen, G.; Roepstorff, P. Collision-Induced Dissociation of Noncovalent Complexes between Vancomycin Antibiotics and Peptide Ligand Stereoisomers: Evidence for Molecular Recognition in the Gas Phase. *Int. J. Mass Spectrom.* **1999**, *188* (1–2), 63–85. https://doi.org/10.1016/S1387-3806(98)14282-3.

(174) Abdelmouleh, M.; Lalande, M.; Vizcaino, V.; Schlathölter, T.; Poully, J. Photoinduced Processes within Noncovalent Complexes Involved in Molecular Recognition. *Chem. – A Eur. J.* **2020**, *26* (10), 2243–2250. https://doi.org/10.1002/chem.201904786.

(175) Nahon, L.; de Oliveira, N.; Garcia, G. A.; Gil, J.-F.; Pilette, B.; Marcouillé, O.; Lagarde, B.; Polack, F. DESIRS: A State-of-the-Art VUV Beamline Featuring High Resolution and Variable Polarization for Spectroscopy and Dichroism at SOLEIL. *J. Synchrotron Radiat.* **2012**, *19* (4), 508–520. https://doi.org/10.1107/S0909049512010588.

(176) Milosavljević, A. R.; Nicolas, C.; Gil, J.-F.; Canon, F.; Réfrégiers, M.; Nahon, L.; Giuliani, A. VUV Synchrotron Radiation: A New Activation Technique for Tandem Mass Spectrometry. *J. Synchrotron Radiat.* **2012**, *19* (2), 174–178. https://doi.org/10.1107/S0909049512001057.

(177) Brunet, C.; Antoine, R.; Allouche, A.-R.; Dugourd, P.; Canon, F.; Giuliani, A.; Nahon, L. Gas Phase Photo-Formation and Vacuum UV Photofragmentation Spectroscopy of Tryptophan and Tyrosine Radical-Containing Peptides. *J. Phys. Chem. A* **2011**, *115* (32), 8933–8939. https://doi.org/10.1021/jp205617x.

(178) Bowie, J. H.; Brinkworth, C. S.; Dua, S. Collision-induced Fragmentations of the (M-H)− Parent Anions of Underivatized Peptides: An Aid to Structure Determination and Some Unusual Negative Ion Cleavages. *Mass Spectrom. Rev.* **2002**, *21* (2), 87–107. https://doi.org/10.1002/mas.10022.

(179) Yang, Z.; Vorpagel, E. R.; Laskin, J. Influence of the Charge State on the Structures and Interactions of Vancomycin Antibiotics with Cell - wall Analogue Peptides: Experimental and Theoretical Studies. *Chem. Eur. J.* **2009**, *15* (9), 2081–2090. https://doi.org/10.1002/chem.200802010.

(180) Serrano-Andrés, L.; Fülscher, M. P. Charge Transfer Transitions in Neutral and Ionic Polypeptides: A Theoretical Study. *J. Phys. Chem. B* **2001**, *105* (38), 9323–9330. https://doi.org/10.1021/jp0034473.

(181) Jones, D. B.; da Silva, G. B.; Neves, R. F. C.; Duque, H. V; Chiari, L.; de Oliveira, E. M.; Lopes, M. C. A.; da Costa, R. F.; Varella, M. T. do N.; Bettega, M. H. F.; Lima, M. A. P.; Brunger, M. J. An Experimental and Theoretical Investigation into the Excited Electronic States of Phenol. *J. Chem. Phys.* **2014**, *141* (7), 74314. https://doi.org/10.1063/1.4893116.

(182) Matheis, K.; Joly, L.; Antoine, R.; Lépine, F.; Bordas, C.; Ehrler, O. T.; Allouche, A.-R.; Kappes, M. M.; Dugourd, P. Photoelectron Spectroscopy of Gramicidin Polyanions: Competition between Delayed and Direct Emission. *J. Am. Chem. Soc.* **2008**, *130* (47), 15903–15906. https://doi.org/10.1021/ja803758w.

(183) Besley, N. A.; Hirst, J. D. Ab Initio Study of the Effect of Solvation on the Electronic Spectra of Formamide and N-Methylacetamide. *J. Phys. Chem. A* **1998**, *102* (52), 10791–10797. https://doi.org/10.1021/jp982645f.

(184) LeGreve, T. A.; James III, W. H.; Zwier, T. S. Solvent Effects on the Conformational Preferences of Serotonin: Serotonin−(H2O)n, n = 1,2. *J. Phys. Chem. A* **2009**, *113* (2), 399–410. https://doi.org/10.1021/jp807031y.

Acknowledgments

I would like to thank all the people who have helped me during my PhD studies.

First of all, I will always be grateful to my supervisor Jean-Christophe POULLY for all his help and support. Thank you for accepting a Masters student in Chemical Biology to do a PhD in Physics. It opens up a new scientific world for me. I know this is not an easy job for you. You have patiently explained many basic concepts in physics to me. I have learnt a lot from you, both scientifically and spiritually.

Furthermore, I would also like to thank Jean-Yves CHESNEL for supporting my academic missions as the AMA group leader. What's more, you are always ready to help like a friend when I have any problems.

I wish to acknowledge my fellow (formal) colleagues of the Atomes, Molécules et Agrégats (AMA) group for their help: Thank you Alain MERY, Alicja DOMARACKA, Alma KURMANOVA, Amine CASSIMI, David O'REILLY, Jimmy RANGAMA, Juliette LEROUX, Marwa ABDELMOULEH, Patrick ROUSSEAU, Penelope CHRISTODOULOU, and Violaine VIZCAINO. You are always there when I need some help. Many of you have helped me with my experiments at IRRSUD, GANIL. Special thanks for that.

I wish to thank Siamak HAGHDOOST and Thomas ROGER for being my CSI members and supporting me.

I would like to thank the members of my reading committee for carefully reading the manuscript and providing me with useful comments and corrections.

I wish to express my gratitude to all the people at the CIMAP lab. Especially to Tristan LE CORNU for bringing me into the big lab family and always being a good friend wherever you are. To Massimo LEGER and Mukul DHIMAN for being my office mates and answering all my stupid questions. To Anna BYCHKOVA, Cintiaaparecida PIRESDACOSTA and Lisa BASYROVA for being good friends and providing me lots of laughs. To Amandine BAILLARD, Erwan HOCHARD, Kou IHARA, Krill КИРИЛЛ, Michel DU CHALARD, Radia RAHALI, Hoda AL ASSAAD *etc.* for presenting all kinds of parties with me. To Eric GIGLIO and Julie DOUADY for hosting very nice parties. To François CHEVALIER for all the support in ARIA lab. To Florian AUBRIT for helping me with my scientific figures and the UV-vis absorption spectroscopy experiments in the solution phase.

I want to thank Lucas DE ARRUDA at GANIL for your kindness and your help. Also Lucas BEGUE GUILLOU for having some good time together.

In the course of my PhD I had the possibility to collaborate with several international research groups.

- HUO Yining, Jente DAMM, LI Wen, Marcelo GOULART, WANG Xin, Thomas Schalthölter from University of Groningen, Netherlands. I have had three beamtimes with your group and they are really important for my PhD. I have learnt so much from you.
- Alexandre GIULIANI, Laurent NAHON from SOLEIL, France. Thank you for your patient instrcution during my beamtime at SOLEIL.
- Lucas SCHWOB, Sadia BARI from Deutsches Elektronen-Synchrotron DESY. Thank you for helping me during my beamtime at DESY.
- Benoit BERNAY from PROTEOGEN Platform at the University of Caen Normandy. Thank you for helping me with the experiments using the ion mobility mass spectrometer.

I would like to thank all my friends who always give me help when needed. It’s nice to have friends like CHEN Jianqi, DAI Weijiong, LI Siqian, ZHANG Chuanqi, ZHAO Weitao in Caen. Many thanks to MAO Wenjing, QI Wenbo, TIAN Haoran, XU Wansha, ZOU Jinghan for having the good time in Caen. Glad to meet FENG Zexi, LI Zhigang, XU Ouming in Cité U Lebisey. Thanks to YOU Min and Jean-Paul CHENAL for my diving lessons. Thank you Lucile MORIN for being my flatmate. A special thank you to XIAO Pan for picking me up at the CDG airport on my arrival in France.

At the end, I would like to thank my family, who have always given me their support and love.

List of publications

1. Liu, M.; Abdelmouleh, M.; Giuliani, A.; Nahon, L.; Poully, J.-C. UV–VUV Photofragmentation Spectroscopy of Isolated Neutral Fragile Macromolecules: A Proof-of-Principle Based on a Deprotonated Vancomycin–Peptide Noncovalent Complex. *J. Phys. Chem. A* **2022**, *126* (48), 9042–9050. https://doi.org/10.1021/acs.jpca.2c07744. (The appendix is reprinted from it.)

2. Liu, M.; O'Reilly, D.; Schwob, L.; Wang, X.; Zamudio-Bayer, V.; Lau, J. T.; Bari, S.; Schlathölter, T.; Poully, J. Direct Observation of Charge, Energy, and Hydrogen Transfer between the Backbone and Nucleobases in Isolated DNA Oligonucleotides. *Chem. – A Eur. J.* **2023**, *29* (13), e202203481. https://doi.org/10.1002/chem.202203481. (Chapter 4 is adapted from it.)

Abstract / Résumé

Title: Radiation-induced processes within DNA in the gas phase

DNA damage is generally considered to be the most common and most important type of lesions in cells caused by ionizing radiation. While DNA damage caused by ionizing radiation poses serious risks to human health, it also makes radiation therapy a powerful tool for killing cancer cells and saving lives. For these reasons, a great deal of research has focused on radiation-induced processes within DNA. However, most of this work has been carried out in the condensed phase, which cannot remove the influence of the surrounding environment. In order to investigate the consequences of direct interaction of DNA with ionizing radiation at the molecular scale, we have irradiated a self-complementary DNA sequence in the gas phase with synchrotron radiation or ion beams, and analyzed the resulting product ions by mass spectrometry. Thanks to ion mobility spectrometry, we have established that deprotonated double strands of this sequence indeed form a double helix that is stable in an ion trap, if the charge state is higher than 5-. Then, we have investigated the consequences of specific photoabsorption occurring at the DNA oligonucleotide backbone in the gas phase. By monitoring non-dissociative single electron detachment from deprotonated precursors as a function of photon energy around the phosphorus K-edge, we have identified the X-ray spectral signature of selective photoabsorption at the phosphorus atoms located only in the backbone. We also detected abundant nucleobase fragment cations resulting from multiple electron detachment and thus demonstrated the charge, energy and hydrogen transfer from the backbone to the nucleobases. In the final part of the thesis, we present the results of irradiation of the DNA oligonucleotides by carbon ions in the gas phase. We have observed similar non-dissociative single electron detachment and similarly abundant positive fragment ions after carbon ion impact as in the case of irradiation by X-ray photons. More importantly, we have successfully irradiated a helical DNA double strand in the gas phase for the first time. 70% of the resulting ionic products come from non-dissociative single electron detachment, which is much higher than the case of single strands. Therefore, direct ionization of a DNA double helix after interaction with a single carbon ion does not lead to separation of the strands, which has important implications regarding DNA damage, notably in the context of hadrontherapy.

Key Words : Mass spectrometry, Gas phase, X-ray photons, carbon ions, DNA, Radiation.

Titre : Processus induits par les rayonnements ionisants au sein de l'ADN en phase gazeuse

Les dommages à l'ADN sont généralement considérés comme les lésions cellulaires les plus courantes et le plus importantes parmi celles causées par les rayonnements ionisants. Ces dommages présentent de graves risques pour la santé humaine, mais ils font également de la radiothérapie un outil puissant pour tuer les cellules cancéreuses et sauver des vies. Pour ces raisons, de nombreuses recherches se sont concentrées sur les processus induits par les radiations au sein de l'ADN. Cependant, la plupart de ces travaux ont été réalisés en phase condensée, ce qui ne permet pas d'éliminer l'influence du milieu environnant. Afin d'étudier les conséquences de l'interaction directe de l'ADN avec les rayonnements ionisants à l'échelle moléculaire, nous avons irradié une séquence d'ADN auto-complémentaire en phase gazeuse avec un rayonnement synchrotron ou des faisceaux d'ions, et analysé par spectrométrie de masse les ions moléculaires produits. Grâce à la spectrométrie de mobilité ionique, nous avons établi que les doubles brins déprotonés de cette séquence forment bien une double hélice stable dans un piège à ions, si l'état de charge est supérieur à 5-. Ensuite, nous avons étudié les conséquences de la photoabsorption spécifique se produisant au niveau du squelette oligonucléotidique de l'ADN en phase gazeuse. En surveillant le détachement non dissociatif d'un seul électron des précurseurs déprotonés en fonction de l'énergie des photons autour du bord K du phosphore, nous avons identifié la signature spectrale des rayons X de la photoabsorption sélective au niveau des atomes de phosphore situés uniquement dans le squelette. Nous avons également détecté d'abondants cations de fragments de bases nucléiques résultant du détachement de plusieurs électrons et avons ainsi démontré le transfert de charge, d'énergie et d'hydrogène du squelette vers les bases nucléiques. Dans la dernière partie de la thèse, nous présentons les résultats de l'irradiation des oligonucléotides d'ADN par des ions carbone en phase gazeuse. Nous avons observé un détachement non dissociatif d'un seul électron et des ions fragments positifs tout aussi abondants après l'impact d'ions carbone, comme dans le cas de l'irradiation par des photons de rayons X. Plus important encore, nous avons réussi pour la première fois à irradier un double brin d'ADN hélicoïdal en phase gazeuse. 70% des produits ioniques résultants proviennent d'un détachement non dissociatif d'un seul électron, ce qui est beaucoup plus élevé que dans le cas des simples brins. Par conséquent, l'ionisation directe d'une double hélice d'ADN après interaction avec un seul ion carbone n'entraîne pas de séparation des brins, ce qui a des implications importantes concernant les dommages à l'ADN, notamment dans le contexte de l'hadronthérapie.

Mots-clés : Spectrométrie de masse, Phase gazeuse, Photons X, ions carbone, ADN, Rayonnement.